University of Alberta

Microfluidic protein fractionator

By

©

Zhen Wang

A thesis submitted to the Faculty of Graduate Studies in partial fulfillment of the requirements for the degree of Doctor of Philosophy

Department of Chemistry
Edmonton, Alberta

Spring 2007

Library and
Archives Canada

Published Heritage
Branch

395 Wellington Street
Ottawa ON K1A 0N4
Canada

Bibliothèque et
Archives Canada

Direction du
Patrimoine de l'édition

395, rue Wellington
Ottawa ON K1A 0N4
Canada

NOTICE:
The author has granted a non-exclusive license allowing Library and Archives Canada to reproduce, publish, archive, preserve, conserve, communicate to the public by telecommunication or on the Internet, loan, distribute and sell theses worldwide, for commercial or non-commercial purposes, in microform, paper, electronic and/or any other formats.

The author retains copyright ownership and moral rights in this thesis. Neither the thesis nor substantial extracts from it may be printed or otherwise reproduced without the author's permission.

AVIS:
L'auteur a accordé une licence non exclusive permettant à la Bibliothèque et Archives Canada de reproduire, publier, archiver, sauvegarder, conserver, transmettre au public par télécommunication ou par l'Internet, prêter, distribuer et vendre des thèses partout dans le monde, à des fins commerciales ou autres, sur support microforme, papier, électronique et/ou autres formats.

L'auteur conserve la propriété du droit d'auteur et des droits moraux qui protège cette thèse. Ni la thèse ni des extraits substantiels de celle-ci ne doivent être imprimés ou autrement reproduits sans son autorisation.

In compliance with the Canadian Privacy Act some supporting forms may have been removed from this thesis.

While these forms may be included in the document page count, their removal does not represent any loss of content from the thesis.

Conformément à la loi canadienne sur la protection de la vie privée, quelques formulaires secondaires ont été enlevés de cette thèse.

Bien que ces formulaires aient inclus dans la pagination, il n'y aura aucun contenu manquant.

Canada

Abstract

In this thesis work, several generations of microfluidic protein fractionators were designed based on electrokinetically driven flow. The fractionator design was improved until a nicely focused sample stream was able to be produced at lower voltages. Two modes of fraction collection, peak selection and fixed time intervals, were explored. The fractionator and collector based on peak selection mode allows a relatively simple design, with the number of collection channels reduced to the number of components of interest. The "in-space" 36-channel fractionator and collector operated at fixed time intervals increases the fractionator's throughput and further increase of the number of fractionation channels is feasible on the basis of our results. The sample stream can be delivered to the grounded channel with no contamination of the other channels. The advantage of electrokinetically driven flow over hydrodynamic flow was embodied in the ability of electrokinetically driven flow to direct flow equally into individual channels on our device with multiple outlets. Polymer beds were coupled with the multiplexed fractionator in order to adsorb protein for further analysis. The sheath flow effect and protein adsorption on this fractionator with polymer beds were performed well. This fractionator will be coupled to protein separation stages in the future.

Thank all the nice people I met during the last four and half years, life in Edmonton will always become a happy memory for me. First and foremost, I would like to express my deep and sincere gratitude to my supervisor, Prof. D.J. Harrison. His patience, understanding and sense of humor made my life and study overseas easier. When I was frustrated, he would always be there with insightful guidance. I really appreciate that.

I cherish the wonderful time spent with former and present DJH group members. Thank Arlene Figley for taking care of many minute and time-consuming businesses and helping me with thesis revision. Thank Dr. J. Bao for instructive discussions and technical assistance. Thank Dr. A. Jemere for his generous help and revision of the thesis draft. Thank Dr. S. Sapelnikova, Dolores Martinez, Eric Flaim, Yong Zeng, Josh Wasylycia, Mei He, Qingye Lu and Yujuan Hua for their company in the lab and funny jokes.

I would also like to show my gratitude to my committee members, Dr. Liang Li, Dr. Mariusz Klobukowski, Dr. X. Chris Le, Dr. Subir Bhattacharjee, and Dr. Robert Corn, for their support in my candidacy exam and final oral exam.

I am grateful for the help from the staff in machine shop, electronic shop, general office and nanofab. Without their assistance, the thesis would never have been finished smoothly.

Finally, I'd like to give my sincere thanks to my family. Thank my parents for their encouragement these years. Now, they are helping me take care of my little daughter in order to give me more free time. My husband is always like an intimate friend and big brother to me. He tolerates my temper and shares my happiness and bitterness all the time. I also want to thank my adorable daughter. Every time I heard her laughing and saw her cute face, I knew what I was working for.

Table of Contents

List of Tables

List of Figures

List of Abbreviations

ACN	acetonitrile
AMPS	2-Acrylamido-2-methyl-1-propanesulfonic acid
BMA	Butyl methacrylate
CGE	Capillary gel electrophoresis
cIEF	Capillary isoelectric focusing
CZE	Capillary zone electrophoresis
DMAP	4-(Dimethylamino)-benzophenone
DPA	2,2 Dimethoxy-2-phenyl-acetophenone
EDMA	Ethylene glycol dimethacrylate
FFF	Field flow fractionation
FITC	fluorescein isothiocyanate conjugate
EOF	Electroosmotic flow
GMA	Glycidyl methacrylate
IgG	immunoglobulin G
ITP	Isotachophoresis
SPE	Solid phase extraction
MEKC	Micellar electrokinetic chromatography
MS	Mass Spectrometry
PAGE	Polyacrylamide gel electrophoresis
SEM	Scan electron microscopy

1.1 Introduction

Micro total analysis systems (μTAS) have drawn extensive attention since the concept was introduced 16 years ago. Nowadays, μTAS devices are being developed for fields including protein analysis [1-5], DNA analysis [6-8], cell culture [9,10], and biomarker screening [11,12]. The drastic expansion in the application of micro total analysis systems, or so-called "Lab on chip" technology, may be attributed to the potential advantages over other analysis systems. Briefly, analysis on a microchip can reach high separation efficiency in a very short time, and integration and automation of various structures performing individual roles can be realized.

In our research work, we have attempted to design a protein analysis platform which integrates protein separation, fractionation and collection, digestion and preconcentration on a single microchip. Fractionation and collection are indispensable steps for a complex sample. This thesis work focuses on developing an "in-space" protein fractionator and collector, coupled with protein separation upstream and protein concentration downstream. The essence of fractionation in-space is to collect individual components into individual collectors without cross contamination. In this chapter, we will give a review on the different aspects involved in our work.

1.2 Protein analysis on microchip

Proteomics involves protein extraction from cells or tissues, protein separation, fractionation, concentration, digestion and identification by Mass Spectrometry (MS). Some of these processes have been demonstrated on microchips.

1

Protein analysis formats on a microchip fall into two categories, the protein biochip array and microfluidic devices. To construct a protein microarray, protein molecules are immobilized through a crosslinker onto a solid support, such as a glass substrate coated with gold film. The protein array is then exposed to an analyte containing protein molecules or other small molecules which can interact with the immobilized protein molecules. A protein array is an excellent tool to study the interaction of protein with protein [13-15], peptide [16] or target drug molecules [17,18].

The traditional and prevalent protein separation method is 2-D polyacrylamide gel electrophoresis (PAGE) [19-22]. Protein molecules are separated by isoelectric focusing in the first dimension and further separated according to molecular weight in the second dimension. Although 2-D PAGE shows great power in protein separation, it is tedious, time-consuming and hard to automate. In comparison, HPLC and CE demonstrate their great potential in protein separation and the ability to couple with MS, allowing fast and automatic analysis. Numerous papers have been published about protein separation using various mechanisms in a capillary, such as capillary zone electrophoresis (CZE) [23,24], capillary gel electrophoresis (CGE) [25,26], and capillary isoelectric focusing (cIEF) [27-30]. In CZE, CGE, and cIEF, molecules are separated according to their differences in mass-to-charge ratio, size and isoelectric point, respectively. Protein separation was successfully adapted from capillary to microchip after the introduction of microfluidic channels. Both one-dimension and two-dimension protein and peptide separations on microchip have been published. Two-dimensional separation is more powerful for complex sample mixtures. Ramsey *et al* [31,32] integrated micellar electrokinetic chromatography (MEKC) and high-speed open-channel electrophoresis to

2

separate peptides. The plate numbers reached 230 000 and 40 000 for the first and second dimensions, respectively. The speed in the second dimension has to be very high, in order to analyze the separated components injected from the first dimension without losing too many fractions. One of the advantages of "lab on chip" was embodied in that device by the ability to achieve almost zero dead volume of the interconnecting channels. The hyphenation of SDS gel electrophoresis and MEKC (Figure 1.1 a) also demonstrated high resolving power for protein separation [33].

The material involved has been removed because of copyright restrictions. Shadpour *et al* [33] a	The material involved has been removed because of copyright restrictions. Herr *et al* [34] b
The material involved has been removed because of copyright restrictions. Tsai et al [35] c	The material involved has been removed because of copyright restrictions. Li *et al* [36] d
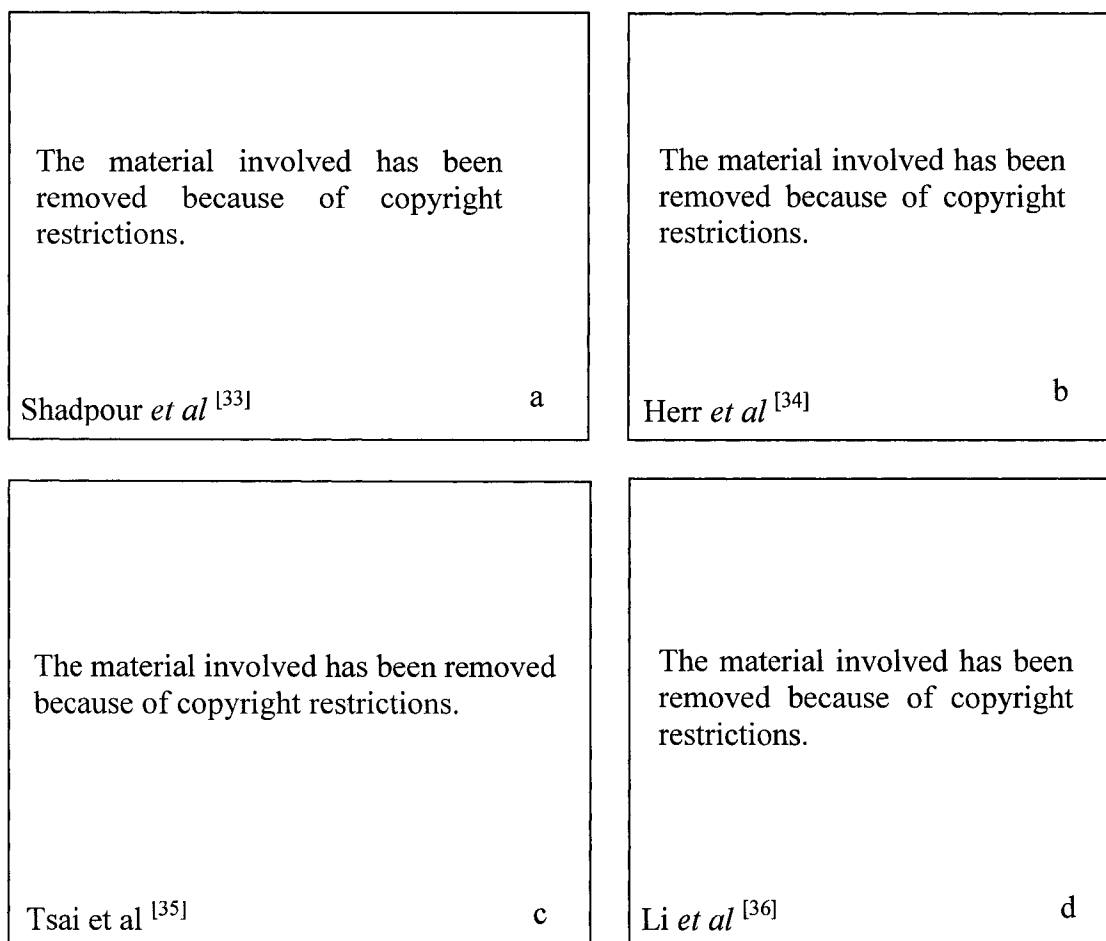
Figure 1.1 Various 2-D designs adapted from literatures

cIEF and CZE in the first and second dimensions, respectively, were carried out on a simple cross channel structure (Figure 1.1 b) [34]. All the 2-D separation modes

3

discussed above have one thing in common. In each case, because the two dimensions were carried out simultaneously, the sample injection frequency from the first dimension to the second should be high enough to avoid loss of sample information. In comparison, by changing the chip design, separations in two dimensions can happen sequentially. Tsai *et al* demonstrated the combination of cIEF and CGE on a glass chip [35] as shown in Figure 1.1 c. They fabricated the cIEF channel and air-gate channels on one layer and the CGE channel on another substrate. The two air-gate channels were employed to reduce the interference between the two dimensions. Similar structures (Figure 1.1d) were made on polycarbonate substrates to perform cIEF and SDS gel electrophoresis in the first and second dimensions, respectively [36]. A 2-D separation employing cIEF and SDS gel on PDMS was also reported [37]. However, this work involved multiple PDMS layers and a complicated procedure involving peeling off one PDMS layer after cIEF before performing the second dimension analysis.

In-solution, on-chip digestion has been presented by Gottschlich *et al* [38]. The protein and trypsin solutions were introduced from different channels into the reaction channel. Because of the autolysis of trypsin, which may interfere with the MS analysis, digestion using immobilized trypsin was developed. Trypsin can be immobilized onto agarose beads and then packed into microchannels [39-41] to perform on-site digestion. Magnetic latex nanoparticles [42] are also a good support for trypsin. The magnetic beads can be easily removed from the microchannels and replaced with new ones. Monolithic porous polymer can also be used as the support [43]. Another interesting way to construct the enzymatic microreactor is to entrap trypsin into a network. The network can be built up by coating the surface of a poly(ethylene terephthalate) chip

4

with positively and negatively charged molecular layers alternately [44], or by grafting sol-gel onto the surface of a PMMA chip through polycondensation [45,46].

Desalting [47] and preconcentration are important steps in protein analysis, and have been realized on chip. Polystyrene beads were packed into microchannels to desalt peptide samples before infusing into the MS [48]. Microdialysis is an efficient method of sample cleanup. Song *et al* [49] fabricated a nanoporous membrane on a microchip through a photopatterning method. A membrane with a molecular weight cutoff less than 5700 was employed to desalt a protein sample. The easiest way of immobilizing a membrane on-chip is demonstrated by just placing a poly (vinylidene difluoride) membrane [50] with 0.45 μm pore in the reservoir. The protein sample was loaded on top of the membrane and desalted. In some cases, desalting and preconcentration can be performed at the same time [51]. Protein concentration on chip has been demonstrated employing classic mechanisms, such as isotachophoresis (ITP) [52], sample stacking [53] and solid phase extraction (SPE) [54], etc. Some interesting concentration methods have been reported recently. Hatch *et al* [55] fabricated a photopatterned size exclusion, nanoporous film, about 50 μm thick. By grounding the sample reservoir and applying a positive voltage to the sample waste reservoir, negatively charged protein molecules were trapped on the film. A similar preconcentration mechanism was presented by Foote *et al* [56]. A porous silica membrane was sandwiched between the substrate and the cover plate. The negatively charged protein molecules were electrophoretically concentrated onto the silica film when a positive voltage was applied between the preconcentrator reservoir and the sample reservoir. A preconcentrator with a million fold concentration capability was reported last year [57]. The concentrator was

5

constructed with a series of nanofluidic filters, fabricated using the normal microfabrication procedures. It took advantage of electrokinetic trapping and nonlinear electroosmotic flow to realize protein concentration.

The hyphenation of a microchip with ESI-MS has been explored thoroughly. Various types of electrospray tips were developed including a capillary tip [41], a polymer tip [58] and a microfabricated tip [59].
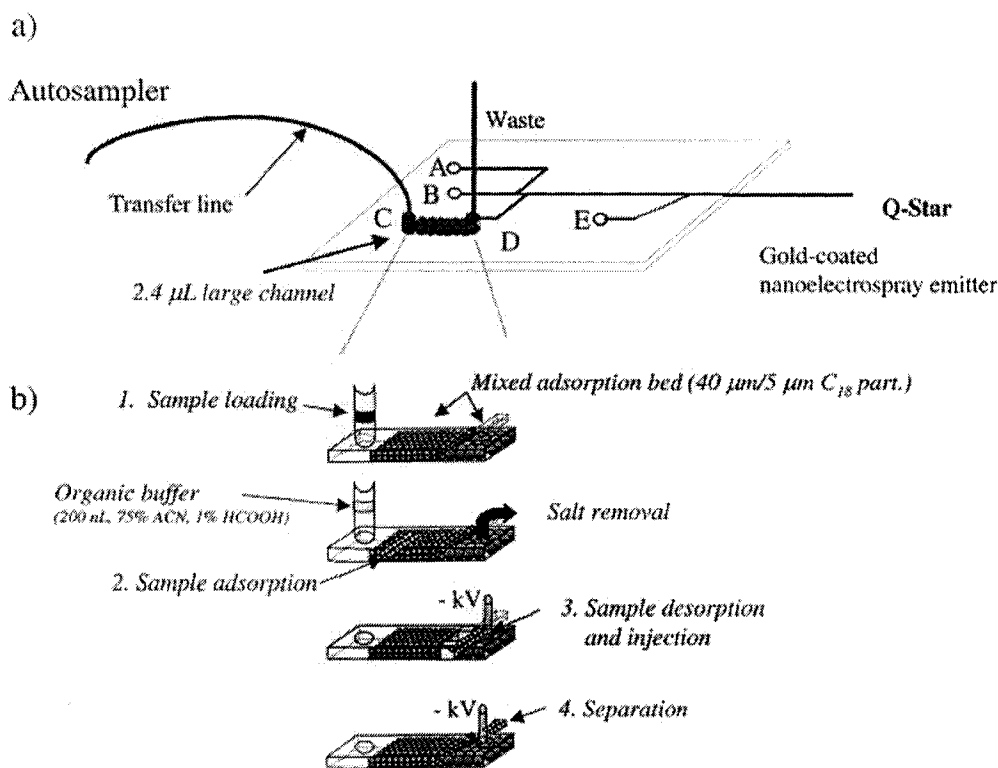
Figure 1.2 Integrated protein platform adapted from Li et al [61].

On the basis of studies on individual procedures involved in protein analysis, some highly integrated systems have been presented such as the nanospray LC/MS chip commercialized by Agilent and a microfluidic platform for LC/MS which integrated pump, valve, separation column and electrospray [60], etc. Li *et al* [61] built up a

6

protein platform (Figure 1.2) on which sample was transferred to microchip through an autosampler, followed by on-chip preconcentration, desalting, separation and identification by MS.

To our knowledge, all the protein analysis platforms reported so far involve a single manifold system. In order to further demonstrate the advantages of the short analysis time and high integration potential of microchips, a multiplexed device needs to be explored. On a multiplexed protein platform, a protein mixture will undergo separation, fractionation and collection, preconcentration, digestion and identification by MS. Since preconcentration and digestion do not occur on the same time scale as separation, an "in space" fractionation and collection design is preferable to integrate the two procedures. The key point of fractionation and collection is how to direct fractions into the desired collection outlets, which is related to flow control. On a microchip, pressure driven flow and electrokinetic flow are the main available sources of flow control.

1.3 Pressure driven flow

Basic principle

Pressure driven flow includes laminar flow and turbulent flow. When a fluid flows in parallel layers [62], and there is no disturbance between the layers, laminar flow is developed. In comparison, turbulent flow is an irregular fluid flow form. The Reynolds number (R_e) is used to evaluate whether the flow is laminar or turbulent. The Reynolds number is defined by

$$R_e = \frac{\rho \upsilon_s L}{\mu}$$

7

where ρ, v_s, L and μ are fluid density, fluid velocity, characteristic length and dynamic fluid viscosity, respectively. Laminar flow occurs when R_e is less than 2000. Because of the small dimension of the microfluidic channels, the flow is almost always laminar. Fully developed laminar flow in small round tubes or microchannels has a parabolic flow profile.

1.4 Electrokinetic driven flow

Electrokinetically driven flow originates from electroosmotic flow (EOF) induced by charged surfaces such as quartz or glass. When a capillary or microchannel is filled with buffer with a pH value above 4.0, the silanol groups on the surface will be ionized and the surface will be negatively charged. The negative charges attract positive charges and form a double layer close to the surface. EOF is created by the movement of the positively charged ions in the double layer towards the cathode which carries the bulk solution with them. The potential at the plane of shear lies in the double layer, and is called the zeta potential. The velocity of EOF (v_{eo}) is described by the Smoluchowski equation [63] as follows,

$$v_{eo} = \frac{\varepsilon \zeta E}{\eta} = \mu_{eo} E$$

where, ε, ζ, η, μ_{eo}, E are the permitivity of the buffer, zeta potential, viscosity of buffer, the electroosmotic mobility and electrical field, respectively. Contrary to the parabolic flow profile arising from pressure driven flow, EOF has a flat profile across the channel which can decrease zone broadening and increase resolution.

Charged particles under an electric field are also driven by an electrophoretic force. The electrophoretic velocity v_{ep} and mobility (μ_{eo}) are given by

$$v_{ep} = \mu_{ep}E = \frac{q}{6\pi\eta r}E$$

where q and r are the charge on the particle and the radius of the particle, respectively. The actual velocity of a charged particle depends on the sum of electroosmotic velocity and electrophoretic velocity.

1.5 Sheath flow and its application

Sheath flow is created when the sample stream is sandwiched between two buffers, on either side. Sheath flow can be created by hydrodynamic focusing or electrokinetic focusing. Sheath flow phenomena have many realistic applications. Lee *et al* [64] described a micromachined flow cytometer based on hydrodynamic focusing. They employed a simulation model to select the possible dimensions of sample and sheath channels. A similar micro flow cytometer was combined with optical detection and microvalves, which were connected to a few outlets to collect cells of interest [65]. Electrokinetic manipulation of cells [66] and electrokinetic focusing on microchips [67] were reported early in 1997, followed by the presentation of a flow cytometer using electrokinetic focusing in 1999 [68]. The basic design for performing electrokinetic focusing involves two channels vertical to each other. One channel is used to introduce a sample stream, while the sheath streams are introduced from either side of the sample channel. The sample stream and sheath streams are driven by electroosmotic and electrophoretic forces towards the same outlet. The flow rates are controlled by the voltages applied and the chip dimensions.

9

1.6 Fractionation and collection on microchip

All the separation methods can be considered as fractionation tools. Here, we focus on some interesting fractionation methods. Elements of these designs are present in the chips designed and presented in this thesis.

1.6.1 Fractionation based on hydrodynamic filtration

Japanese researchers presented a series of papers on the topic of hydrodynamic filtration, referring to it as "pinched flow fractionation" [69] in the first paper. This method takes advantage of laminar flow in microchannels, and does not require an external field. The schematic explanation of this method is shown in Figure 1.3. Liquids

The material involved has been removed because of copyright restrictions.
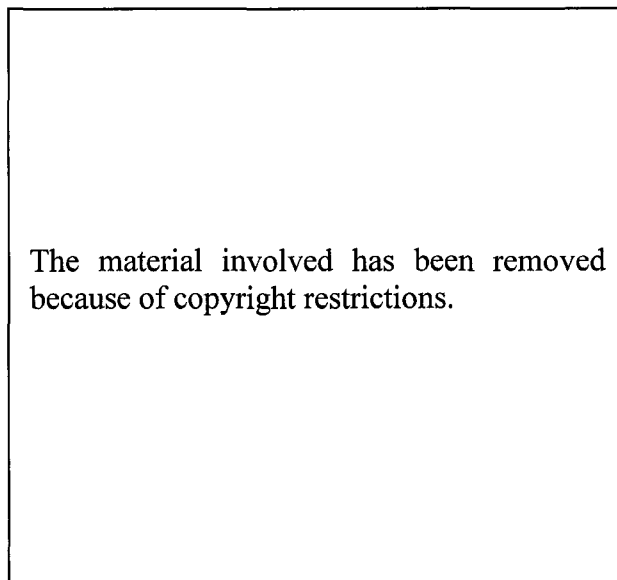
Figure 1.3 Schematic illustration of the mechanism of particle sorting. Adapted from Yamada et al [69].

with and without particles were introduced from two inlets. The suspended particle stream was close to the side wall due to the pinching effect of the other liquid stream. When the particle stream reached the expanded region, small particles still flowed close to the channel wall, whereas large particles flowed towards the center. In their

10

following papers, Yamada and Seki explained the separation mechanism more explicitly, defining this method as hydrodynamic filtration [70].

The design used multiple side channels as outlets. The particles flow direction depends on the ratio of the flow rate of the side channel to that of the main channel. As shown in Figure 1.4 (a), the flow rate of the side channel was so small that no particle entered the side channel. In Figure 1.4 (b) and (c), as the flow rate in the side channels increased, particles with larger sizes could flow into the side channels. However, small particle streams may contaminate the large particle streams because not all the particles are aligned to the channel wall. In the later design [71], side channels used for splitting and recombining were added to improve recovery and selectivity. Valves were also integrated into the side channels to control the flow rates of the side channels in order to realize tunable pinched flow fractionation [72].

The material involved has been removed because of copyright restrictions.
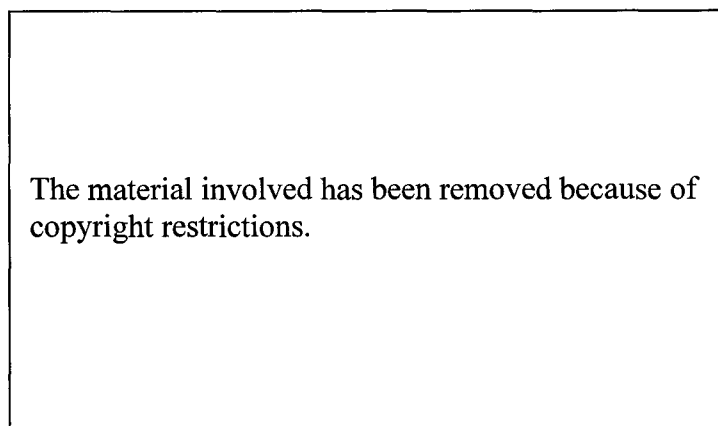
Figure 1.4 Schematic illustration of hydrodynamic filtration. Adapted from Yamada et al [70].

1.6.2 Field flow fractionation based on isoelectric focusing

Field flow fractionation (FFF), presented first by Thompson [73], is a continuous mode of separation. Briefly, in field flow fractionation, the sample stream is pumped

11

into a thin channel by pressure, forming a parabolic flow, while a field perpendicular to the flow direction is applied. Because of the interaction with that field, sample components are forced towards the channel wall. Different interactions with the field result in different velocities of individual sample components, separating sample components into different zones along the channel wall. Various FFF modes have been developed depending on the types of field, including sedimentation FFF [74], magnetic FFF [75], thermal FFF [76], dielectrophoresis FFF [77] and IEFFFF [78].

IEF has proven to be an efficient protein separation tool. The first report about combining IEF with FFF was published in 1989 [78]. In that work, the ampholyte was pumped into the channel to form a pH gradient. However, in some cases, ampholyte should be avoided because it might interfere with the detection of protein. In this circumstance, carrier-free IEF is recommended. Yager *et al* [79] reported ampholyte-free IEFFFF (Figure 1.5). In this design, gold or palladium was used to construct the two channel walls in which the sample stream was sandwiched. The pH gradient was formed by OH⁻ and H⁺ produced from electrolysis of water.
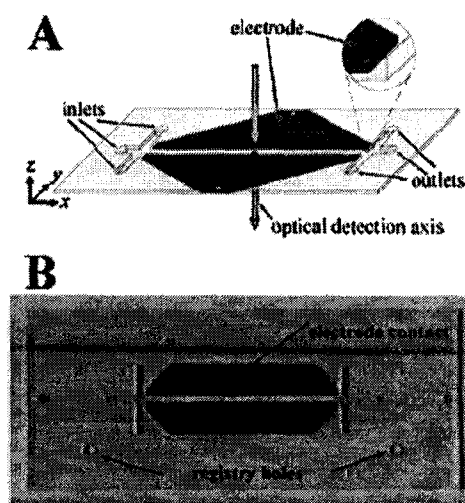
Figure 1.5 Chip design for IEFFFF. Adapted from Macounova et al [79].

12

Han *et al* [80] reported a novel way of generating a pH gradient in order to perform IEFFFF. The pH gradient originated from a diffusion potential, as shown in Figure 1.6. This method does not involve ampholyte or even an electric field. A sample solution with a lower buffer concentration and pH value compared to the background buffers was introduced from the middle channel. Because Na^+ has a higher diffusion coefficient than $H_2PO_4^-$ and HPO_4^{2-} ions, a positive diffusion potential was formed in the sample solution. The electric field produced from the diffusion potential over a small distance is enough to focus protein molecules. The protein molecules with pI values between 6 and 8 were positively charged and focused at the positions corresponding to their pI values.
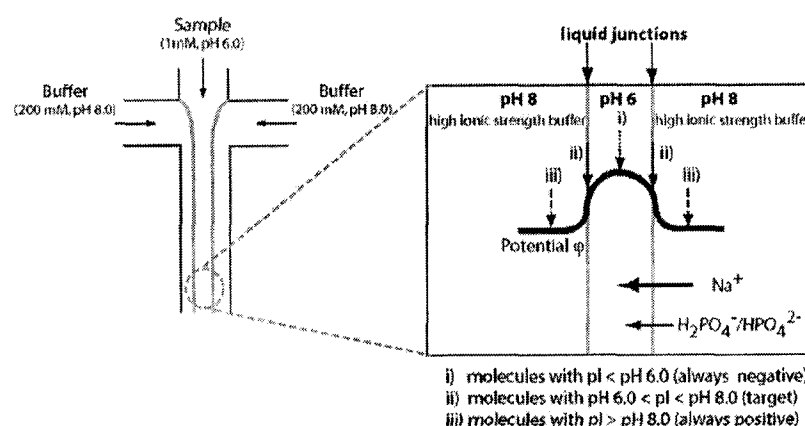
Figure 1.6 Schematic illustration of diffusion potential induced pH gradient. Adapted from Song et al [80].

1.6.3 Optical fractionation and particle deterministic lateral displacement

MacDonald *et al* [81] reported particle sorting using an optical lattice. This method is based on the change in particle kinetic motion when it is illuminated by light, and on the laminar flow in a microchannel. As shown in Figure 1.7 (a), when no disturbance happens, particles will flow from B to D. However, when an optical lattice is coupled to

13

the fractionation chamber, some particles will be pushed up by interacting with light and will flow into C.

Another novel separation method based on deterministic lateral displacement was presented by Huang *et al* [82]. In traditional particle separation methods like size exclusion and hydrodynamic chromatography, the collected peaks are usually broad because particles with the same size will travel close to each other, but not the same distance, before they reach the detector. In Huang's work, an obstacle array (Figure 1.7(b)) was built in a microchip. Particles with the same size traveled along the same path, which increased the resolution.

The material involved has been removed because of copyright restrictions.	The material involved has been removed because of copyright restrictions.
(a)	(b)
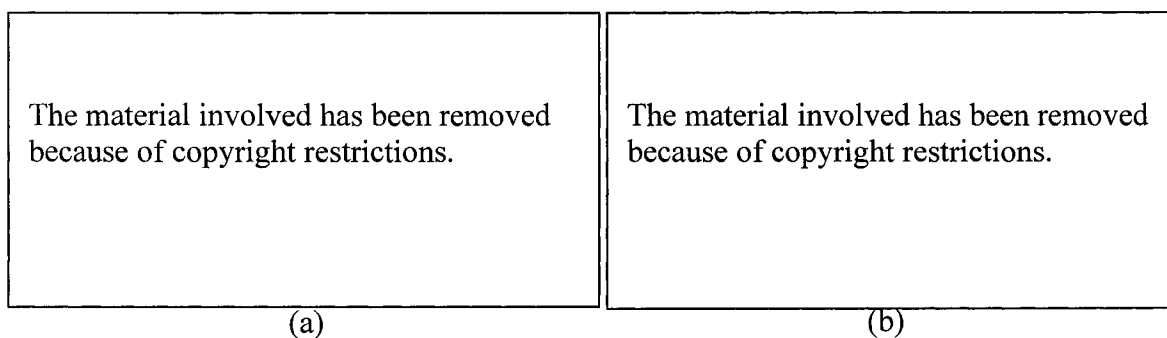
Figure 1.7 Schematic illustration of optical fractionation (a). Adapted from MacDonald et al [81]. Particle separation based on deterministic lateral displacement (b). Adapted from Huang et al [82].

1.6.4 Fraction collection

Fraction collection in capillary format [83-85] has been reported. Yet few papers were published about fraction collection on microchip. In this section, we will give a brief review of fraction collection designs and flow switching methods in the field of microfabrication.

14

For a design which has only one collection outlet, the collection ability is limited. So, a strategy needed to be devised to collect fractions individually. Khandurina *et al* [86,87] reported DNA fraction collection using a simple cross-channel design. Sample introduction, separation and collection were driven by an electrokinetic force. The voltage scheme for each step is shown in Figure 1.8. In the fraction collection step, reservoir **1** was applied with a positive voltage and the voltages on reservoir **2** and **3** were decreased. The desired fraction passed the cross section point and was collected by

The material involved has been removed because of copyright restrictions.

Figure 1.8 Schematic illustration of flow directions and voltages applied in sequential stages. Adpated from Khandurina et al [86].

reservoir **3**, while the flow direction below the cross section point was reversed a little, so that other fractions remained in the channel. Thus, the desired fraction would not be contaminated by other fractions. In comparison, if the separation channel and fraction collection channel are separated, the two processes can be performed independently. The application of a nanofilm [88,89] can solve this problem. Tulock *et al* [90] reported a gateable fraction collection design for a mass-limited sample. A nanofilm was placed between a separation channel and a collection channel, which was perpendicular to it. The solutions in both channels would not mix together due to the nanofilm. However,

15

under an electrokinetic force, sample was transferred from the separation to the fraction collection channel. Moreover, a detector placed just before the cross section point was used to monitor the arrival of the targeted fractions to trigger the fraction collection process.

For fraction collection designs with multiple outlets, the collection capacity is increased. However, methods to control flow switching into each collection outlet remain an issue. Mainly three types of forces, pressure, electrokinetic and centrifugal force, have been employed.

Lee *et al* [91] designed a flow switching system (Figure 1.9 (a)) involving a series

(a)   (b)
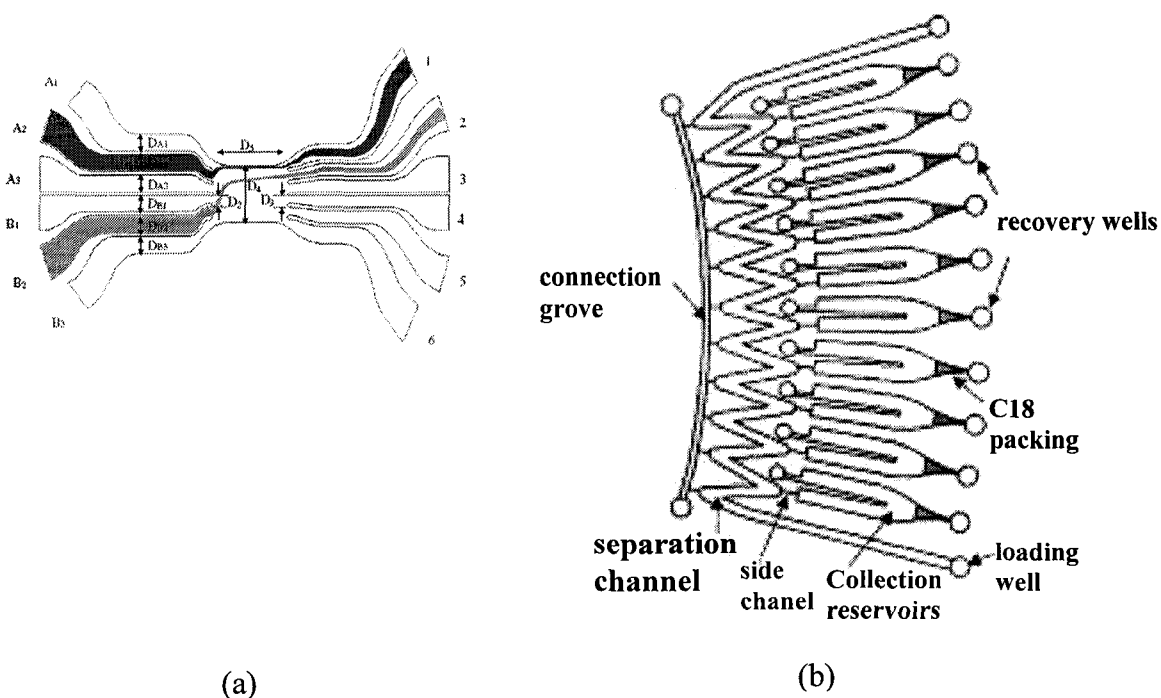
Figure 1.9 (a) Schematic illustration of direction of sample streams into desired outlets by pressure-driven force. Adapted from Lee et al [91]. (b) Fraction collection design based on centrifugal force. Adapted from Spešny et al [92].

of pressure pumps. As shown in Figure 1.9 (a), in order to direct the sample streams introduced from A2 and B2 into specific outlets on the right side, the flow velocities of

16

all the inlet channels need to be controlled accurately, by adjusting the pressure pumps. The flow velocities required were evaluated using models that considered the fluid densities in individual channels and the channel dimensions, before setting up the pressure pumps. Obviously, this is a complex process and the entire system is bulky due to the requirement of several pressure pumps.

Foret *et al* [92] presented a complex fraction collection design (Figure 1.9 (b)) employing centrifugal force. The separation channel was in serpentine shape where isotachophoresis or isoelectric focusing could occur. The separation channel was modified to be hydrophilic. In order to avoid leakage from the separation channel to collection reservoirs through the side channels which connected them together, hydrophobic patches were placed at the junctions. After the separation, the focused sample zones were transferred into collection reservoirs by applying a centrifugal force strong enough to overcome the restriction of the hydrophobic patches.

The material involved has been removed because of copyright restrictions.	The material involved has been removed because of copyright restrictions.
a	b
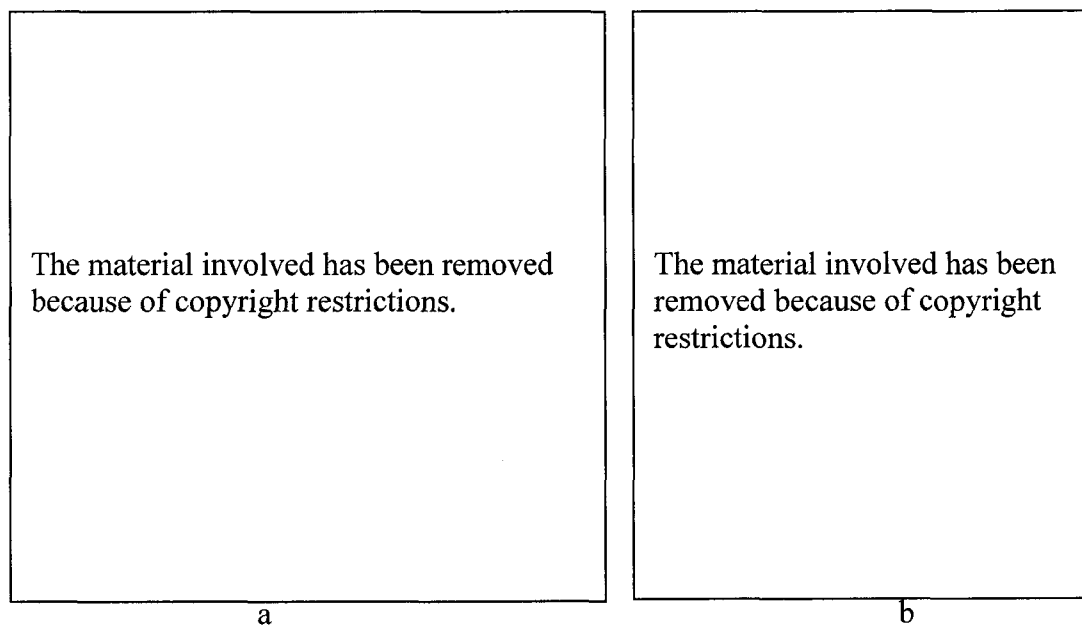
Figure 1.10 (a) Design for multiple injections. Adapted fromFu et al [93]. (b) Design for multiple injections involving less electrodes than the design in (a). Adapted from Pan et al [94].

17

Compared to pressure-driven flow, electrokinetically driven flow does not require movable parts and flow switching can be easily controlled by switching voltages. These advantages make electokinetically driven flow a useful driving force in fraction collection devices. Fu *et al* [93] reported a multiple injection method based on an electrokinetic pinching effect. In their device (Figure 1.10 a), two sample streams introduced from two inlets were supposed to be directed into two outlets from A to G. A simulation model was required to estimate the required voltages on each reservoir. Although the two sample streams flowed into the desired channels, the reservoirs from A to E needed to have voltages of different values applied, which made the entire system cumbersome. Moreover, EOF on the channel surface changes with time due to adsorption of sample onto the wall of the microchannel. For such a complex system in which the flow direction was so sensitive to slight changes in voltages (as shown in their data), change in EOF means readjustment of all the voltages. Pan *et al* [94] reported a simple version (Figure 1.10 b) based on the same principle. In their device, sample streams were introduced from **B** and **D**. Reservoirs **A** to **E** received positive voltages, and one or two reservoirs from **1** to **5** were grounded, depending on which reservoir the sample streams were supposed to flow into.
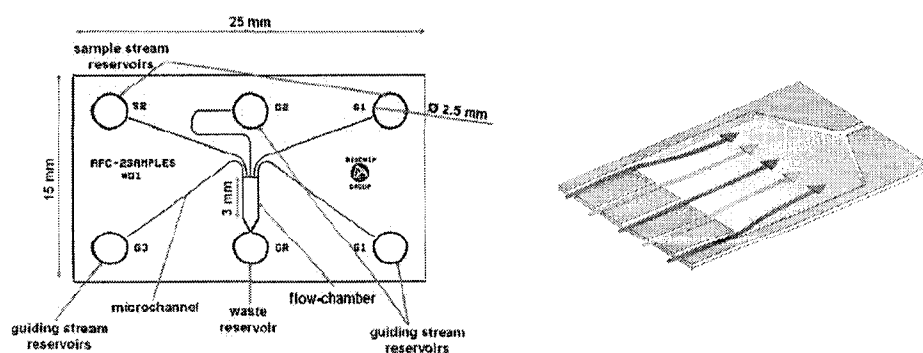
Figure 1.11 Chip design for performing address flow (left) and schematic illustration of address flow in the chamber (right). Adapted from Besselink et al [95].

18

The electrokinetic effect was also being used to produce so-called "address flow" as reported by Besselink *et al* [95,96]. They demonstrated flow control for one and two sample streams, respectively. To control two sample streams, three guiding streams were employed as shown in Figure 1.11. The positions of the two sample streams in the flow chamber were adjusted by changing the voltage settings on the sample stream reservoir and guiding stream reservoirs. They considered the device as a combination of electrical resistors and developed an analog model which was combined with the Labview program to change the voltage settings in real time.

1.7 Capillary isoelectric focusing

Isoelectric focusing (IEF) has been extensively used in 2-D SDS PAGE separation of proteins. Here, we only focus on IEF in capillary or microchannel format which is called cIEF. Traditionally, in order to form a pH gradient in a capillary, ampholyte and two buffers with different pH values are needed. The acidic buffer (anolyte) and basic buffer (catholyte) are placed at the anodic and cathodic ends, respectively. An ampholyte consists of numerous compounds with different pI values. In cIEF, the mixture of sample and ampholyte is introduced into a capillary. Upon application of an electric field, a charged ampholyte molecule will move towards the anode or cathode, depending on its charge, until the net charge at that spatial region of the ampolyte is zero, and then it stops at that position. If it moves away from that position due to diffusion and is charged again, it will move back. Numerous ampholyte molecules are distributed in the capillary according to their pI values and a pH gradient is generated.

19

Protein molecules will move to the positions of their own pI values and then be concentrated at those positions into narrow zones.

In cIEF, the step of driving focused protein zones past the detector is called mobilization. In two-step IEF, focusing and mobilization occur in separate stages, while in one-step IEF, the two steps proceed simultaneously. The mobilization can be performed in three ways. In chemical mobilization [97], adding some neutral salts to the anolyte or catholyte will lead to a pH shift in the capillary, and the focused zone moves out of the capillary. In hydraulic mobilization, pressure is needed to push the focused zone past the detector, while keeping the electric field on [98]. Electroosmotic mobilization is normally used in one-step IEF. EOF has to be partially removed in order not to interfere with focusing too much and the residual EOF serves as the mobilization force [99]. In contrast, in two-step IEF the capillary wall needs to be modified to remove EOF completely.

One of the main problems in cIEF is that the mobilization might deform the focused zone. To avoid this issue, Pawliszyn *et al* [100, 101] developed a whole column imaging detection system to monitor the focusing process over a long distance. Another problem arises from the ampholyte. The ampholyte can easily be adsorbed onto the capillary or channel wall and thus EOF is changed. Moreover, ampholyte is not compatible with mass spectrometry (MS), yet it is hard to separate from the protein. Various ways of developing pH gradients have been presented. Cabrera *et al* [102] reported the generation of a pH gradient by electrolysis of water. Thermally formed pH gradients were investigated by Fang [103] and Huang [104]. A tapered channel was used in their work. When a current flowed in this channel, the Joule heat generated at

20

the sharper region was higher than that at the wider part. When the channel was filled

up with weak acid or base, the dissociation constant would change with temperature,

thus forming a pH gradient in the channel.

1.8 Monolithic polymer

Monolithic polymers have found extensive applications on microchips. They can

be used to make microreactors [105], concentrators [106], electroosmotic micropumps

[107], and electrospray tips [108], etc. The polymerization reaction involves monomer,

cross linker, initiator and porogens. The pore size can be adjusted by changing the

amount of individual components [109]. The reaction can be initiated by heat [110] or

UV light. Compared to thermal polymerization, photo initiated polymerization is more

useful because the polymerization reaction can be confined into a specific region with

the aid of an exposure mask [111,112]. Reichmuth *et al* [113] fabricated a micro reactor

and reversed phase column for protein separation using laser polymerization. Half of

the volume of the microinjector was filled with polymer. The monolithic polymer could

be driven to move from one end to the other by pressure. The movement caused the

introduction of sample quantitatively, followed by separation. A photopolymerized

silica based sol-gel with EOF can also be packed into a microchannel as separation

media [114, 115]. Separation of peptides and amino acids using electrochromatography

were demonstrated by Throckmorton *et al* [116]. 2-acrylamido-2-methyl-1-

propanesulfonic acid (AMPS) was added to the monomer solution in order to increase

EOF.

21

Monolithic polymer is an excellent media for solid phase extraction (SPE) and preconcentration because of its high surface to volume ratio. Yu *et al* [117] demonstrated the concentration of recombinant green fluorescent protein on a hydrophobic polymer bed. Yang *et al* [118,119] reported the extraction of imipramine in human urine sample using a similar polymer bed followed by detection with MS. A monolithic polymer can be employed as support for microreactors. One of the examples is a trypsin digestion microreactor. Traditional trypsin digestion is performed in solution and is time-consuming, because the concentration of trypsin has to be kept at a low level, otherwise autodigestion will affect the identification of targeted proteins. Trypsin can be immobilized onto a polymeric support in various ways. When glycidyl methacrylate (GMA) is introduced to the polymeric structure, the epoxide functional group of GMA can react with the primary amino group of trypsin to immobilize trypsin [120]. Dulay *et al* [121] modified a sol-gel monolith with alkoxysilane containing an aldehyde group, which reacts with an inactive amine group of trypsin. Kato *et al* [122,123] reported immobilization of trypsin by forming a trypsin film on a sol-gel monolith. Xie [124] and Peterson *et al* [125] immobilized trypsin by coupling azlactone moiety into a polymeric structure which can react with the amine group of trypsin.

1.9 pSpice simulation

Because the fabrication of microfluidic devices, especially devices on glass substrates, is usually time-consuming and expensive, it is useful to first model the flow behavior before fabricating the chip. So far, a few simulation tools for microfluidics are available. In our study, we are particularly concerned with the sample stream width,

22

because it affects the required width of the main channel. Details about how to calculate the sample width can be found in chapter 2. We need to consider the volumetric flow rates of sheath streams and sample streams, which depend on the electoosmotic flow rates. As long as all the channels were prepared under the same conditions, and the sample buffer is the same as the sheath buffers, it can be assumed that the surface charges over the entire device are uniform. Thus, the electroosmotic flow is proportional to the electric field in each channel. If each portion of the channel is treated as an electrical resistor, upon applying voltages to specific reservoirs, the electric field can be calculated according to Kirchhoff's law. When the chip design becomes complex, a simulation tool is necessary. pSpice software available from Cadence can perform this job easily. The simulation gives the current in each channel segment, which is proportional to the volumetric flow. The voltage at each node allows us to calculate the electric fields. pSpice software can also be used to simulate the hydrodynamic flow rate. Flow resistance and pressure correspond to electrical resistance and voltage, respectively. Because a pSpice simulation is based on an electrical model, all the parameters have to be converted to a form of electrical parameter. Although a pSpice simulation cannot give flow profile information, it is not time-consuming when compared with other simulation methods. Moreover, in our experiment, it gives enough information to direct the chip design.

1.10 Thesis scope

Chapter 2 focuses on fundamental design studies to establish good sheath flow conditions. In order to deliver sample stream into a specific fractionation channel

23

without contaminating other channels, electrokinetic focusing was employed to pinch the sample stream. To distribute as many fractionation channels as possible, the pinched sample stream needs to be long enough. The chip design was revised and tested several times until finally 8 fractionation channels were functional. Design work then allowed us to estimate that more channels can be accommodated.

Chapter 3 demonstrates fractionation and selective collection of separated protein components. The high purity of collected fractions proves the efficiency of this fractionator and collector.

In Chapter 4, the number of fractionation channels is expanded to 36. Electrokinetic focusing and hydrodynamic flow in this multiplexed design were investigated. The pinching effect still worked well, even when the pinched sample stream traveled as far as 2.75 mm.

In Chapter 5, our attempt to make monolithic polymer beds, in order to concentrate protein in the multiplexed fractionator, is described. The challenge was that the introduction of polymer increased flow resistance significantly, and thus the sheath flow effect did not work well. Different reaction mixtures and chip dimensions were tested until conditions were found for which the polymer beds did not affect the sheath flow.

Chapter 6 focuses on the study of one-step IEF condition on these fractionators. IEF performance was found to relate to chip dimensions, sample components, and the concentration of anolyte and catholyte. The same conditions which produced good IEF results on a simple fractionator were not working well on the highly multiplexed fractionator. IEF may not be a suitable separation method for coupling to these fractionators.

24

Chapter 7 briefly discusses future work.

1.11 Reference

1   Cooper, J.W.; Chen, J.; Li, Y.; Lee, C.S. *Anal. Chem.* **2003**, 75, 1067-1074.
2   Wheeler, A.R.; Moon, H.; Bird, C.A.; Loo, R.R.O.; Kim, C.J.; Loo, J.A.; Garrell, R.L. *Anal. Chem.* **2005**, 77, 534-540.
3   Lion, N.; Gellon, J.O.; Jenson, H.; Girault, H.H. *J. Chromatogr. A* **2003**, 1003, 11-19.
4   Zhou, F.; Johnston, M.V. *Anal. Chem.* **2004**, 76, 2734-2740.
5   Li, J.; Thibault, P.; Bings, N.H.; Skinner, C.D.; Wang, C.; Colyer, C.; Harrison, D.J. *Anal. Chem.* **1999**, 71, 3036-3045.
6   Wang, H.; Chen, J.F.; Zhu, L.; Shadpour, H.; Hupert, M.L; Soper, S.A. *Anal. Chem.* **2006**, 78, 6223-6231.
7   Liu, C.N.; Toriello, N.M.; Mathies, R.A. *Anal. Chem.* **2006**, 78, 5474-5479.
8   Lee, J.G.; Cheong, K.H.; Huh, N.; Kim, S.; Choi, J.W.; Ko, C. *Lab on a chip* **2006**, 6, 886-895.
9   Tabuchi, M.; Baba, Y. *J. of Proteome Research* **2004**, 3, 871-877.
10   Lin, Y.C.; Huang, M.Y. *J. Micromech. Microeng.* **2001**, 11, 542-547.
11   Lazar, I.M.; Trisiripisal, P.; Sarvaiya, H.A. *Anal. Chem.* **2006**, 78, 5513-5524.
12   Christodoulides, N.; Mohanty, S.; Miller, C.S.; Langub, M.C.; Floriano, P.N.; Dharshan, P.; Ali, M.F.; Bernard, B.; Romanovicz, D.; Anslyn, E.; Fox, P.C.; McDevitt, J.T. *Lab on a chip* **2005**, 5, 261-269.
13   Ro, H.; Koh, B.H.; Jung, S.O.; Park, H.K.; Shin, Y.; Kim, M.; Chung, B.H. *Proteomics* **2006**, 6, 2108-2111.
14   Tsai, C.S.; Yu, T.B.; Chen, C.T. *Chem. Comm.* **2005**, 4273-4275.
15   Swietnichi, W.; O'Brien, S.; Holman, K.; Cherry, S.; Brueggemann, E.; Tropea, J.E.; Hines, H.B.; Waugh, D.S.; Ulrich, R.G. *J. Biol. Chem.* **2004**, 279, 38693-38700.
16   Kitada, S.; Ito, A. *J. Biochem.* **2001**, 129, 155-161.
17   Arnell, R.; Ferraz, N.; Fornstedt, T. *Anal. Chem.* **2006**, 1682-1689.
18   Miao, B.C.; Geng, M.Y.; Li, J.; Li, F.C.; Chen, H.X.; Guan, H.S.; Ding, J. *Biochemical pharmacology* **2004**, 68, 641-649.
19   Garcillan, D.A.; Gomez-Esquer, F.; Diaz-Gil, G.; Martinez-Arribas, F.; Delcan, J.; Schneider, J.; Palomar, M.A.; Linares, R. *Proteomics* **2005**, 5, 4946-4957.
20   Micheahamzehpour, M.; Sanchez, J.C.; Epp, S.F.; Paquet, N.; Hughes, G.J.; Hochstrasser, D.; Pechere, J.C. *Enzyme &Protein* **1993**, 47, 1-8.
21   Prat, O.; Berenguer, F.; Malard, V.; Tavan, E.; Sage, N.; Steinmetz, G.; Quemeneur, E. *Proteomics* **2005**, 5, 297-306.
22   Mears, R.; Craven, R.A.; Hanrahan, S.; Totty, N.; Upton, C.; Young, S.L.; Patel, P.; Selby, P.J.; Banks, R.E. *Proteomics* **2004**, 4, 4019-4031.
23   Keough, T.; Takigiku, R.; Lacey, M.P.; Purdon, M. *Anal. Chem.* **1992**, 64, 1594-1600.
24   Figeys, D.; van Oostveen, I.; Ducret, A.; Aebersold, R. *Anal. Chem.* **1996**, 68, 1822-1828.

25   Szilagyi, A.; Blasko, B.; Ronai, Z.; Fust, G.; Sasvari-Szekely, M.; Guttman, A. *Electrophoresis* **2006**, 27, 1437-1443.

26   Grady, J.K.; Zang, J.; Laue, T.M.; Arosio, P.; Chasteen, N.D. *Anal. Biochem.* **2002**, 302, 263-268.

27   Kang, D.J.; Moon, M.H. *Anal. Chem.* **2006**, 78, 5789-5798.

28   Liu, Z.; Pawliszyn, J. *Anal. Chem.* **2005**, 77, 165-171.

29   Tang, S.; Nesta, D.P.; Maneri, L.R.; Anumula, K.R. *J. Pharmaceutical and Biomedical Analysis* **1999**, 19, 569-583.

30   Sze, N.S.K.; Huang, T.M.; Pawliszyn, J. *J. Sep. Sci.* **2002**, 25, 1119-1122.

31   Rocklin, R.D.; Ramsey, R.S.; Ramsey, J.M. *Anal. Chem.* **2000**, 72, 5244-5249.

32   Ramsey, L.D.; Jacobson, S.C.; Culbertson, C.T.; Ramsey, J.M. *Anal. Chem.* **2003**, 75, 3758-3764.

33   Shadpour, H.; Soper, S.A. *Anal. Chem.* **2006**, 78, 3519-3527.

34   Herr, A.E.; Molho, J.I.; Drouvalakis, K.A.; Mikkelsen, J.C.; Utz, P.J.; Santiago, J.G.; Kenny, T.W. *Anal. Chem.* **2003**, 75, 1180-1187.

35   Tsai, S.; Loughran, M.; Karube, I. *J. Micromech. Microeng.* **2004**, 14, 1693-1699.

36   Li, Y.; Buch, J.S.; Rosenberger, F.; DeVoe, D.L.; Lee, C.S. *Anal. Chem.* **2004**, 76, 742-748.

37   Chen, X.; Wu, H.; Mao, C.; Whitesides, G.M. *Anal. Chem.* **2002**, 74, 1772-1778.

38   Gottschlich, N.; Culbertson, C.T.; McKnight, T.E. *J. Chromatogr. B* **2000**, 745, 243-249.

39   Jin, L.J.; Ferrance, J.; Sanders, J.C.; Landers, J.P. *Lab on a Chip* **2003**, 3, 11-18.

40   Yue, G.E.; Roper, M.G.; Balchunas, C.; Pulsipher, A.; Coon, J.J.; Shabanowitz, J.; Hunt, D.F.; Landers, J.P.; Ferrance, J.P. *Analytica Chimica Acta* **2006**, 564, 116-122.

41   Wang, C.; Oleschuk, R.; Ouchen, F.; Li, J. Thibault, P. *Rapid Commun. Mass Spectrom.* **2000**, 14, 1377-1383.

42   Slovakova, M.; Minc, N.; Bilkova, Z.; Smadja, C.; Faigle, W.; Futterer, C.; Taverna, M.; Vivoy, J. *Lab on a Chip*, **2005**, 5, 935-942.

43   Peterson, D.S.; Rohr, T.; Svec, F.; Frechet, J.M.J. *Anal. Chem.* **2002**, 74, 4081-4088.

44   Liu, Y.; Lu, H.; Zhong, W.; Song, P.; Kong, J.; Yang, P.; Girault, H.H.; Liu, B. *Anal. Chem.* **2006**, 78, 802-808.

45   Huang, Y.; Shan, W.; Liu, B.; Liu, Y.; Zhang Y.; Zhao, Y.; Lu, H.; Tang, Y.; Yang, P. *Lab on a Chip* **2006**, 6, 534-539.

46   Qu, H.; Wang, H.; Huang, Y,; Zhong, W.; Lu, H.; Kong, J.; Yang, P.; Liu, B. *Anal. Chem.* **2004**, 76, 6426-6433.

47   Silvertand, L.H.H.; Machtejevas, E.; Hendriks, R.; Unger, K.K.; van Bennekom, W.P.; de Jong, G.J. *J. Chromatogr. B* **2006**, 839, 68-73.

48   Lindberg, P.; Dahlin, A.P.; Bergström, S.K.; Thorslund, S.; Andrén, P.E.; Nikolajeff, F.; Bergquist, J. *Electrophoresis* **2006**, 27, 2075-2082.

49   Song, S.; Singh, A.K.; Shepodd, T.J.; Kirby, B.J. *Anal. Chem.* **2004**, 76, 2367-2373.

50   Lion, N.; Gobry, V.; Jensen, H.; Rossier, J.S.; Girault, H. *Electrophoresis* **2002**, 23, 3583-3588.

51 Dahlin, A.P.; Bergström, S.K.; Andrén, P.E.; Markides, K.E.; Berquist, J. *Anal. Chem.* **2005**, 77, 5356-5363

52 Grass, B.; Hergenroder, R.; Neyer, A.; Siepe, D. *J. sep. Sci.* **2002**, 135-140.

53 Li, J.; Wang, C.; Kelly, J.F.; Harrison, D.J.; Thibault, P. *Electrophoresis*, **2000**, 21, 198.

54 Yu, C.; Davey, M.H.; Scev, F.; Frechet, J.M. *Anal. Chem.* **2001**, 73, 5088.

55 Hatch, A.V.; Herr, A.E.; Throckmorton, D.J.; Brennan, J.S.; Singh, A.K. *Anal. Chem.* **2006**, 78, 4976-4984.

56 Foote, R.S.; Khandurina, J.; Jacobson, S.C.; Ramsey, J.M. *Anal. Chem.* **2005**, 77, 57-63.

57 Wang, Y.C.; Stevens, A.L.; Han, J. *Anal. Chem.* **2005**, 77, 4293-4299.

58 Bedair, M.F.; Oleschuk, R.D. *Anal. Chem.* **2006**, 78, 1130-1138.

59 Fortier, M.; Bonneil, E.; Goodley, P.; Thibault, P. *Anal. Chem.* **2005**, 77, 1631-1640.

60 Lazar, L.M.; Trisiripisal, P.; Sarvaiya, H.A. *Anal. Chem.* **2006**, 78, 5513-5524.

61 Li, J.; LeRiche, T.; Tremblay, T.; Wang, C.; Bonneil, E.; Harrison, D.J.; Thibault, P. *Molecular & Cellular Proteomics* **2002**, 1, 157-168.

62 http://en.wikipedia.org

63 Smoluchowski, M.V. *Bull. Int. Acad. Sci. Cracovie* **1903**, 184.

64 Lee, G.B.; Hung, C.I.; Ke, B.J.; Huang, G.R.; Hwei, B.H.; Lai, H.F. *J. Fluids Engineering* **2001**, 123, 672-679.

65 Yang, S.Y.; Hsiung, S.K.; Hung, Y.C.; Chang, C.M.; Liao, T.L.; Lee, G.B. *Meas. Sci. and Technol.* **2006**, 17, 2001-2009.

66 Li, P.C.H.; Harrison, D.J. *Anal. Chem.* **1997**, 69, 1564-1568.

67 Jacobson, S.C.; Ramsey, J.M. *Anal. Chem.* **1997**, 69, 3212-3217.

68 Schrum, D.P.; Culbertson, C.T.; Jacobson, S.C.; Ramsey, J.M. *Anal. Chem.* **1999**, 71, 4173-4177.

69 Yamada, M.; Nakashima, M.; Seki, M. *Anal. Chem.* **2004**, 76, 5465-5471.

70 Yamada, M.; Seki, M. *Lab on a Chip* **2005**, 5, 1233-1239.

71 Yamada, M.; Seki, M. *Anal. Chem.* **2006**, 78, 1357-1362.

72 Sai, Y.; Yamada, M.; Yasada, M.; Seki, M. *J. Chromatogr. A* **2006**, 1127, 214-220.

73 Thompson, G.H.; Myers, M.N.; Giddings, J.C. *Anal. Chem.* **1969**, 41, 1219-1222.

74 Giddings, J.C.; Yang, F.J.F.; Myers, M.N. *Anal. Chem.* **1974**, 46, 1917-1924.

75 Vickrey, T.M.; Garcia-Ramirez, J.A. *Sep, Sci. Technol.* **1980**, 15, 1297-1304.

76 Edwards, T.L.; Gale, B.K.; Frazier, A.B. *Anal. Chem.* **2002**, 74, 1211-1216.

77 Markx, G.H.; Pethig, R.; Rousselet, J. *J. Phys. D. Appl. Phys.* **1997**, 30, 2470-2478.

78 Ng, P.K.W.; Slominski, E.; Johnson, W.J.; Bushuk, W. *Cereal Chemistry* **1989**, 66, 536-537.

79 Macounova, K.; Cabrera, C.R.; Yager, P. *Anal. Chem.* **2001**, 73, 1627-1633.

80 Song, Y.; Hsu, S.; Stevens, A.L.; Han J. *Anal. Chem.* **2006**, 78, 3528-3536.

81 MacDonald, M.P.; Spalding, G.C.; Dholakia, K. *Nature*, **2003**, 426, 421-424.

82 Huang, L.R.; Cox, E.C.; Austin, R.H.; Sturm, J.C. *Science*, **2004**, 304, 987-990.

83 Boss, H.J.; Rohde, M.F.; Rush, R.S. *Anal. Biochem.* **1995**, 231, 123-129.

84 Irie, T.; Oshida, T.; Hasegawa, H.; Matsuoka, Y.; Li, T.; Oya, Y.; Tanaka, T.; Tsujimoto, G.; Kambara, H. *Electrophoresis*, **2000**, 21, 367-374.

85 Guttman, A.; Cohen, A.S.; Heiger, D.N.; Karger, B.L. *Anal. Chem.* **1990**, 62, 137-141.

86 Khandurina, J.; Guttman, A. *J. Chromatogr. A* **2002**, 979, 105-113.

87 Khandurina, J.; Chovan, T.; Guttman A. *Anal. Chem.* **2002**, 74, 1737-1740.

88 Cannon Jr., D.M.; Kuo, T.C.; Bohn, P.W.; Sweedler, J.V. *Anal. Chem.* **2003**, 75, 2224-2230.

89 Kuo, T.C.; Cannon, D.M.; Chen, Y.; Tulock, J.J.; Shannon, M.A.; Sweedler, J.; Bohn, P.W. *Anal. Chem.* **2003**, 75, 1861-1867.

90 Tulock, J.J.; Shannon, M.A.; Bohn, P.W.; Sweedler, J.V. *Anal. Chem.* **2004**, 76, 6419-6425.

91 Lee, G.B.; Hwei, B.H.; Huang, G.R. *J. Micromech. Microeng.* **2001**, 11, 654-661.

92 Spešny, M.; Foret, F. *Electrophoresis* **2003**, 24, 3745-3747.

93 Fu, L.M.; Yang, R.J.; Lee, G.B. Pan, Y.J. *Electrophoresis* **2003**, 24, 3026-3032.

94 Pan, Y.J.; Lin, J.J.; Luo, W.J.; Yang, R.J. *Biosensors and Bioelectronics* **2006**, 21, 1644-1648.

95 Besselink, G.A.; Vulto, P.; Lammertink, R.G.H.; Schlautmann, S.; van den Berg, A.; Olthuis, W.; Engbers, G.H.M.; Schasfoort, R.B.M. *Electrophoresis* **2004**, 25, 3705-3711.

96 Kohlheyer, D.; Besselink, G.A.J.; Lammertink, R.G.H.; Schlautmann, S.; Unnikrishnan, S.; Schasfoort, R.B.M. *Microfluid Nanofluid* **2005**, 1, 242-248.

97 Hjertén, S.; Zhu, M. *J. Chromatogr.* **1985**, 346, 265.

98 Zhang, C.X.; Xiang, F.; Pasa-Tolic, L.; Anderson, G.A.; Veenstra, T.D.; Smith, R.D. *Anal. Chem.* **2000**, 72, 1462-1468.

99 Hofmann, O.; Che, D.P.; Cruickshank, K.A.; Muller, U.R. *Anal. Chem.* **1999**, 71, 678-686.

100 Mao, Q.L.; Pawliszyn, J. *J. Biochem. Biophys. Methods* **1999**, 39, 93-110.

101 Mao, Q.L.; Pawliszyn, J. *The Analyst* **1999**, 124, 637-641.

102 Cabrera, C.R.; Finlayson, B.; Yager, P. *Anal. Chem.* **2001**, 73, 658-666.

103 Fang, X.H.; Adams, M.; Pawliszyn, J. *The Analyst* **1999**, 124, 335-341.

104 Huang, T.; Pawliszyn, J. *Electrophoresis* **2002**, 23, 3504-3510.

105 Kato, M.; Inuzuka, K.; Saka-Kato, K.; Toyo'oka, T. *Anal. Chem.* **2005**, 77, 1813-1818.

106 Yu, C.; davey, M.H.; Svec, F.; Fréchet, J.M.J. *Anal. Chem.* **2001**, 73, 5088-5096.

107 Chen, Z.; Wang, P.; Chang, H.C. *Anal. Bioanal. Chem.* **2005**, 382, 817-824.

108 Koerner, T.; Turck, K.; Brown, L.; Oleschuk, R.D. *Anal. Chem.* **2004**, 76, 6456-6460.

109 Xie, S.; Svec, F.; Fréchet, J.M.J. *J. Polym. Sci. Part A: Polym. Chem.* **1997**, 35, 1013-1021.

110 Li, N.; Cho, A.S.; Broadbelt, L.J.; Hutchinson, R.A. *Macromol. Chem. Phys.* **2006**, 207, 1429-1438.

111 Wang, X.C.; Yang, X.H.; Zrang, X.M. *Analytical Sciences* **2006**, 22, 1099-1104.

112   Melander, C.; Momcilovic, D.; Nilsson, C.; Bengtsson, M.; Schagerlof, H.; Tjerneld, F.; Laurell, T.; Reimann, C.T.; Gorton, L. *Anal. Chem.* **2005**, 77, 3284-3291.

113   Reichmuth, D.S.; Shepodd, T.J.; Kirby, B.J. *Anal. Chem.* **2005**, 77, 2997-3000.

114   Morishima, K.; Bennett, B.D.; Dulay, M.T.; Quirino, J.P.; Zare, R.N. *J. Sep. Sci.* **2002**, 25, 1226-1230.

115   Breadmore, M.C.; Shrinivasan, S.; Wolfe, K.A.; Power, M.E.; Ferrance, J.P.; Hosticka, B.; Norris, P.M.; Landers, J.P. *Electrophoresis* **2002**, 23, 3487-3495.

116   Throckmorton, D.J.; Shepodd, T.J.; Singh, A.K. *Anal. Chem.* **2002**, 74, 784-789.

117   Yu, C.; Xu, M.; Svec, F.; Frechet, J.M.J. *J. Polym. Sci.: Part A: Polym. Chem.* **2002**, 40, 755-769.

118   Yang, Y.; Li, C.; Lee, K.H.; Craighead, H.G. *Electrophoresis* **2005**, 26, 3622-3630.

119   Yang, Y.; Li, C.; Kameoka, J.; Lee, K.H.; Craighead, H.G. *Lab on a Chip* **2005**, 5, 869-876.

120   Krenková, J.; Bilková, Z. *J. Sep. Sci.* **2005**, 28, 1675-1684.

121   Dulay, M.T.; Baca, Q.J.; Zare, R.N. *Anal. Chem.* **2005**, 77, 4604-4610.

122   Kato, M.; Inuzuka, K.; Sakai-Kato, K.; Toyo'oka, T. *Anal. Chem.* **2005**, 77, 1813-1878.

123   Kato, M.; Sakai-Kato, K.; Jin, H.; Kubota, K.; Miyano, H.; Toyo'oka, T.; Dulay, M.T.; Zare, R.N. *Anal. Chem.* **2004**, 76, 1896-1902.

124   Xie, S.; Svec, F.; Fréchet, J.M.J. *Biotechnology and Bioengineering* **1999**, 62, 30-35.

125   Peterson, D.S.; Rohr, T.; Svec, F.; Fréchet, J.M.J. *Anal. Chem.* **2002**, 74, 4081-4088.

2.1 Introduction

In this chapter, we demonstrate a protein fractionator and collector which is designed to be merged into a protein analysis system on a microchip. Considerable work on the application of microfluidic chips to proteomics has been reported [1,2]. However, a protein analysis platform on a microchip remains a challenging, yet very promising research area. This alternative to the traditional protein analysis method has the beauty of integrating individual analysis steps on a single chip. On a proteomics platform, given a complex mixture of proteins, the components first have to be separated, then fractionated and collected for further analysis [3]. Therefore, a protein fractionator and collector is an indispensable part of a protein platform. Müller *et al* [4] designed a fraction collector for capillary electrophoresis in which the sample exits the separation capillary and is forced toward a group of capillaries, which are located in the grooves of a cylinder. Khandurina *et al* [5] used a plastic cross-connector to couple the separation column and a single fraction collection capillary. Tulock *et al* [6] combined microfluidics with nanostructures and developed a nanofilm-based, gateable fraction collection system for mass-limited samples. Müller's device is bulky while only one collection channel is available on Khandurina's or Tulock's device. Our goal is to integrate a fractionator and collector onto a protein processing platform. Therefore, an "in-space" fractionator and collector with multiple collection channels is required.

Fractionation "in-time" has been shown in 2-d separation systems on chip [7], but much less work has been done to show fractionation "in-space" for protein samples. However, fractionation "in space" makes it possible to integrate protein separation with the following digestion, concentration and identification stages on a microchip.

Designing a fractionator and collector always involves controlling the flow from one dimension to the other, which is realized by either a valve or valveless system. Wang *et al.* [8] reported the isolation of an isoelectric focusing channel from a CE channel, using the air valve system which was first introduced by Quake *et al* [9]. Choi *et al.* [10] coupled isoelectric focusing with micro liquid chromatography in a demonstration employing conventional, rotor-based valves. Conventional rotor valves were also used by Yin *et al.* [11] for flow switching between sample loading and separation. However, a valve system is not an ideal solution for a proteomic chip platform, because of the complexity resulted from the peripheral hardware and the possibility of flow interruption during separation. In valveless systems, flow switching can be controlled by a pressure pump or electrokinetic force. Lee *et al.* [12] assembled a set of pressure pumps to adjust the sheath and sample flow rates in order to guide a focused sample stream into desired outlets. This kind of sheath effect arises from the laminar flow [13] in microchannels. Electrokinetic systems eliminate the disadvantages of the bulky pumps in pressure driven laminar flow. Moreover, electrokinetic flow switching [14] brings the advantage of being easier to operate. These advantages indicate the great potential of the application of electrokinetic force to a protein fractionator and collector.

In this chapter, we develop a fractionator and collector "in space" utilizing the principle of electrokinetic force. In our research work, we attempted to build up a protein analysis platform on a microchip. Our goal is to integrate protein separation, fractionation, digestion and preconcentration on a single microchip. Fractionation "in space" is an indispensable step for analysis of a complex sample. The essence of fractionation in space is to collect individual components into individual collectors

31

without cross contamination. Unfortunately, as is well known, leakage is a notorious problem in electrokinetic systems. Such leakage will lead to the contamination of the intersections of two orthogonal microchannels. In order to preclude this problem, we have taken advantage of electrokinetic sheath flow effects to deliver the sample stream under the protection of the sheath buffers. In this chapter, we present the design of successive generations of microchips for fractionation purposes. The chip design and the achievements of each generation are discussed.

2.2 Experimental

The chip was flushed with 0.1 M NaOH (BDH assured, Québec, Canada) for one hour, followed by rinsing with water for half an hour, before flushing with 20 mM ammonium bicarbonate (pH=8.0) (Sigma, Ontario, Canada). Fluorescein (Sigma, Ontario, Canada) was dissolved in 20 mM ammonium bicarbonate. The images were taken by CCD camera connected to an epifluorescent microscope. Electropherograms of fluorescent signals were recorded with a PMT. High voltages were provided by a power supply box with seven relays. Control programs were written with Labview software. pSpice simulation was performed by using OrCAD Capture 9.1 software (OrCAD Inc., San Jose, CA, USA).

Microchips were made in the Nanofab at the University of Alberta using a previously published chemical etching procedure [15]. The 0211 glass (Precision Glass and Optics, CA, USA) substrate was coated with 30 nm thick chrome and 150 nm thick Au. It was coated with HPR 504 photoresist (Arch Chem., Norwalk, CT, USA) (500 pm for 10 s then 4000 rpm for 40 s.) to give a 1.5 μm thick layer. The pattern on the photomask was transferred to the substrate under UV light (365 nm) for 4 s. The

substrate was then dipped into 354 developer (Shipley, Newton, MA, USA) for 25 seconds, followed by etching in gold etchant for 30 s before etching in chrome etchant for 15 s. Finally, the substrate was soaked into HF glass etchant ($HF:HNO_3:H_2O$, 20:14:66) for 400 s to 800 s to the desired depth.

2.3 Chip design

This chapter will discuss two generations of fractionators. The first generation contains the "squashed tree" design. In the second generation, three fractionators outlined below were designed in an effort to determine the preferred design.

2.3.1 Squashed tree fractionator (the first generation)

This first generation of fractionators was made from a single mask process, resulting in a single depth. The structure of the "squashed tree" fractionator is given in Figure 2.1. The detailed dimensions are summarized in Table 2.1. All the channels were etched into the bottom wafer, with access holes drilled in the top wafer. The two wafers were thermally bonded together. The design consists of a sample channel for the sample, connected to ten collection channels. Two sheath channels surround the sample channel flow as it enters into fractionation zone.

2.3.1.1 Microchip operation

All the reservoirs and channels were filled with buffer first, then reservoir **S** was emptied and loaded with dye solution. (See Fig. 2.1 to identify reservoirs). Reservoir **S**, **Sh1** and **Sh2** received high voltages, while one of the collection channels was held at ground, driving the sample into one of the collection channels by electroosmotic flow.

33
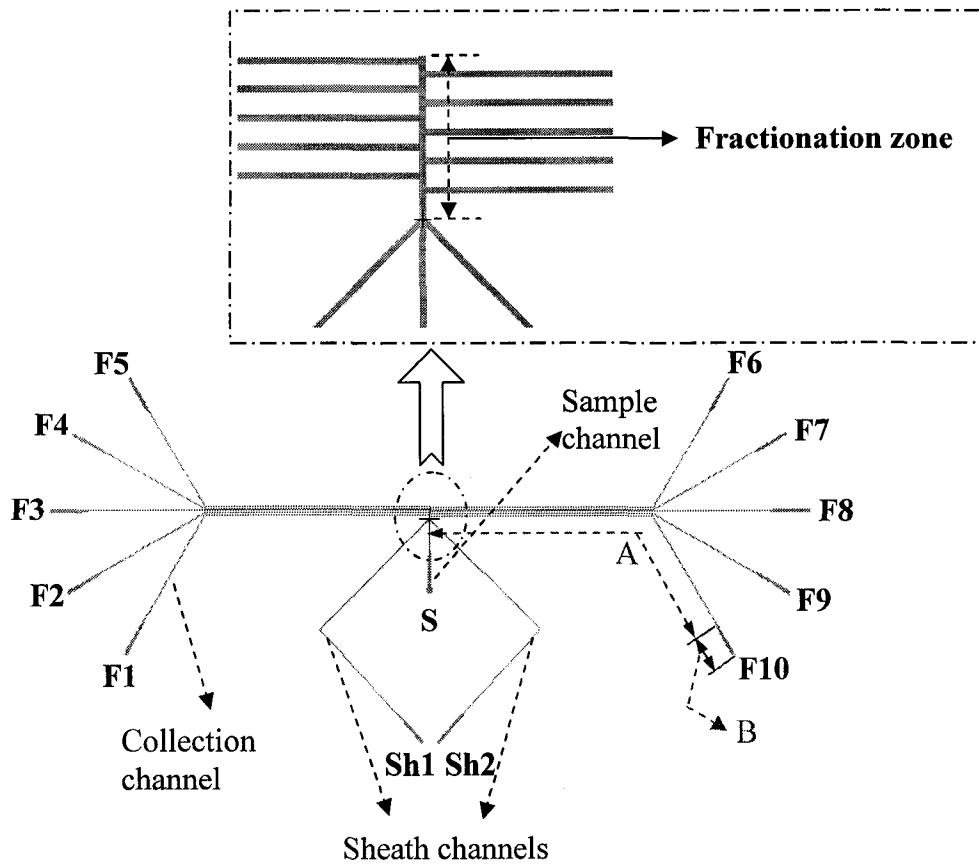
Figure 2.1 *The structure of the squashed tree design.* The distance between two adjacent collection channels is 100 μm center to center. The converging point of sample and sheath channels is called sheath point. All the channels are 10 μm deep and 70 μm wide.

Table 2.1 *Detailed dimensions of the squashed tree*

Fractionation zone	Sheath channel		Collection channel		Sample channel	
d =10 μm w =70 μm l =1100 μm	Segment A	d =10 μm w =70 μm l =24 mm	Segment A	d =10 μm w =70 μm l = 30 mm	Segment A	d =10 μm w =70 μm l = 3 mm
	Segment B	d = 10 μm w = 220 μm l = 3.4 mm	Segment B	d = 10 μm w = 220 μm l = 3.4 mm	Segment B	d = 10 μm w = 220 μm l = 3.4 mm

Note: Sheath, collection and sample channels all contain two segments, A and B, with different dimensions, as shown in Figure 2.1.

34

Flow from **Sh1** and **Sh2** into the collection channels was also driven by electroosmotic

force too. The sheath flows functioned as protective fluids which prevented the dye

stream from flowing into other floating channels. A sheath flow profile [16] like the one

shown in Figure 2.2 was formed on the chip.
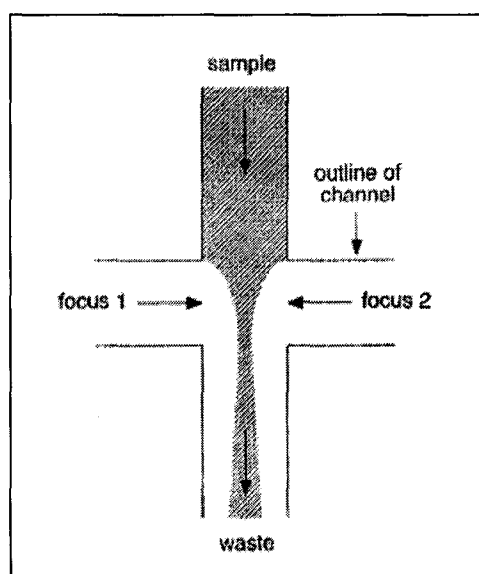
Figure 2.2 *Cartoon shows the sheath flow profile*
Adapted from J.M. Ramsey et al, Anal. Chem. 1997,
69, 3212-3217.

2.3.1.2 Impedance simulation

In order to predict the flow profile, pSpice software was used for simulations of the

device designs. The results instruct the choice of voltages used in the experiments. In

this simulation model, the channels are treated as resistors. Because all the channels are

filled with the same buffer, their relative impedance only depends on the dimensions.

When a voltage layout is set up, the simulation result gives the current (I) in each

35

channel and the voltage at each intersection point. The current is proportional to the volume flow rate (F) as follows:

$$I = \frac{V}{R} = \frac{El}{\rho l / A} = \frac{EA}{\rho} = \frac{v/\mu}{\rho} \times A = \frac{F}{\mu\rho} \quad , \qquad \mu = \mu_{eo} + \mu_{ep} \tag{1}$$

where R is resistance, E is electric field, l is the length of the channel, ρ is resistivity, A is the cross section area of the channel, v is the linear velocity, μ_{eo} and μ_{ep} are electroosmotic mobility and electrophoresis mobility, respectively. The diffusion distance (d) can be calculated from the voltage drop as follows:

$$d = \sqrt{2Dt} = \sqrt{2Dl_F / v} = \sqrt{\frac{2Dl}{\mu E}} = \sqrt{\frac{2Dl^2}{\mu V}} \tag{2}$$

where D (3.3 $\times 10^{-6}$ cm^2/s for fluorescein [17]) is diffusion coefficient, l_F is the length of the fractionation zone, and t is the traveling time along the fractionation zone. In our case, the sample velocity is usually smaller than the electroosmotic flow (EOF) of the sample streams, because the electrophoretic flow of sample is typically opposite to the EOF. Because the EOF is uniform in the fractionation zone, the flow velocities of the sample and sheath streams can be assumed to be the same. However, the net flow of sample in the sample stream will be different, since μ_{ep} is not zero. When considering the sheath effect, it is the volume flow rate of solvent, and thus EOF alone that matters. Thus, the difference between sample stream flow rate (F_{sample}) and sheath buffer flow rate ($F_{sheath\ stream}$) results in different cross sectional areas (A) of sample streams and sheath streams in the fractionation zone. The cross sectional area controls the stream width, since the channel depth in that zone is a constant. Therefore, stream width is only proportional to flow rate. The width of the sample stream is given by

36

$$W_{sample} = \frac{F_{sample}}{F_{sample} + F_{sheath\ buffer}} \times W_{fractionation\ zone} + 2d(t) \tag{3}$$

where W_{sample} and $W_{fractionation\ zone}$ are the width of the sample in the fractionation zone and the width of the fractionation zone, respectively. d is horizontal diffusion distance of the sample. This equation predicts a constant width due to volume flow rate ratios, and a time dependent term due to diffusion. To account for μ_{ep} being non-zero, the net mobility μ is used to determine the length of time the sample has to diffuse while it is in the fractionation zone.

The width of the sample stream is a key factor in our experiment. A wide sample stream may contact the inlets of other collection channels, therefore contaminating other channels. Too narrow a sample stream means that there will be too much dilution by the sheath buffers. Because the volume flow rate is determined by current flow, as shown in eq. 1, the important design factors are governed by the percent of current flow in the sample channel relative to the total current flow. To evaluate the flow rate ratios in eq. 3, only the relative impedance values need be obtained from the simulation. Consequently, the ratio of the channel length to the cross sectional area was used instead of the true impedance value. This value is equal to R/ρ (μm^{-1}) for each channel segment. The pSpice model of the channel segments considered provides the electric field and current flow in each segment. The electric field allows calculation of the migration times through each segment, from $v = l/t = \mu E$. The time in the fractionation zone, needed to calculate d (t) from eq. 2 is thus obtained from the model. The volumetric flow ratio is then calculated from the currents, predicted by the pSpice model. The overall mobility of fluorescein was measured and the diffusion coefficient of fluorescein was obtained

37

from previous work [17]. pSpice simulation model can not give as accurate a prediction as other simulation methods, such as finite element analysis, can provide, because only electrokinetic force is considered in pSpice simulation whereas hydrodynamic force is not considered. However, it gives enough information for an initial device layout design. This modeling method is not time-consuming, so it is an appropriate design tool for complex chip design. In comparison, if the finite element analysis method is used, it will take a very substantial amount of computer time (many days or weeks) to obtain the simulation results for a system as complex as ours.

2.3.1.3 Results and discussion

2.3.1.3.1 Measuring the mobility of fluorescein

To measure the mobility of fluorescein, a series of voltages were applied between reservoir S and **F10** (see Figure 2.1) to drive fluorescein past the detector (located at the sheath point), giving an electropherogram like that shown in Figure 2.3. The relative impedance of each portion of the system is shown in Figure 2.4.
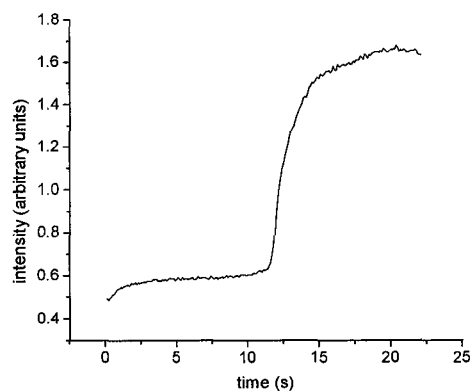
Figure 2.3 *The electropherogram collected when 800 V was applied between reservoir S and F10. A PMT detector was located at the sheath point described in Figure 2.1.*

38

The migration time is calculated by

$$t_{migr} = \frac{L}{v} = \frac{0.34cm}{\mu E_1} + \frac{0.3cm}{\mu E_2} = \frac{1}{\mu}\left(\frac{0.34cm^2}{V_1} + \frac{0.3cm^2}{2.897V_1}\right), \quad V_1 = 0.0294V$$

So,

$$\frac{1}{t_{migr}} = 0.2004\mu V.$$

Figure 2.5 shows the linear relationship between $1/t_{migr}$ and the voltage. The mobility was calculated to be $(4.34 \pm 0.10) \times 10^{-4}$ cm^2 V^{-1} S^{-1}, a value used in the following calculations. A value of $(1.21 \pm 0.06) \times 10^{-4}$ cm^2 V^{-1} S^{-1} was reported previously [17], in a different buffer system. However, the glass type was not described in this paper.
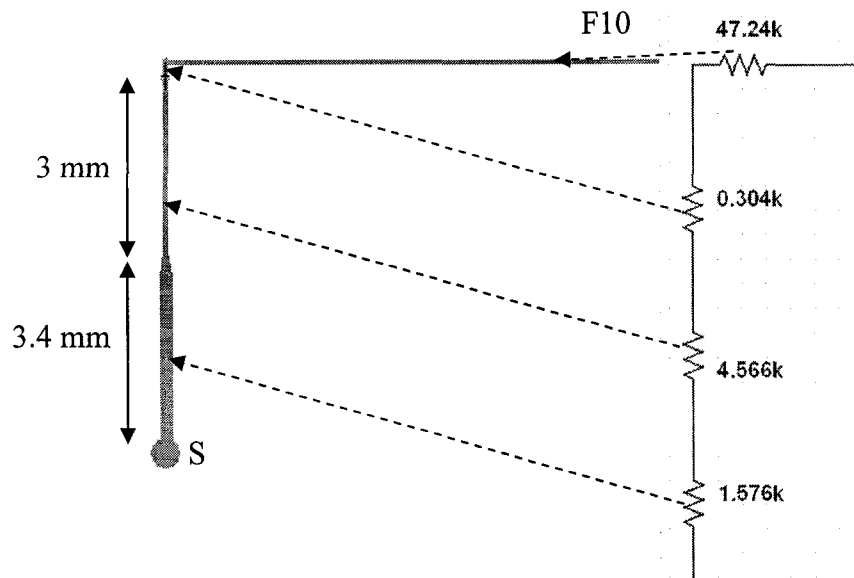
Figure 2.4 The structure of a portion of the squashed tree and the impedance of each segment expressed as R/ρ.

39
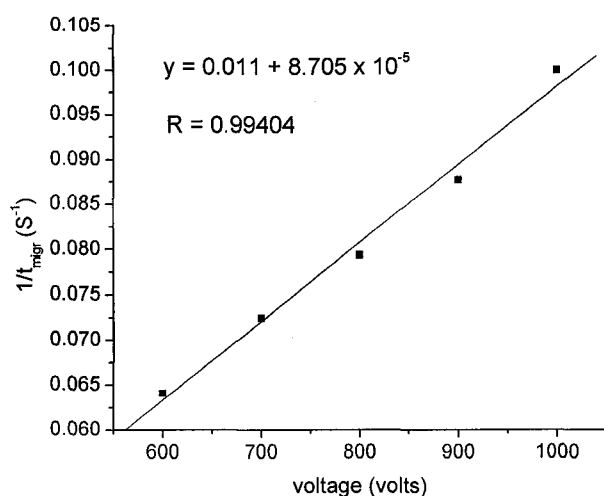
Figure 2.5 $1/t_{migr}$ varies as a function of voltage. Sample was loaded into reservoir S (Figure 2.4) and driven past the detector located at the sheath point.

2.3.1.3.2 Effect of pinching voltage on the sheath effect

Figure 2.6 demonstrates the necessity of using sheath flow to reduce leakage. In Figure 2.6, the furthest collection channel was grounded, and the two sheath arms were left floating. The sample stream spread everywhere as it passed by the inlets of other collection channels.
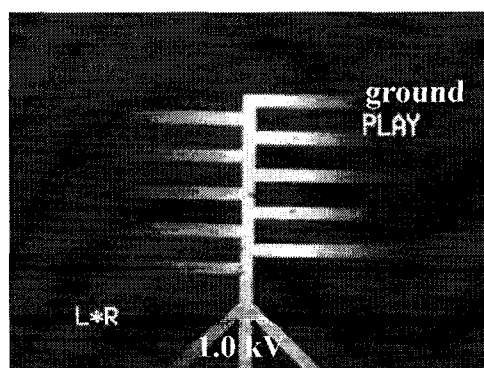
Figure 2.6 Flow profile of the dye stream in a squashed tree fractionator without protection from the sheath buffers. Reservoir S was at +1.0 kV and the last collection channel on the right side was at ground.

40
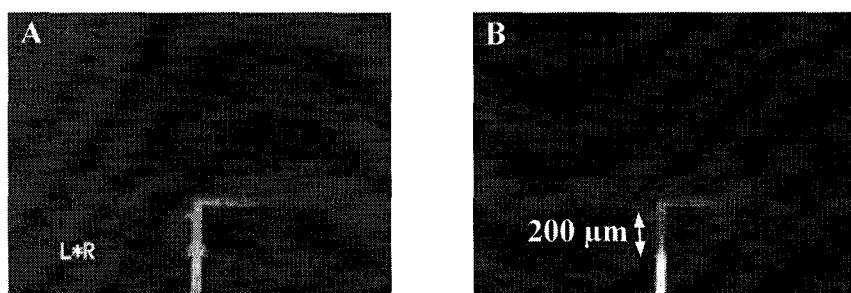
Figure 2.7 Images of sample streams show that the sample stream width changes with sheath voltage. Sample voltage was fixed at 1.0 kV while sheath voltage is 1.0k V for (A) and 1.2kV for(B), respectively.

The sheath effect at different sheath voltages was studied while the sample voltage (voltage applied to Reservoir S) was fixed at 1.0 kV. The results were shown in Figure 2.7, 2.8 and Table 2.2. Figure 2.7 A and B shows the results when using sheath flow at 1.0 kV and 1.2 kV, respectively. Figure 2.8 illustrates the simulation scheme used with pSpice software when sample and sheath voltages were 1.0 kV and 1.4 kV. Table 2.2 summarizes the data needed to calculate the sample stream width from pSpice simulation when the sample voltage was fixed at 1.0 kV, while the sheath voltages varied from 1.0 kV to 1.4 kV. Case **A** in Table 2.2 corresponds to Figure 2.7 A. The simulation tells us the stream will be close to 78 μm wide. Figure 2.7 A demonstrates that the sample stream filled the fractionation zone, which is 70 μm wide. Because of confinement by the channel wall, the sample stream can not spread to the predicted width. Figure 2.7 A also demonstrates no observable sheath effect was created, because the sample stream should be accompanied by the sheath streams on both sides if the sheath effect functions well. In Figure 2.7 B, the sample stream was only pinched

41

within a short region of several tens of micrometers before it expanded across the entire

fractionation zone. However, Case **B** in Table 2.2, the simulation for Figure 2.7 B,

indicates that the sample stream should spread to 49.6 μm, which is smaller than the

fractionation zone width, after transiting 300 μm in the fractionation zone. The

discrepancy might be related to flow resistance, which is not considered in the

simulation model. However, it is obvious that the sample stream gets thinner as the

focusing voltage increases. Further increase in the sheath voltage did not help much.

Our experiments showed that as the sheath voltage increased above a certain value the

sample stream could not be driven to the sheath point. The simulation results confirm

this, showing that the voltage at the sheath point becomes higher than that at the

Reservoir **S**, driving flow backwords. With 1000 V on **S**, this value is 1400 V on the

sheath channels according to the simulation (Figure 2.8).
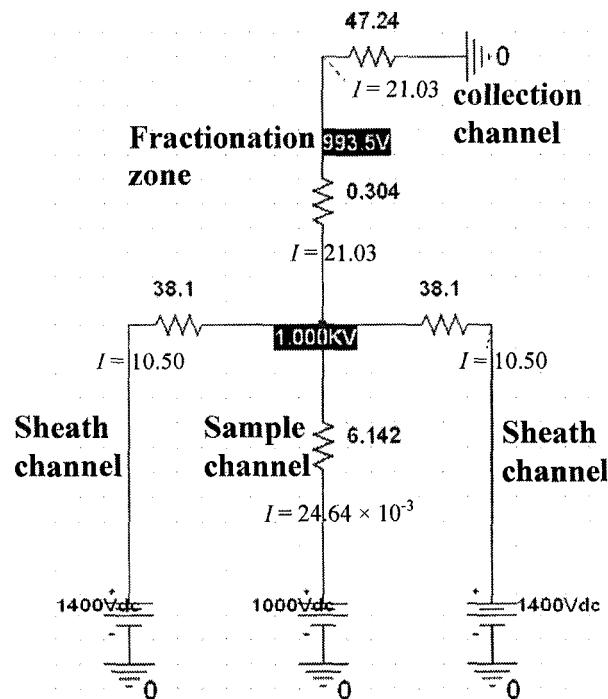
Figure 2.8 *Simulation scheme for the "squashed tree" fractionator.*
*Reservoir **S** was at 1.0 k V and reservoir **Sh1** and **Sh2** were at 1.4 k V. The first*
collection channel was at ground. The resistances are in 1000 · μm^{-1} and currents
are in V·μm /1000, respectively.

42

Table 2.2 *Simulation results for "squashed tree" fractionator at lower voltages*

	Case A	Case B	Case C
V_{sample} (V)	1000	1000	1000
V_{sheath} (V)	1000	1200	1400
$I_{sample\ channel}$ ($V \cdot \mu m /1000$)	14.45	7.21	$\cong 0$
$I_{fractionation\ zone}$ ($V \cdot \mu m /1000$)	19.11	20.04	
channel at ground	1st on the right	1st on the right	1st on the right
travel distance (μm)	300	300	
V_{drop} (V)	8.8	9.2	
$E_{fractionation\ zone}$ (V/cm)	293.3	306.7	
$t_{fractionation\ zone}$ (s)	0.236	0.225	
d (μm)	12.5	12.2	
W_{sample} (μm)	77.9	49.6	
$W_{sample}/ W_{fractionation\ zone}$	**1.1**	**0.71**	

V_{sample} and V_{sheath} are the voltages applied to reservoir **S** and reservoir **Sh1** and **Sh2**.

$I_{sample\ channel}$ and $I_{fractionation\ zone}$ are the current in sample channel and fractionation zone. *travel distance*, V_{drop}, and $E_{fractionation\ zone}$ are the length, voltage drop and electric field of part of the fractionation zone between the sheath point and the inlet of the collection channel at ground.

$t_{fractionation\ zone}$ and d are the transit time of sample stream and its diffusion distance in fractionation zone before it reaches the inlet of the collection channel at ground. W_{sample}, the width of the sample stream in fractionation zone.

$W_{sample}/ W_{fractionation\ zone}$, the ratio of the sample stream width to the total width of fractionation zone.

43

On the same "squashed tree" fractionator, using a higher sample voltage of 3.55 kV allowed a higher sheath voltage, giving a more neatly focused sample stream, as shown in Figure 2.9. In Figure 2.9 a, when the first collection channel on the left side was grounded, the sample stream looked good. However, when the first collection channel on the right side was grounded, the sample stream was introduced into this channel while at the same time it diffused forward. As a result, the 2nd channel on the left side was contaminated. However, with a higher voltage (Sample voltage: 5.07 kV, sheath voltage: 7.00 kV), as shown in Figure 2.9 b, the focused sample stream was longer, extending 700 µm before obvious diffusion broadening was observed. The simulation results are summarized in Table 2.3. As demonstrated in the simulation model and the images recorded, the sample stream became slightly wider as it traveled further and further downstream. The simulated ratio of sample width to the fractionation zone width is close to that demonstrated in the images. For example, when the 3rd channel on the left side was grounded, the observed sample stream was around 23 µm, while the predicted value was 16.89 µm. Given that the use of $\sqrt{2Dt}$ to estimate diffusion widths is a moderate approximation of the true error function distribution, the agreement is reasonable. Also, the switching time between channels contributes to broadening, as will be discussed in Chapter 4.

44
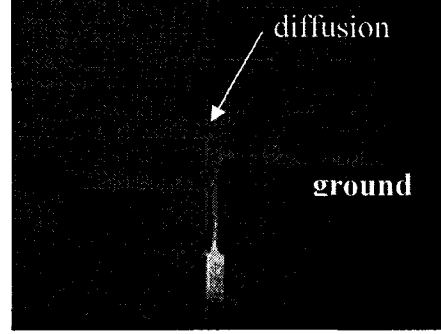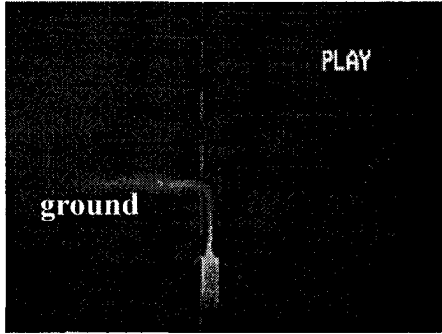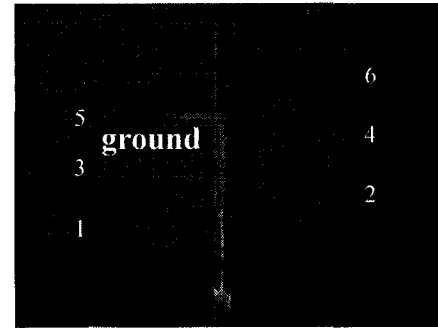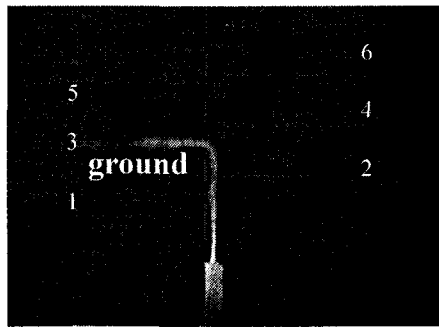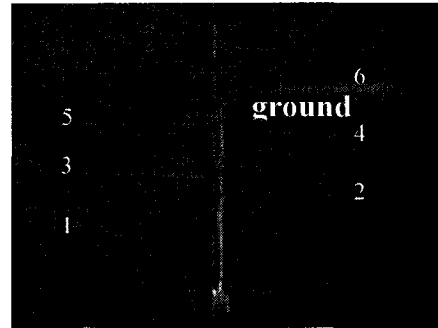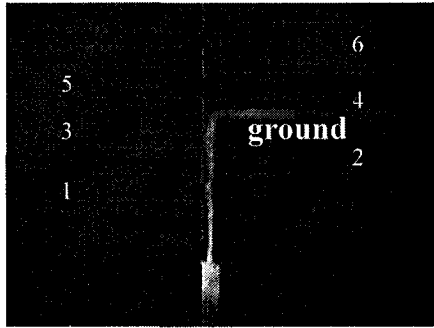
Figure 2.9 Sheath images for "squashed tree" fractionation. Figure 2.9 a:
Reservoir **S** at 2.66 kV, Reservoir **Sh1** and **Sh2** at 3.55 kV; *Figure 2.9 b:*
Reservoir **S** *at 5.07 kV,* *Reservoir* **Sh1** *and* **Sh2** *at 7.00 kV*

Table 2.3 Simulation results for "squashed tree" fractionator at higher voltages

	Case 1	Case 2	Case 3	Case 4	Case 5
V_{sample} (V)	2660	5070	5070	5070	5070
V_{sheath} (V)	3550	7000	7000	7000	7000
channel at ground	left 1st	left 2nd	right 2nd	left 3rd	right 3rd
$t_{fractionation\ zone}$ (s)	0.054	0.058	0.072	0.086	0.101
d (μm)	5.97	6.19	6.89	7.53	8.16
W_{sample} (μm)	20.01	14.50	15.76	16.89	18.00
$W_{sample}/$ $W_{fractionation\ zone}$	**0.28**	**0.21**	**0.22**	**0.24**	**0.26**

2.3.1.4 Summary of the squashed tree

The sheath effect was successfully demonstrated by the squashed tree design. However, in order to obtain an extended sheath effect, extremely high voltages were necessary, which are not desirable in many cases. Even with these voltages the sample stream remained confined for only around 700 μm, which limits the number of collection channels that can be incorporated to ~14 (assuming 50 μm wide channels with 100 μm from center to center).

2.3.2 The second generation

A second generation of chip with an improved design was developed. The results from the first generation showed that a high ratio of sheath to sample flow and shorter transit time of the sample stream were needed. We improved the design in several aspects.

46

1. In the first generation, most of the voltage drop occurs across the collection channels, so high voltages are needed in order to create a high electric field in the fractionation zone. Therefore, the electrical resistance of the collection channels should be reduced relative to the fractionation zone. In the second generation, the collection channels are deeper than all the other channels, which gives a smaller resistance and lower voltage drop. It is then possible to get a very high velocity and shorter transit time in the fractionation zone at lower applied voltages, thus reducing diffusion.

2. The fractionation zone in the first generation is so narrow that the sample stream is close to the collection channels. Therefore, the fractionation zone should be wider. However, too wide a fractionation zone will lead to significant longitudinal diffusion as the sample is directed towards the collection channels. If the fractionation zone is 1 mm wide, the center of the sample stream will be around 500 μm away from collection channel inlets. For an electric field in the fractionation zone of 1000 V/cm, a sample stream needs to travel ~500 μm before it reaches the inlets. These conditions lead to 9 μm of longitudinal diffusion spreading on both sides of the sample stream before it reaches the collection channel. Optimization of the fractionation zone width is thus an important parameter.

3. The short sample channel in the first generation design induces large current flow from the sample channel. Therefore, a longer sample channel with higher impedance and smaller current is needed.

47
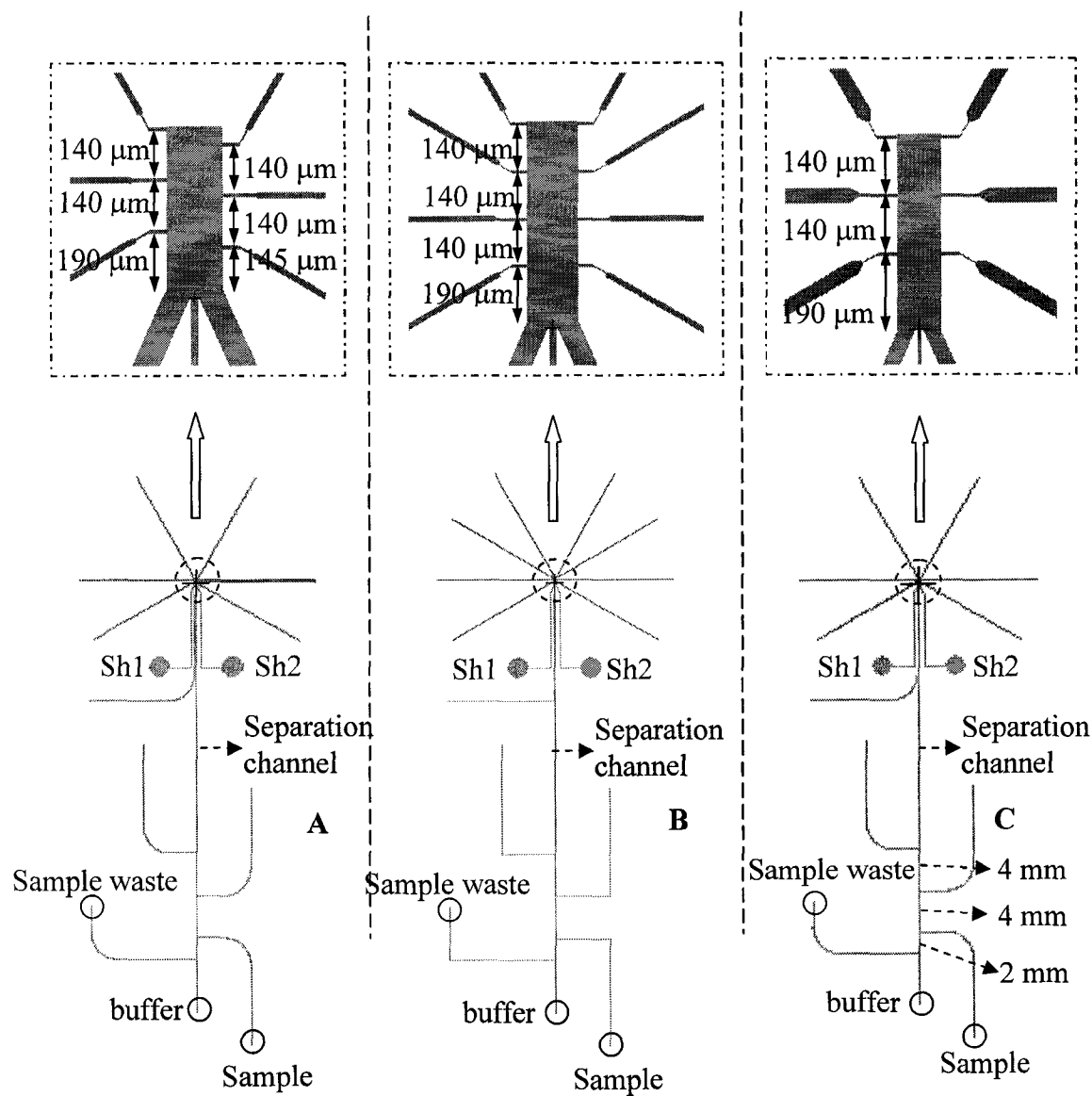
Figure 2.10 *Layouts of fractionators for the second generation. All the designs contain a separation channel, two sheath channels, five injection arms and a few collection channels. The dimensions are summarized in Table 2.4. The five arms located beside the separation channel will be used as injection arms in Chapter 6. They are all 10 µm deep and 70 µm wide. The injection arms in Design B are 15 mm long and those in Design A and C have similar lengths.*

48

4. All channels have the same width in the first generation. However, wider sheath channels with a smaller impedance should allow a larger current flow, which makes the ratio of sample flow to the total flow become smaller, improving the sheath effect, as predicted by eq.3. Thus, the sheath channels in the second generation are wider.

Table 2.4   Dimensions of Design A, B and C on the mask

	Fractionation zone	Sheath channel	Collection channel		Sample channel
A	$w = 162 \ \mu m$ $l = 500 \ \mu m$	$w = 78 \ \mu m$ $l = 10 \ mm$	Segment A	Segment B	$w = 20 \ \mu m$ $l = 40 \ mm$
			$w = 10 \ \mu m$ $l = 100 \ \mu m$	$w = 16 \ \mu m$ $l = 10 \ mm$	
B	$w = 162 \ \mu m$ $l = 650 \ \mu m$	$w = 78 \ \mu m$ $l = 10 \ mm$	Segment A	Segment B	$w = 20 \ \mu m$ $l = 40 \ mm$
			$w = 10 \ \mu m$ $l = 100 \ \mu m$	$w = 16 \ \mu m$ $l = 10 \ mm$	
C	$w = 114 \ \mu m$ $l = 500 \ \mu m$	$w = 46 \ \mu m$ $l = 10 \ mm$	Segment A	Segment B	$w = 10 \ \mu m$ $l = 40 \ mm$
			$w = 10 \ \mu m$ $l = 100 \ \mu m$	$w = 50 \ \mu m$ $l = 10 \ mm$	

Note: The collection channels contain two segments with different dimensions, as suggested in Figure 2.10.

Three fractionators (Figure 2.10) with different dimensions (Table 2.4) were designed to realize fractionation at a lower voltage combination. Design A and B are only different in the number of collection channels and length of the fractionation zone. On one hand, simulation shows that, due to the wider collection channel and narrower

49

fractionation zone, the sample stream in Design **C** will be narrower than that of **A** or **B** for the same voltage combination. On the other hand, the narrower fractionation zone makes the sample stream closer to inlets of collection channels, which may be preferable according to point 2 above.

A two-mask process was used to produce channels with different depths, allowing better focusing of the applied fields. All the collection channels are deeper than the other channels to reduce the voltage drop there. Each design has two sheath channels and six to eight collection channels. There are five arms located on both sides of the sample channel. These arms are used to define injection plugs with different lengths, resulting in different amounts of sample being introduced.

2.3.2.1 Fabrication details

Mask **A** contains all the channel patterns except the pattern of the collection channels while Mask **B** contains only the collection channels. The microchips were made in two ways.

Method A

Mask A development used exactly the protocols described in the experimental section. The channels were etched to 10 μm in depth. After stripping off the metal films, the substrate was coated again with Cr film (30 nm) and gold film (150 nm). In the lithography process, the patterns on **Mask B** were transferred to the substrate, followed by etching the collection channels to 30 μm in depth. The image of the chip is shown in Figure 2.11. It can be seen that the edges of the fractionation zone are not clearly defined. The edges of the fractionation zone were etched again during the etching process of the collection channels. This might be explained by three factors. First, the

50

Cr and Au films are not thick enough to properly cover the edges of the fractionation zone. Second, one layer of HPR 504 photoresist may not properly cover the edges of the channels. As shown in Figure 2.12, after the spinning of one layer of photoresist, some streaks could be seen. Because there were already some channel patterns etched on the chip, the spreading of the photoresist would be restricted around the channel regions, especially at the edges and corners of the channels. Supporting these concerns, the gold film inside the channels can be seen close to the edges. Some visible streaks around the channels indicate that the covering of the photoresist in those regions is not uniform. Finally, the HF etching process may be a cause, since it took 20 minutes to etch the collection channels to the desired depth. The long soaking in HF can lead to metal film adhesion failure, causing etch defects.
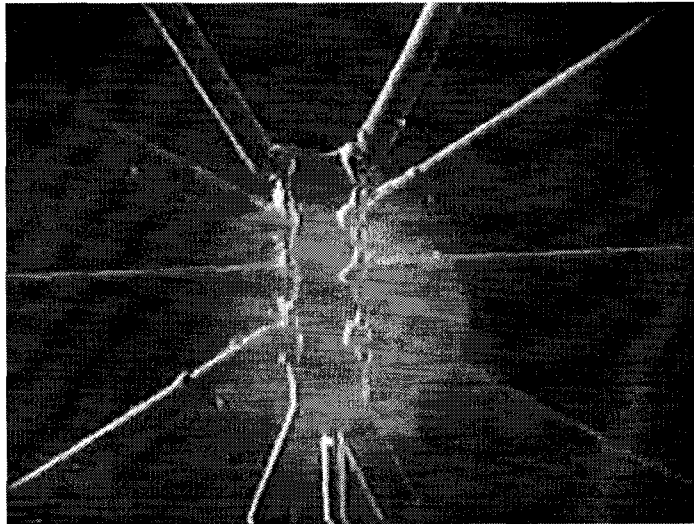
Figure 2.11 Image of the chip made via *Method A* shows the bad inlets regions
The collection channels are 30 μm deep and all the other channels are 10μm
deep.

51

Method B

Mask **B** was used first to etch the collection channels to 20 μm in depth. Afterwards, the metal films were stripped off and a new metal film was deposited again. The thickness of the Cr and Au film was increased to 60 nm and 250 nm, respectively. During the lithography process, the substrate was first covered with one layer of HPR 504 photoresist, followed by hard baking at 115°C for half an hour. The speed of spread and spin was adjusted to be 500 rpm and 1000 rpm, respectively. This process was repeated twice, until the substrate was covered with three layers of photoresist with a thickness of around 6.0 μm. As shown in Figure 2.12 C, no yellow color or streaks appeared on the substrate with three layers of photoresist. Afterwards, the substrate was
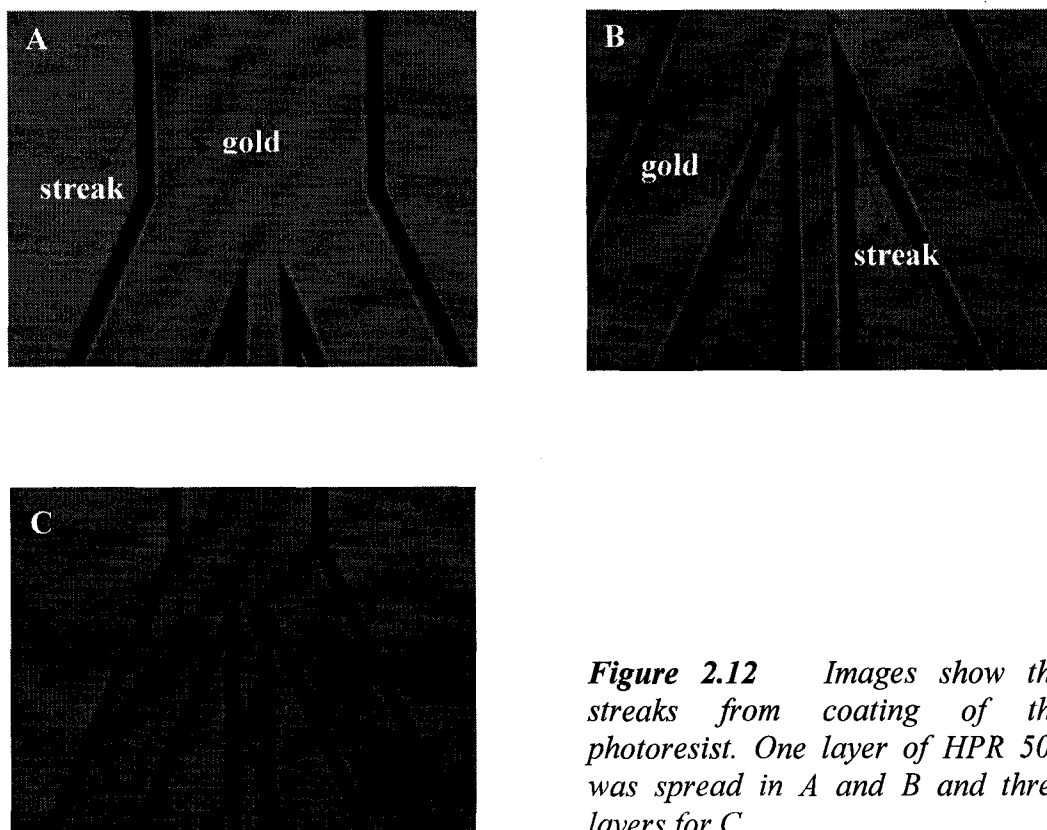
Figure 2.12   Images show the streaks from coating of the photoresist. One layer of HPR 504 was spread in A and B and three layers for C.

52

aligned with Mask **A** accurately before exposue. Because the photoresist is thicker, the exposure time was extended to 20 s and the development process took 45 s, compared to 25 s for the normal protocol. Due to the thicker metal films, 60 s was spent on Au etching and 40 s on Cr etching. Finally, the fractionation zone and other channels were etched to 5 μm in depth. Images of the chips are shown in Figure 2.13. The edges of all the channels are nicely defined.
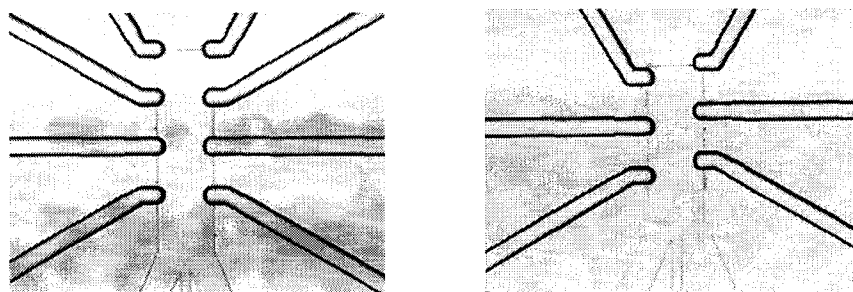
Figure 2.13 Images of the chips made via **Path B** show well defined edges in inlets regions. The collection channels are 20 μm deep and all the other channels are 5 μm deep.

2.3.2.2 Study on sheath effect for designs made via Method B

Devices made by **Method A** behaved poorly due to etch defects. For the fractionator devices made via **Method B**, the sheath flow effects were tested for a series of voltage combinations. For Design **C**, it was found that 700 V on the sample reservoir and 2200 V on the sheath reservoirs gave a nicely pinched sample stream, as shown in Figure 2.14. The simulation results are shown in Figure 2.15 and Table 2.5 for the three different collection channels. The experiments performed at other voltage combinations gave wider sample streams, as shown in Figure 2.16. The simulation results are shown in Table 2.6. As can be seen from Figure 2.16A and B, a higher negative voltage on the

53

collection channel (Figure 2.16A) produced a more narrow sample stream in the fractionation zone. Because of this, the diffusion distance was smaller, which resulted in a thinner dye stream. This is in agreement with the results in Table 2.6. Figure 2.16 C, D, E and F illustrated that lower sheath voltages made the sample stream a little bit wider, when the voltages applied to the sample reservoir and sheath reservoirs were fixed.
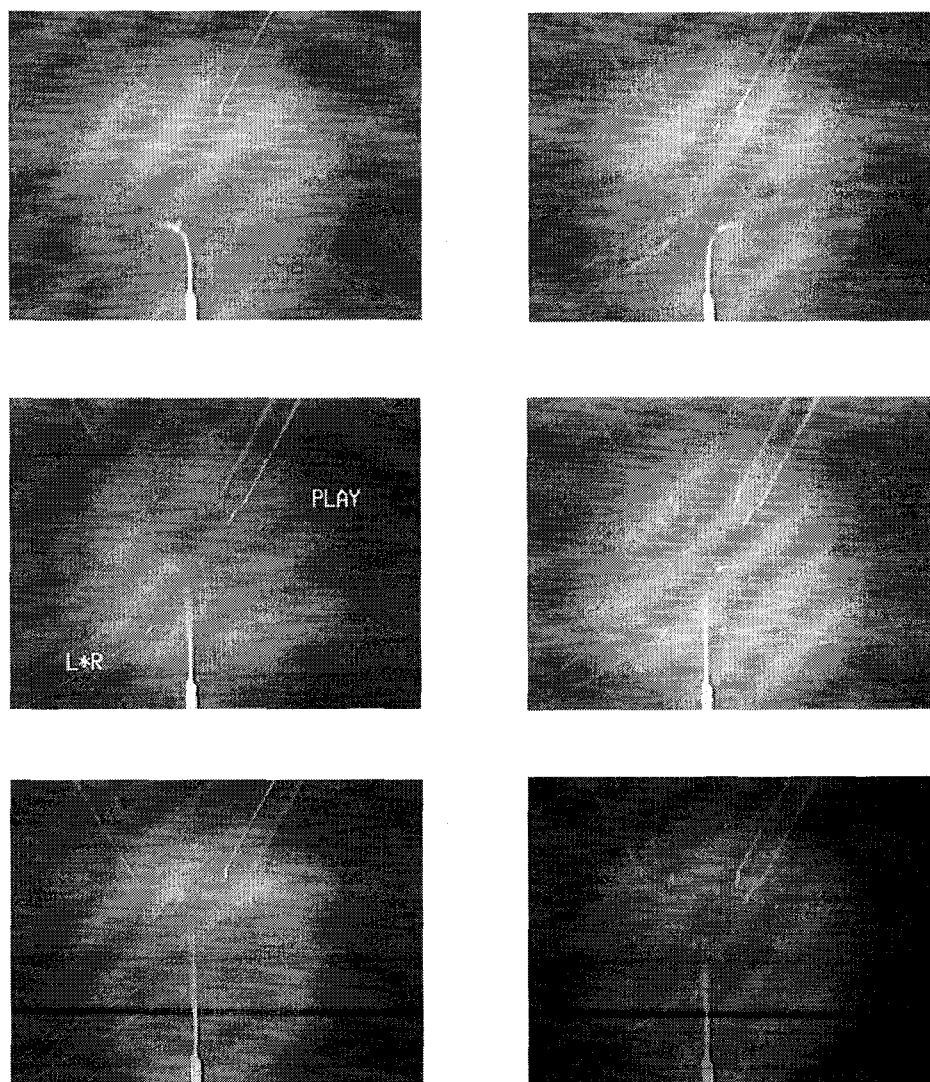
Figure 2.14 Images show the sequential fractionation of flow into each collection channel in **Design C.** Sample voltage: 0.7 kV, sheath voltage: 2.2kV

54

6.263
—\/\/\—

538.1V

0.804

$I = 85.91$

37.17   607.1V   37.17

$I = 42.85$ $I = 42.85$

449.44

$I = 206.6 \times 10^{-3}$

2200Vdc   700Vdc   2200Vdc

0   0   0
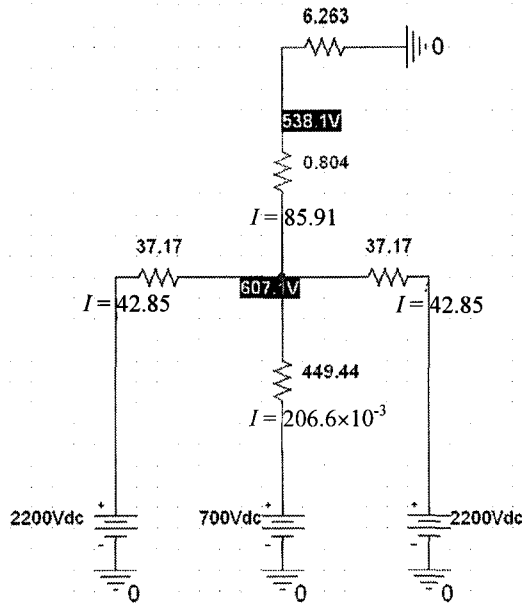
Figure 2.15 *Simulation result of the case when the third collection channel was at ground for Design C. The units of resistances and currents are the same as those in Figure 2.8.*

Table 2.5 *Simulation results for Design C when three collection channels were grounded separately*

	Case 1	Case 2	Case 3
V_{sample} (V)	700	700	700
V_{sheath} (V)	2200	2200	2200
channel at ground	1st	2nd	3rd
$t_{fractionation\,zone}$ (s)	0.030	0.055	0.080
d (μm)	4.45	6.02	7.27
W_{sample} (μm)	9.29	12.38	14.83
$W_{sample}/W_{fractionation\,zone}$	**0.07**	**0.10**	**0.12**

55
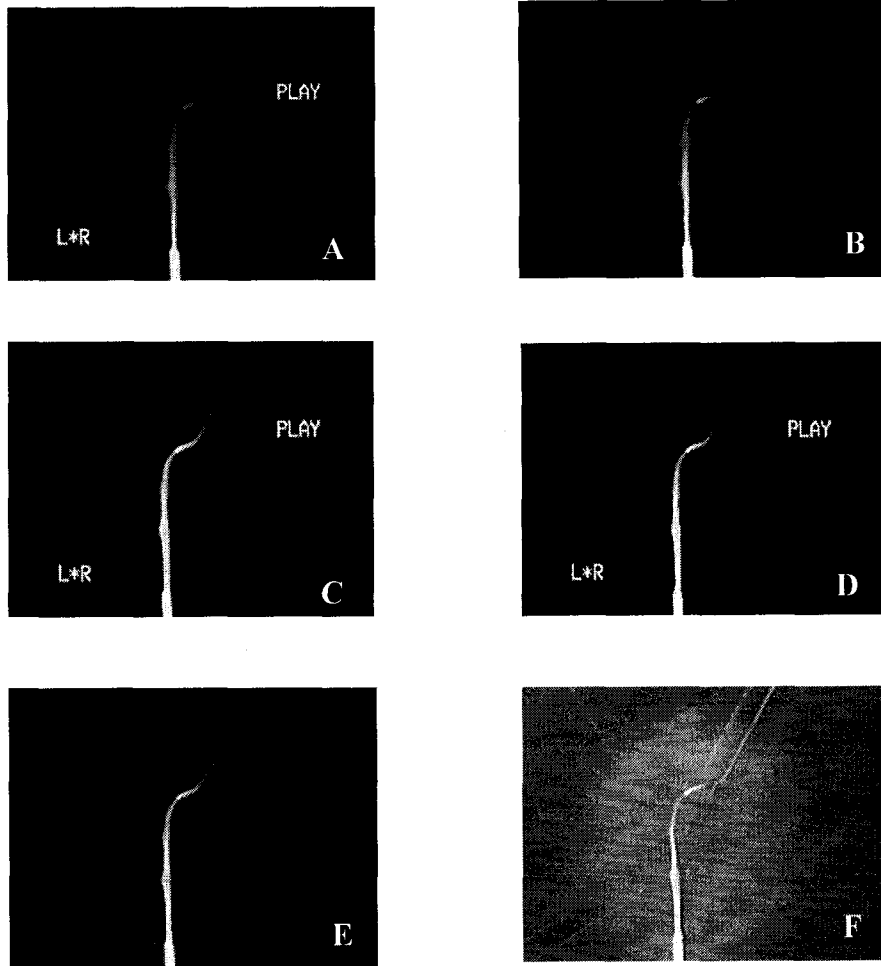
Figure 2.16 *Images for Design C at different voltage combinations*

when the third channel on the right side was grounded

(A) collection -1.0 kV, sheath 0.7 kV; (B) collection -0.5 kV, sheath 0.7 kV
(C) collection -4.0 kV, sheath 0.5 kV; (D) collection -4.0 kV, sheath 1.0 kV
(E) collection -4.0 kV, sheath 1.5 kV; (F) collection -4.0 kV, sheath 2.0 kV

56

Table 2.6 *Simulation results for Design C when the 3ʳᵈ channel was grounded*

	A	B	C	D	E	F
V_{sample} (V)	0	0	0	0	0	0
$V_{fractionation}$ (V)*	-1.0	-0.5	-4.0	-4.0	-4.0	-4.0
V_{sheath} (V)	0.7	0.7	0.5	1.0	1.5	2.0
travel distance (μm)	490	490	490	490	490	490
$I_{sample\ channel}$ ($V \cdot \mu m /1000$)	1.170	0.3727	6.072	5.769	5.466	5.163
$I_{fractionation\ zone}$ ($V \cdot \mu m /1000$)	67.12	47.05	179.8	199.1	218.4	237.6
V_{drop} (V)	53.9	37.8	145	160	175	191
$E_{fractionation\ zone}$ (V/cm)	1100	771	2959	3265	3571	3898
$t_{fractionation\ zone}$ (s)	0.103	0.146	0.038	0.034	0.032	0.029
d (μm)	8.24	9.82	5.01	4.74	4.60	4.37
W_{sample} (μm)	18.64	20.62	14.21	13.07	12.30	11.43

$V_{collection}$ is the voltage applied to the collection channel. A negative voltage was applied instead of at ground.

Design **A** and **B** are basically the same except the collection channels have different lengths. Here, we discuss the results of Design **B**. For Design **B**, the sheath effects were studied at low and high voltage combinations. They are shown in Figure 2.17 and Figure 2.18. The simulation results are summarized in Figure 2.19 and Table 2.7. When the sample stream transits 640 μm to the end of the fractionator, it spreads to about 17 μm in Figure 2.18 which is thinner than that (~25 μm) in Figure 2.17 because

57

of the higher voltage combination in Figure 2.18 compared to that in Figure 2.17. The predicted sample widths as shown in Table 2.7 will be 22.38 μm and 13.79 μm, respectively. However, the electric field in the fractionation zone was already over 2500 V/cm. Such high electric fields always induce bubbles in our experiment, while bubbles usually do not occur for electric fields less than 1000 V/cm. Moreover, the focused sample stream in Figure 2.17 is already thin enough not to touch the inlets of collection channels. Therefore, we ended up using lower voltages.

At the same voltages, the sample stream in Design **C** will be slightly thinner than that in Design **A** or **B** when comparing Case **A** in Table 2.6 and Case **C** in Table 2.7. However, on the other hand, the fractionation zone of Design **C** is narrower than the other two designs. Since the experiments showed that the sample stream in Design **A** or **B** was narrow enough not to touch the inlets of collection channels, no further experiments were performed in Design **C**.

Our experiments showed a drawback associated with the long and narrow sample channel. As seen from Figures 2.15, 2.19 and Tables 2.7 and 2.8, the voltage across the segment from the sample reservoir to the sheath point is so small that the electric field is only several tens of volts per centimeter. Such a weak electric field is not good for separation, because it results in low flow rate and long transit times, so that diffusion becomes a dominant term in peak broadening and resolution is ruined. The shorter sample channel will be discussed in Chapter 6 where it is referred to as the "separation channel".

2.3.3 Conclusion

In this chapter, two generations of fractionators were discussed. In the 1st generation, a tightly focused sample stream was created at quite high voltages (5-7 kV). In order to produce a nicely focused sample stream at lower voltages, the fractionator design was improved based on the information from the 1st generation. Deeper collection channels in the 2nd generation make it possible to create high electric field in fractionation zone and thus shorter transit time and less diffusion. Narrower and longer sample channel and wider sheath channels makes the first term in eq. 3 smaller, which helps to reduce sample stream width. Wider fractionation zone allows more space between sample stream and inlets of collection channels.
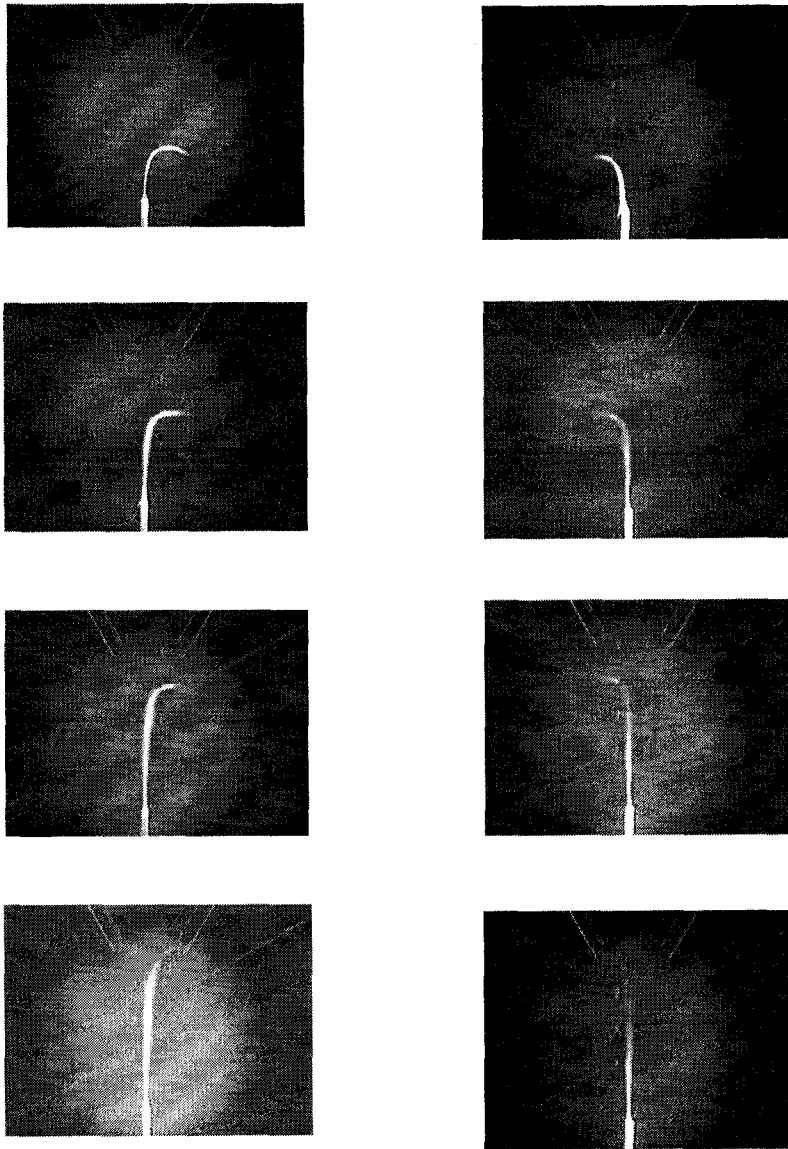
Figure 2.17 Images show the sequential fractionation of flow into each collection channel. Sample channel, sheath channel and collection channel were at ground, 700 V, and -1000 V, respectively.

60
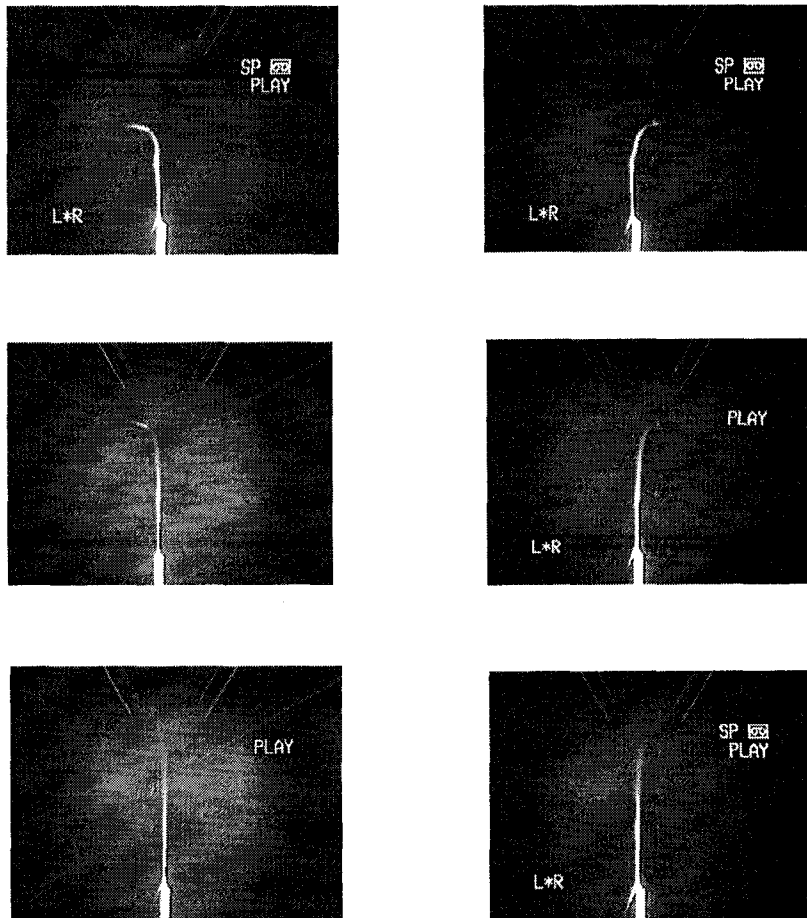
Figure 2.18 *Images show the sequential fractionation of flow into each collection channel. Sample channel, sheath channel and collection channel were at ground, 2000 V and -3000 V, respectively.*
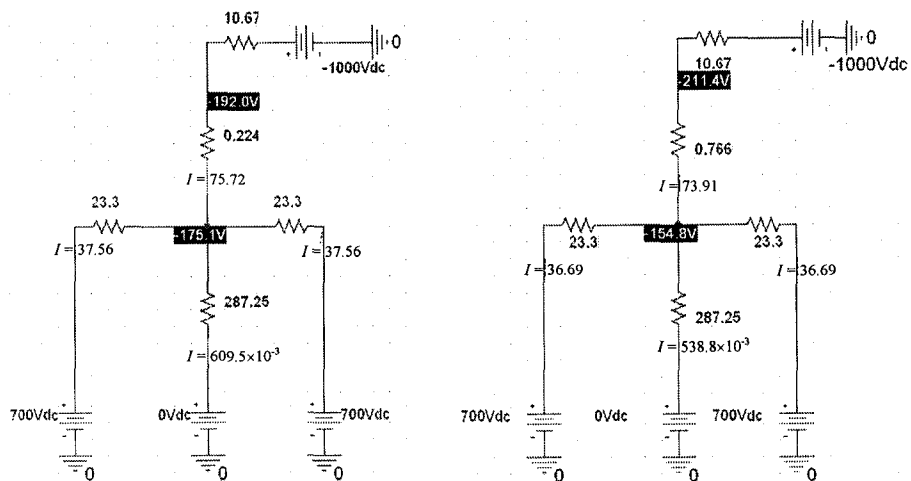
Figure 2.19 *Simulation results for Design **B** when the 1ˢᵗ and last collection channel was grounded. The units of resistances and currents are the same as those in Figure 2.8.*

61

*Table 2.7 Simulation results for Design **B** at different voltages*

	A	B	C	D	E	F	G
V_{sample} (V)	0	0	0	0	0	0	0
$V_{fractionation}$ (V)*	-1000	-1000	-1000	-1000	-3000	-3000	-3000
V_{sheath} (V)	700	700	700	700	2000	2000	2000
channel at ground	1	2	3	4	2	3	4
travel distance (μm)	190	340	490	640	340	490	640
$I_{sample\ channel}$ ($V \cdot \mu m / 1000$)	0.6095	0.5862	0.5631	0.5403	1.925	1.857	1.790
$I_{fractionation\ zone}$ ($V \cdot \mu m / 1000$)	75.72	75.13	74.53	73.95	221.1	219.3	217.6
V_{drop} (V)	16.9	30	43	55.8	88.4	126.5	164
$E_{fractionation\ zone}$ (V/cm)	889	882	878	872	2600	2582	2562
$t_{fractionation\ zone}$ (s)	0.049	0.089	0.128	0.169	0.030	0.044	0.058
d (μm)	5.69	6.21	9.19	10.56	4.45	5.39	6.19
W_{sample} (μm)	12.76	13.76	19.68	22.38	10.40	12.24	13.79
$W_{sample}/ W_{fractionation\ zone}$	**0.07**	**0.08**	**0.11**	**0.13**	**0.06**	**0.07**	**0.08**

2.4 Reference

1. Wang, C.; Oleschuk, R.; Ouchen, F.; Li, J. J.; Thibault, P.; Harrison, D.J. *Rapid Commun. Mass Spectrom.* **2000**, 14, 1377-1383.

2. Wheeler, A. R.; Moon, H.; Bird, C. A.; Loo, R. R. O.; Kim, C. J.; Loo, J. A.; Garrell, R. L. *Anal. Chem.* **2005**, 77, 534-540.

3. Figeys, D.; Pinto, D. *Electrophoresis* **2001**, 22, 208-216.

4. Müller, O.; Foret, F.; Karger, B. L. *Anal. Chem.* **1995**, 17, 2974-2980.

5. Khandurina, J.; Guttman, A. *J. Chromatogr. A* **2002**, 979, 105-113.

6. Tulock, J. J.; Shannon, M. A.; Bohn, P. W.; Sweedler, J. V. *Anal. Chem.* **2004**, 76, 6419-6425.

7. Gottschlich, N.; Jacobson, S. C.; Culbertson, C. T.; Ramsey, J. M. *Anal. Chem.* **2001**, 73, 2669-267.

8. Wang, Y. C.; Choi, M. H.; Han, J. *Anal. Chem.* **2004**, 76, 4426-4431.

9. Unger, M. A.; Chou, H. P.; Thorsen, T.; Scherer, A.; Quake, S. R. *Science*, **2000**, 288, 113-116.

10. Choi, M. H.; Wang, Y. C.; Wishnok, J. S.; Tannenbaum, S. R.; Han, J. *MicroTAS Proceedings* **2004**, 255-257.

11. Yin, H. F.; Killen, K.; Brennen, R.; Sobek, D.; Werlich, M.; Goor, T. *Anal. Chem.* **2005**, 77, 527-533.

12. Lee, G. B.; Hwei, B. H.; Huang, G. R. *J. Micromech. Microeng.* **2001**, 11, 654-661.

13. Brody, J. P; Yager, P.; Goldstein, R. E.; Austin, R. H. *Biophys. J.* **1996**, 71, 3430-3441.

14. Johann, R.; Renaud, P. *Electrophoresis*, **2004**, 25, 3720-3729.

15. Fan, Z.H.; Harrison, D.J. *Anal. Chem.* **1994**, 66, 177-184.

16. Jacobson, S.C.; Ramsey J.M. *Anal. Chem.***1997**, 69, 3212-3217.

17. Harrison D.J; Manz A.; Fan Z.H. *Anal. Chem.* **1992**, 64, 1926-1932.

3.1 Introduction

Our aim is to fractionate and collect separated protein components utilizing a fractionator described in Chapter 2. The fraction collection in-space concept on microchip derives from conventional fraction collection with HPLC systems. Commercial HPLC instruments are usually endowed with two types of fraction collection functions. One approach is to collect the fractions into a series of vials at fixed time intervals as the fractions are eluted. The other approach is to collect an isolated peak for further identification. We are working to transfer these two methods to a microchip. Instead of a series of vials used as fraction container, we used a series of collection channels. In this chapter, we describe the peak selection method, evaluating fixed interval collection in a later chapter.

3.2 Combo Chip design

In order to test the fractionation efficiency of the fractionators discussed in Chapter 2, a more complex one containing CE separation channels downstream was designed. The CE stage was added to allow evaluation of the isolated fraction purity. The layout and dimensions of this so-called combo chip are shown in Figure 3.1 and Table 3.1. Reservoir C is loaded with sample and reservoir D is the sample waste. Separation buffer is loaded into reservoir A. B1 and B2 are reservoirs for the sheath buffers. E1 and E2 are the fraction collection reservoirs. F1 and F2 are sample waste. G1, G2, H1 and H2 are filled with separation buffer. The channels downstream (as shown in the expanded region) were used to evaluate the purity of the fractionated protein. The running buffer is 20 mM ammonium bicarbonate in water.

64
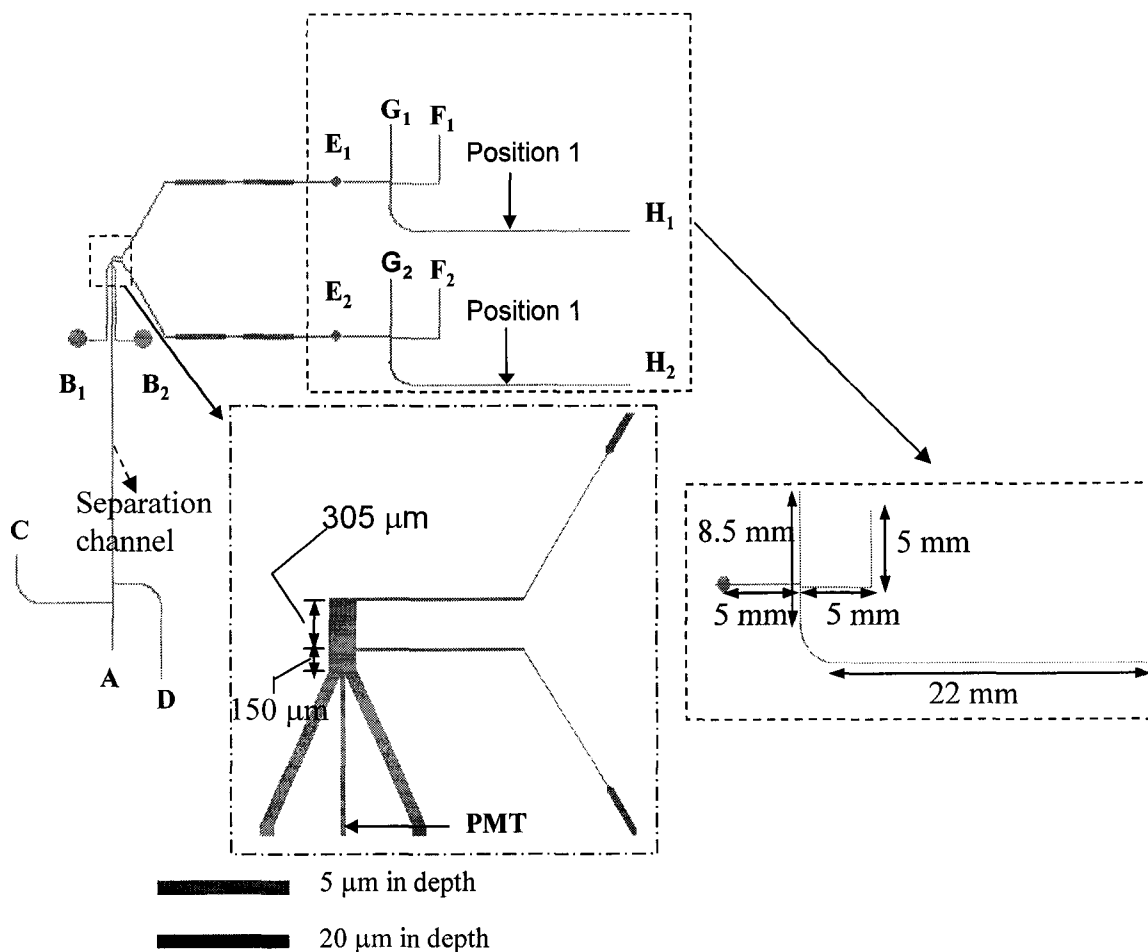
Figure 3.1 The sketch shows the fractionation/ CE device, with two fractionation channels. B1 and B2 are sheath reservoirs. Reservoirs C, D are used for sample injection, with CE performed downstream towards B by grounding Reservoir A. Reservoirs B and E received 1000 V and -2600 V to provide the sheath flow stream and the fractionation. On the right side expansions are shown of the following CE separation stages. Voltages of ~1000 – 3000 V were applied to each stage as required.

65

Table 3.1 *Dimensions of the Combo design*

Fractionation zone	$w = 162\ \mu m$, $l = 450\ \mu m$	
Sheath channel	$w = 78\ \mu m$, $l = 10\ mm$	
Separation channel	$w = 20\ \mu m$, $l = 40\ mm$	
Injection arm	$w = 20\ \mu m$, $l = 19\ mm$	
Collection channel	**1**, $w = 10\ \mu m$, $l = 2000\ \mu m$	**5**, $w = 10\ \mu m$, $l = 800\ \mu m$
	2, $w = 50\ \mu m$, $l = 8000\ \mu m$	**6**, $w = 50 \mu m$, $l = 3090\ \mu m$
	3, $w = 10\ \mu m$, $l = 800\ \mu m$	**7**, $w = 400\ \mu m$, $l = 10400\ \mu m$
	4, $w = 10\ \mu m$, $l = 1800\ \mu m$	
CE channels	$w = 50\ \mu m$	
	The length of each segment is shown in Figure 3.1.	

3.3 Sheath flow test

Detailed dimensions of the combo design are given in Table 3.1. The two collection channels are the same, and each of them contains seven segments. The sheath flow effect at various voltage combinations was tested. Images in Figure 3.2 show the tightly pinched sample stream at the indicated voltages. Sample width can be roughly obtained from these images. For example, in Figure 3.2 D, the sample width is estimated to be 21 μm. The predicted sample width is 7.08 μm as shown in Table 3.2. The discrepancy might be from the drawback of pSpice simulation, as discussed in Chapter 2. Voltage combinations in Figure 3.2 C and D were used in the subsequent experiments. pSpice simulation results shown in Figure 3.3 and Table 3.2 provide estimates of the transit time in the fractionation zone (t fractionation zone), which allows an estimate of the diffusion induced width of the sample zone. The predicted widths are all smaller than the width of the fractionation zone channel (172 μm).

66
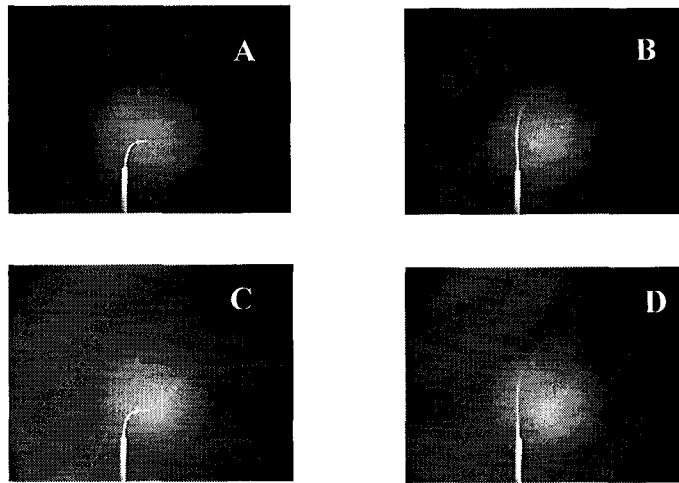
Figure 3.2 *Images show the tightly focused sample stream for the Combo design. The collection channel and sample channel were held at -2600 V and 0 V, respectively. (A) and (B) Sheath reservoirs were at 500 V; (C) and (D) Sheath reservoirs were at 1000 V.*
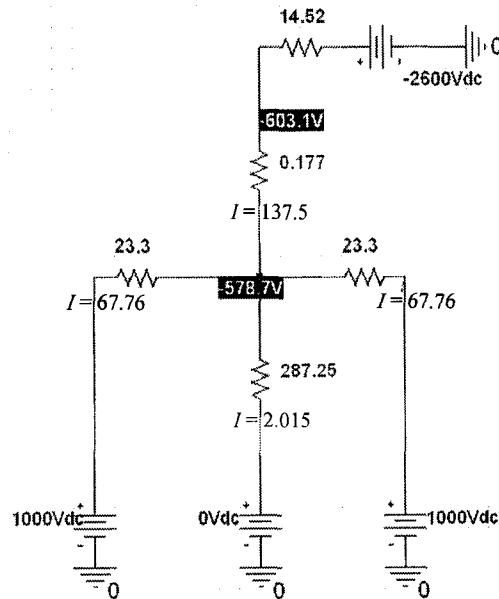
Figure 3.3 *Simulation scheme for the Combo Design for the 1st collection channel. The units of resistances and currents are the same as those in Figure 2.8.*

Table 3.2 Simulation results for the combo design

	A	B	C	D
V_{sample} (V)	0	0	0	0
$V_{collection}$ (V)	-2600	-2600	-2600	-2600
V_{sheath} (V)	500	500	1000	1000
channel at ground	1	2	1	2
$L_{fractionation\ zone}$ (μm)	150	455	150	455
I_{sample} ($V \cdot \mu m / 1000$)	2.964	2.901	2.015	1.942
I_{total} ($V \cdot \mu m / 1000$)	119.0	117.3	137.5	135.6
V_{drop} (V)	21	62.9	24.4	72.7
$E_{fractionation\ zone}$ (V/cm)	1400	1382	1627	1598
$t_{fractionation\ zone}$ (s)	0.025	0.076	0.021	0.066
d (μm)	4.06	7.08	3.72	6.60
W_{sample} (μm)	12.40	18.41	9.96	15.66

3.4 Microchip operation

Our aim was to separate protein mixtures, followed by the delivery of each purified protein into collection channels. The process was performed automatically, without operator involvement. The voltage application was divided into four stages in sequence, as demonstrated in Figure 3.4. In the first stage, sample was injected for 10 s. The voltage was then switched automatically to separation and fractionation modes at the second stage. A PMT was positioned around 1 mm before the sheath point at the intersection of the sheath and separation channels, as shown in Figure 3.1. This PMT

68

was used to select the peaks with heights over a preset threshold value. These peaks were then collected in reservoir **E1** or **E2** by applying negative voltages (-2600V) to them in sequence. The duration of the negative voltage applied to reservoir **E1** or **E2** depends on the duration of the peak. After fractionation, the stage was moved to reposition the PMT downstream. At the third stage, one of the two fractions was injected for 10 s into the CE stage and finally a CE separation of the fraction was performed, while holding **H1** negative. The entire process was controlled by an in-house written Labview program.
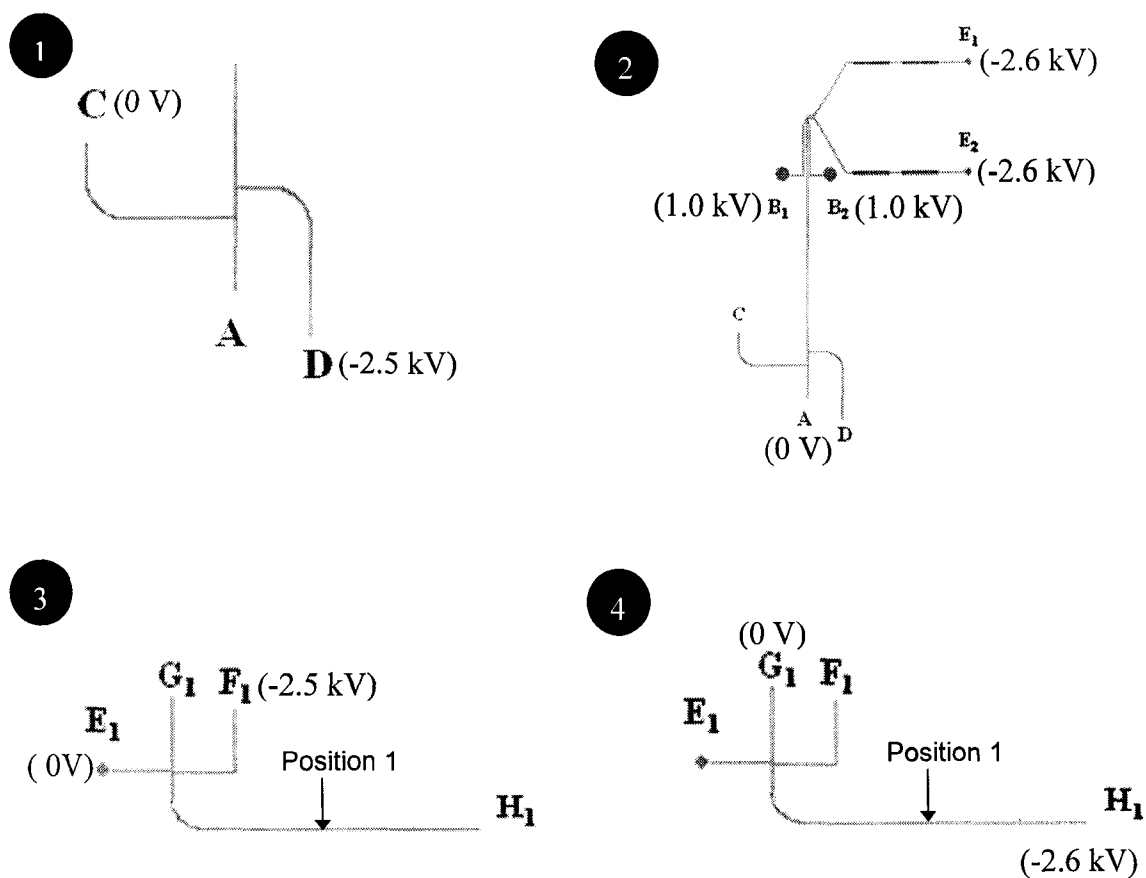
Figure 3.4 Four stages of applying voltages for fractionation, collection and separation downstream

3.5 Fractionation and collection of a protein mixture

A mixture of FITC-BSA (8×10^{-4} mg/mL) and FITC-IgG (0.02 mg/mL) in water was used as a model sample. All the buffers used were 20 mM ammonium bicarbonate. Shown in Figure 3.5 A is the electropherogram obtained when PMT was positioned to record the fluorescent signal from the separation channel before fractionation as shown by the expanded fractionator layout in Figure 3.1. In order to eliminate the unwanted components, the threshold value was set to 1.0 volt PMT signal. The power supply was programmed to direct BSA and IgG, respectively, into the top and bottom part of Figure 3.1. The same process was repeated 15 times in ~ 20 minutes. After fractionation and collection, the fractions were introduced into the CE channels downstream. The fluorescent signals (Figure 3.5 B, C and D) from position 1 (shown in Figure 3.1) were recorded. The signal intensity for the fractionated BSA and IgG are much smaller than seen in Figure 3.5 A. This is attributed to the small volume of the injector (200 μm versus 2 mm in the main separation channel) used to inject the fractionated proteins. The repetitive collection may increase the possibility that the inlets of the fractionation channels become contaminated. However, as can be seen from Fig. 3.5 B and Fig. 3.5 C, CE of the fractionated BSA and IgG shows they are substantially purified. These results verify that the collection channels are well shielded by the sheath buffers.

3.6 Conclusion

A fractionator and collector based on peak selection mode was developed. The peak selection method allows a relatively simple design, with the number of collection channels reduced to the number of components of interest. A microchip could be

70

designed for specific sample clean up and analysis steps, as in a biochemical assay for example.
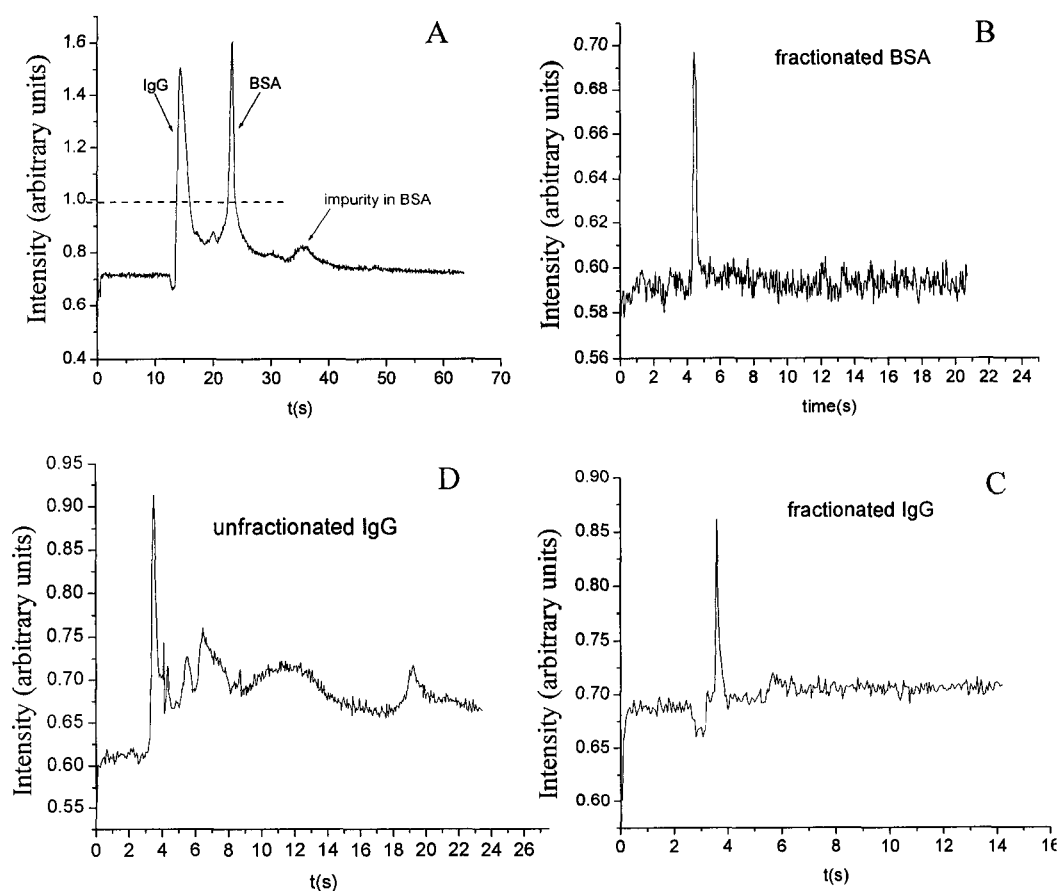
Figure 3.5 Electropherograms obtained during CZE process. (A) CE of a mixture of BSA and IgG. (B) CE in the column on the right side of Fig 3.1 after fractionation of a BSA/IgG mixture, showing the significantly purified BSA component. (C) CE in the other column on the right side of Fig 3.1 after fractionation of a BSA/IgG mixture, showing the significantly purified IgG component. (D) CE in the column on the right side of Fig 3.1, showing the unfractionated IgG is not pure.

71

4.1 Introduction

In Chapter 3, fraction collection based on peak selection was demonstrated. Although this method simplifies the microchip layout and engenders pure fractions, it has limitations that prevent wide application. The drawbacks arise from the use of a threshold value to select peaks. In order to set up the threshold value, the sample needs to be run first in order to set up the parameter for an actual fractionation. Sophisticated commercial systems have algorithms and methods to solve these problems, but it always remains a challenge. Moreover, to eliminate interference from background signal, the threshold value must be relatively high, which leads to a failure to capture components. Additionally, the signals induced by bubbles will disturb fractionation. In contrast, a fraction/unit time method can avoid those issues and can be employed to collect a large number of fractions. This is in fact the common approach of conventional systems.

In this chapter, we present a fractionator with 36 collection channels, which can collect fractions at fixed time intervals by sequentially switching high voltage relays. No physical valve is involved in this system and no peripheral mechanical parts are required other than the relays, making the device simple to use and easy to couple to other techniques. The sample stream was fractionated into individual channels by an electrokinetic driving force, with sheath buffers used to prevent cross contamination. This is an extension of the work presented in Chapter 2. More challenges were confronted, because of the much longer focused sample stream required to make an array of 36 collection channels. This chapter focuses on the design considerations and the performance of the 36-channel fractionator.

72

4.2 Design considerations

In order to direct the sample stream into a specific collection channel without contaminating the other collection channels, the sample stream needs to be focused by sheath buffers. Because multiple collection channels are distributed along the fractionation zone, the length and width of the focused sample stream in the fractionation zone determines the number of collection channels allowed. If Design **B** in Chapter 2 is used as a template, the sample stream width is estimated to be around 50 μm when it reaches the inlet of the 40th collection channel based on a device with a fractionation zone length of 3 mm. So, it should be feasible to design a fractionator with around 40 collection channels. Since the sheath effect functioned properly in Design **B**, impedances of segments of Design **B** and their related impedance values were considered as templates for designing a 36-channel fractionator. Some issues come up as the system becomes more complex. To ensure that there is enough space for access holes and reservoirs, long and nonparallel collection channels are required. Lengths and widths of these collection channels must be designed to give similar impedances to those of Design **B**.

The collection channels were designed for a 20 μm depth, with all the other channels 5 μm deep. They are on the same wafer. The chip fabrication followed Method **B** described in the experimental section of Chapter 2. Shown in Figure 4.1 and Table 4.1 is the 36-channel fractionator layout and the dimensions. The considerations will be discussed in detail in the following sections.
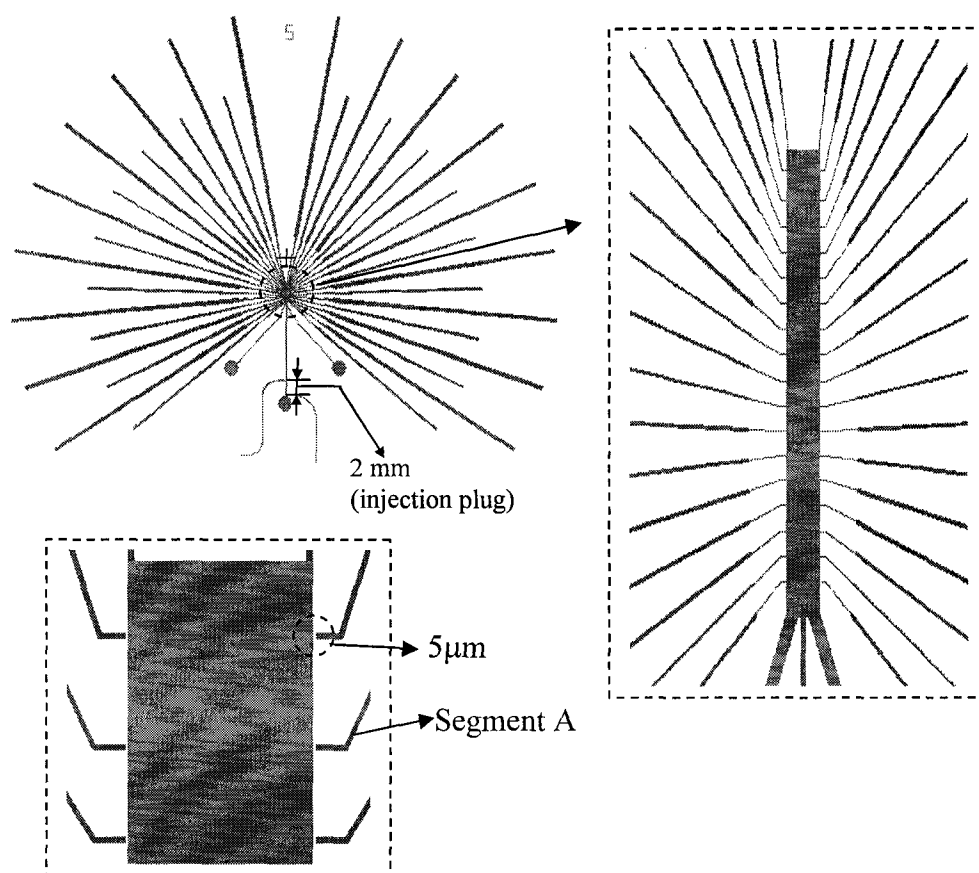
Figure 4.1 The layout of the fractionator with 36 collection channels

Table 4.1 The detailed dimensions and F factor

Fractionation zone	Sheath channel	Separation channel	Injection arms
$d = 5$ μm $w = 210$ μm $l = 2750$ μm	$d = 5$ μm $w = 88$ μm $l = 10$ mm	$d = 5$ μm $w = 30$ μm $l = 1.2$ mm	$d = 5$ μm $w = 60$ μm $l_{left} = 12.64$ mm
$d = 5$ μm $w = 310$ μm $l = 2750$ μm	$d = 5$ μm $w = 129$ μm $l = 10$ mm	$d = 5$ μm $w = 43$ μm $l = 1.2$ mm	$l_{right} = 8.46$ mm
$F = 0.00544$	$F = 0.01258$	$F = 0.03341$	$F = 0.02517$

Collection channels
$F_A = 0.07162$, $F_B = F_D = 0.07162$, $F_C = 0.03945$, $F_{E1} = 0.02241$, $F_{E2} = 0.01563$

74

4.2.1 The fractionation zone

Two fractionators were designed with fractionation zone widths of 200 μm or 300 μm. Wider channel devices were not explored, because of the increased longitudinal diffusion problem predicted by the simulation in Chapter 2. On the mask designs of both fractionators, the edges of the fractionation zone are separated from the collection channels by a 5 μm space, as shown in Figure 4.1. This distance reduces the protrusion of the collection channels into the fractionation zone. A distance longer than 5 μm could further reduce the protrusion; however, this value was selected to ensure the channels would be connected after etching. After etching, the undercutting associated with isotropic etching joins the channels together.

4.2.2 The sheath channels, separation channel, collection channels and the injection plug

For the fractionator with a 200 μm wide fractionation zone, the sheath channels have the same dimensions as Design **B** of Chapter 2 (88 μm wide and 10 mm long) because those dimensions produce a tightly focused sample stream. The separation channel is shortened to 1 cm in order to enhance the electric field in the separation channel. The collection channels are distributed evenly along the fractionation zone, spaced 150 μm apart center to center except for the last three channels. In order to keep a minimum distance of 70 μm from edge to edge between the collection channels, only 36 were located along the fractionation zone (Figure 4.1). The channels were spread to maximize the distance between access reservoirs, so that the exact distance between

75
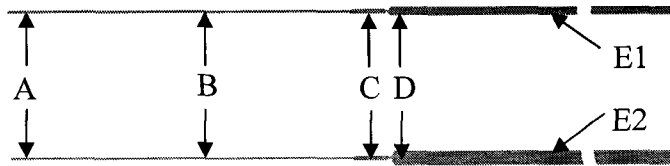
The collection channel layout when the fractionation zone is 200 μm wide

Segment A: l = 350 μm, w = 50 μm; Segment B: l = 9750 μm, w = 56 μm;
Segment C: l = 1000 μm, w = 140 μm; Segment D: l = 100 μm, w = 56 μm;
Segment E1: l = 20 mm, w = 274 μm; Segment E2: l = 30 mm, w = 408 μm.
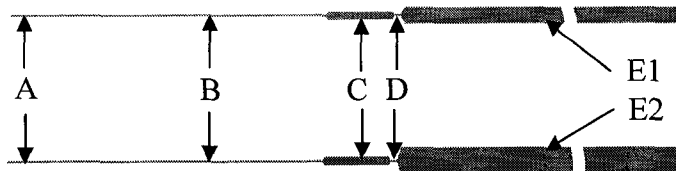
The collection channel layout when the fractionation zone is 300 μm wide

Segment A: l = 350 μm, w = 50 μm; Segment B: l = 5140 μm, w = 56 μm;
Segment C: l = 1000 μm, w = 140 μm; Segment D: l = 100 μm, w = 56 μm;
Segment E1: l = 20 mm, w = 274 μm; Segment E2: l = 30 mm, w = 408 μm.

Figure 4.2 *The detailed dimensions of the collection channels for the fractionators with 200 μm and 300 μm fractionation zone, respectively*
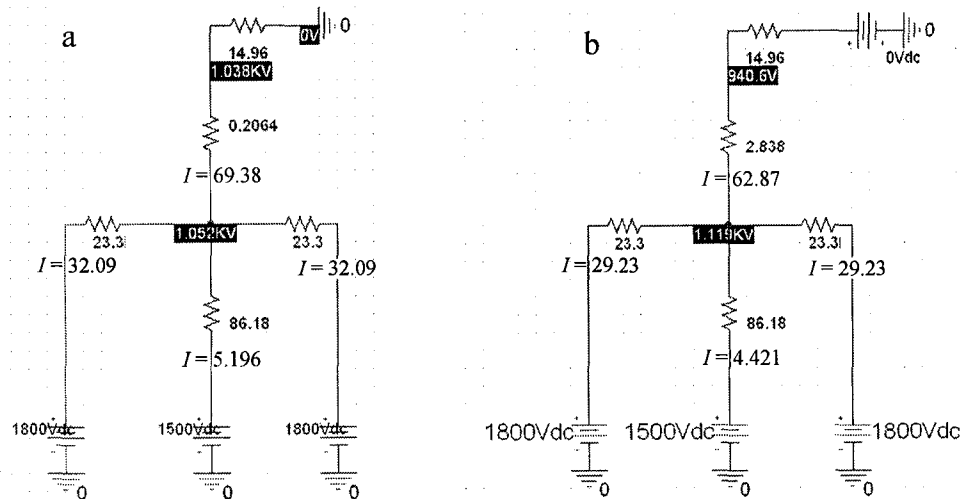
Figure 4.3 *Simulation scheme for 200 μm fractionation zone device with the 1st (Figure 4.3 a) and the 18th (Figure 4.3 b) channel at ground, respectively. The predicted sample stream widths are 30 μm and 66 μm, respectively. The units of resistances and currents are the same as those in Figure 2.8.*

76

channels varied. There are two types of collection channels with different lengths (3 cm and 4 cm) and widths as shown in Figure 4.2 a, and each of them contains five segments. These two types of collection channels have equal electric impedance. Segment **B** is similar to the collection channel of Design **B**. The impedance of Segment **B** is the main source of total impedance of the collection channel. Segment **C** is designed as a protein absorption bed, wherein a photoinitiated polymerization reaction is to be used to fabricate digestion or extraction beds, as will be discussed in the next chapter. Long (4 cm) and short (3 cm) collection channels are distributed alternately, which provides enough room for drilling access holes. The pSpice simulation indicates this fractionator should create a nicely focused sample stream, as shown in Figure 4.3. The sample stream widths predicted by the pSpice simulation are 30 μm and 66 μm at the 1st and 18th collection channel, which is smaller than the fractionation zone width (210 μm).

For the fractionator with a 300 μm wide fractionation zone, channel widths of all the other channels are adjusted in order to have the same values of relative impedance as those for the fractionator with a 200 μm wide fractionation zone. Therefore, a suitable voltage combination for the 200 μm wide fractionation zone device should also function well on the 300 μm wide fractionation zone device.

The volume of the injection plug (l = 2 mm, w = 43 μm, d = 5 μm) is 0.4085 nL. The total injection amount will be 20 fetomoles for a protein (1mg/mL) with a molecular weight of 20,000. This amount of protein molecules will be fractionated into 36 collection channels. If the fractionation process is repeated 36 times, each collection channel will collect 20 fetomoles of protein molecules which is enough for the MS identification.

77

4.3 Experimental

High voltages were applied to the sample reservoir and sheath reservoirs. The collection channels were grounded through a high voltage relay box. A timer control box was employed to switch the relays. There are 20 relays in the system. Each of them was connected to one of the reservoirs through platinum electrodes to perform the sequential switching. This system has been used previously by Justine Taylor in this research group [1]. Figure 4.4 shows a picture of this system.
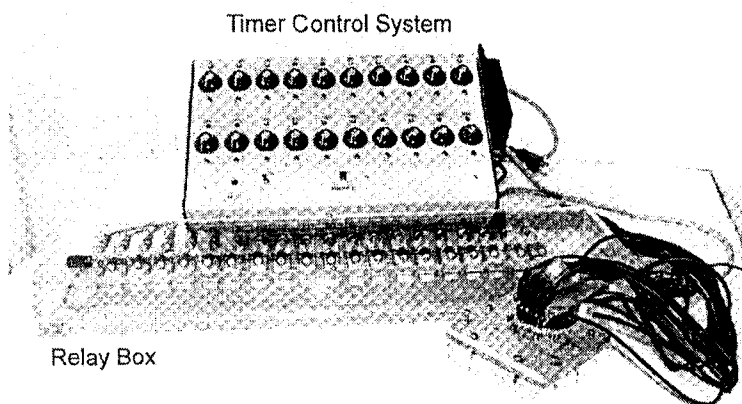
Figure 4.4 The picture of the high voltage box and time control box (*Adapted from Ref [1]*)

The fluorescent microscope setup was similar to that described in other chapters, except that the laser beam illuminates the device from above, and was expanded with a cylindrical lens into a linear beam. The resulting 3 mm long beam covers the entire fractionation zone (2750 μm long) with sufficient intensity to excite detectable fluorescence emission.

4.4 Results and discussion

4.4.1 Measuring delay time

A delay time exists between the adjacent relays, which will result in additional diffusion of the sample stream. The delay time was evaluated with the system connected to two low voltage sources through the high voltage relays and the timer box. Data were collected at 10^4 points/s as shown in Figure 4.5. The measured delay time may be more accurate at a higher collection rate, however, the computer did not function well at higher rates. All the relays were measured because of slight differences between them. The results are listed in Table 4.2 (obtained at 10^4 points/s). The delay times for all the relays were less than 1 ms. The delay time was averaged to be 468 µs for the 20 relays. The diffusion distance within 468 µs is predicted to be around 0.6 µm. The diffusion distance due to the delay time will become 11.4 µm when sample stream reaches the last collection channel.
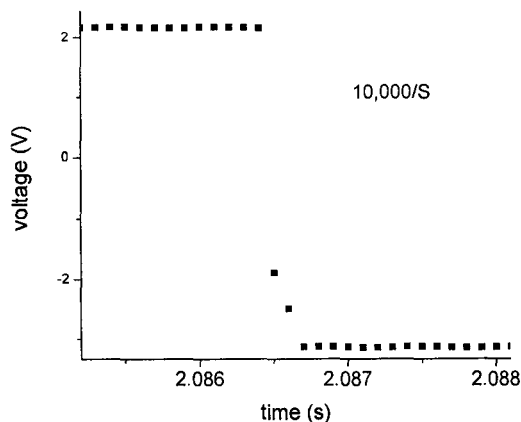
Figure 4.5 *Measurement of delay time at different data collection rates*

79

Table 4.2 The delay time for all the relays

	Time (μs)		Time (μs)
1-2	300	11-12	700
2-3	400	12-13	400
3-4	400	13-14	300
4-5	400	14-15	500
5-6	100	15-16	500
6-7	600	16-17	600
7-8	600	17-18	900
8-9	400	18-19	500
9-10	400	19-20	600
10-11	300		

4.4.2 Sheath flow effect test

The sheath flow effect on the 300 μm wide fractionation zone was tested, with the collection channels on both sides switched to ground individually. The results are shown in Figure 4.6 and 4.7. Afterwards, the channels on the right side were grounded, sequentially controlled by the high voltage relay box. The results are shown in Figure 4.8. In all the sheath flow effect tests, the sample reservoir and the two sheath reservoirs were held at 1.5 kV and 1.8 kV respectively. The images in Figures 4.6, 4.7 and 4.8 show that the sample stream was focused tightly by the sheath streams and delivered to the grounded collection channel without contamination in other floating channels. The images demonstrate that the sample stream becomes wider and wider as it travels along the fractionation zone, as expected. In Figure 4.6, sample stream widths are estimated to increase from 40 μm to 100 μm between the 1st and 18th collection channel. Figure 4.9 shows the impedances and the simulation scheme with the 1st and 18th channels at ground. The sample stream widths predicted by the pSpice simulation are 37 μm and 74 μm at the 1st and 18th collection channel. The difference between predicted and

80
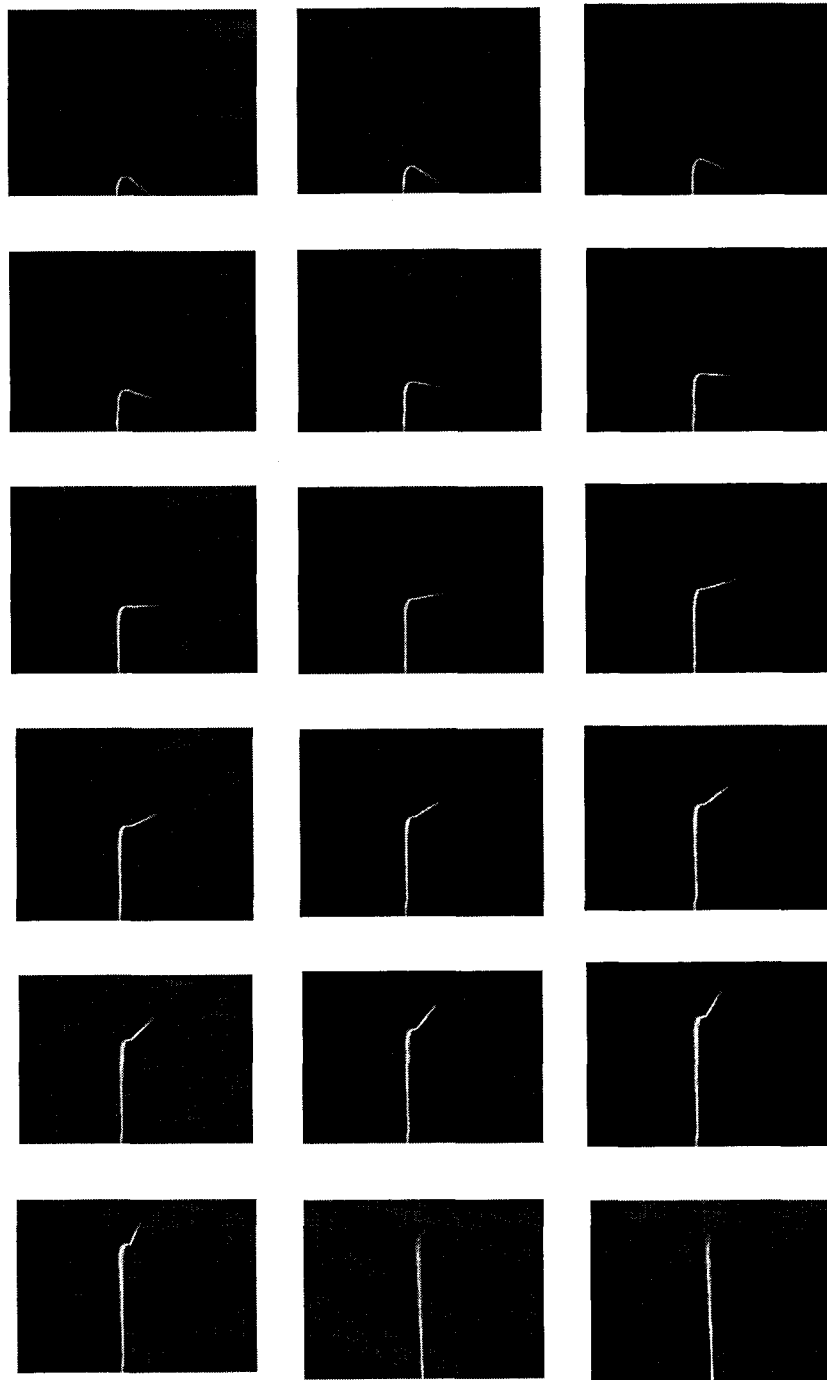
Figure 4.6 *Images show the fluorescein stream was delivered into individual collection channels on the right side under the protection of sheath streams. The experiments were performed on the multiplexed fractionator with 300 μm wide fractionaton zone. Sample voltage: 1.5 kV, sheath voltage: 1.8 kV. Collection channel was grounded individually. Buffer: 20 mM NaOH. The fluorescein was 200 μM in 20 mM ammonium bicarbonate.*

81
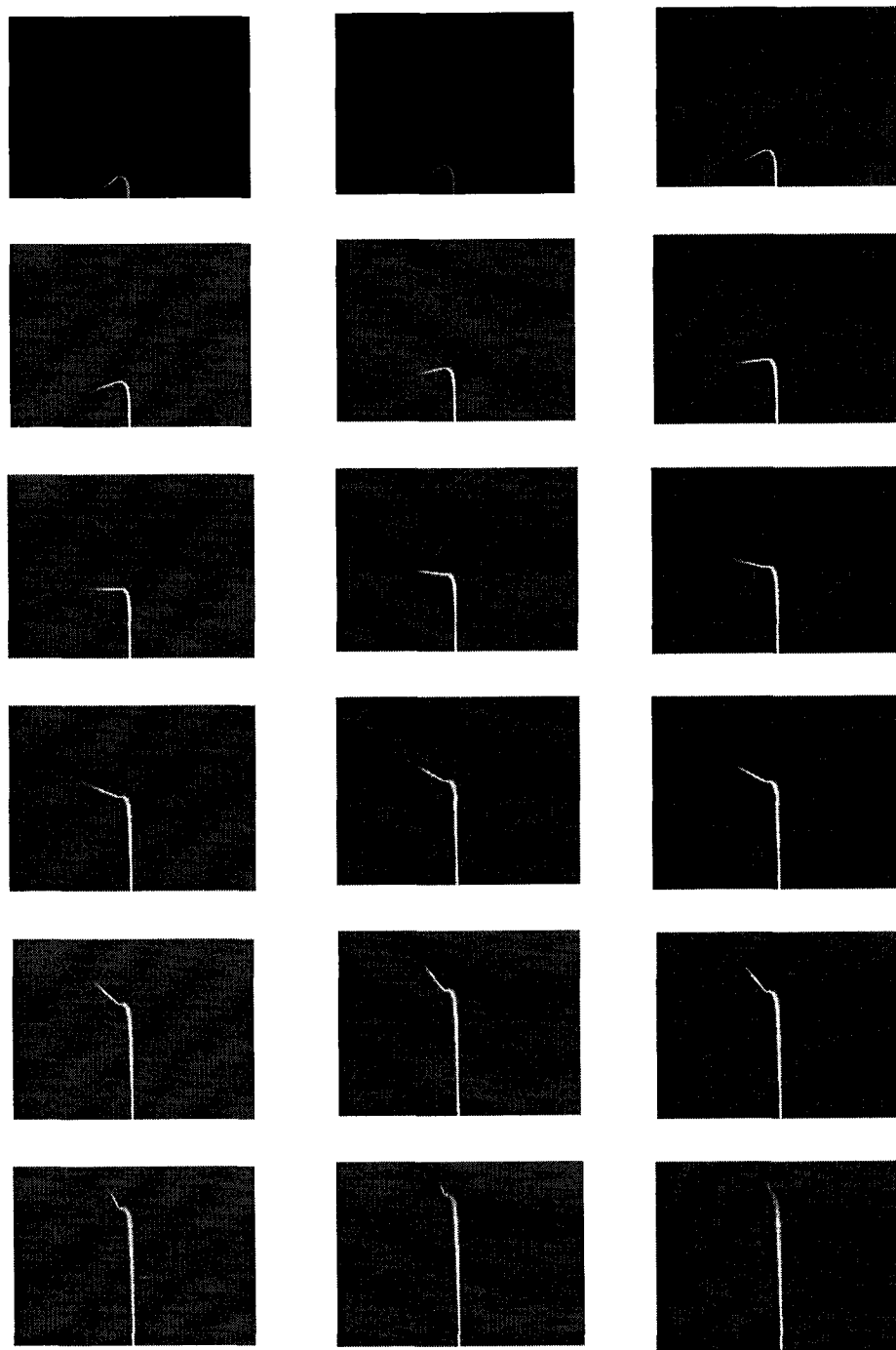
Figure 4.7 Images show the fluorescein stream was delivered into individual collection channels on the left side under the protection of sheath streams. Sample voltage: 1.5 kV, sheath voltage: 1.8 kV. Collection channel was grounded individually. Buffer: 20 mM NaOH. The same device design and fluorescein solution as those in Figure 4.6 was used.

82
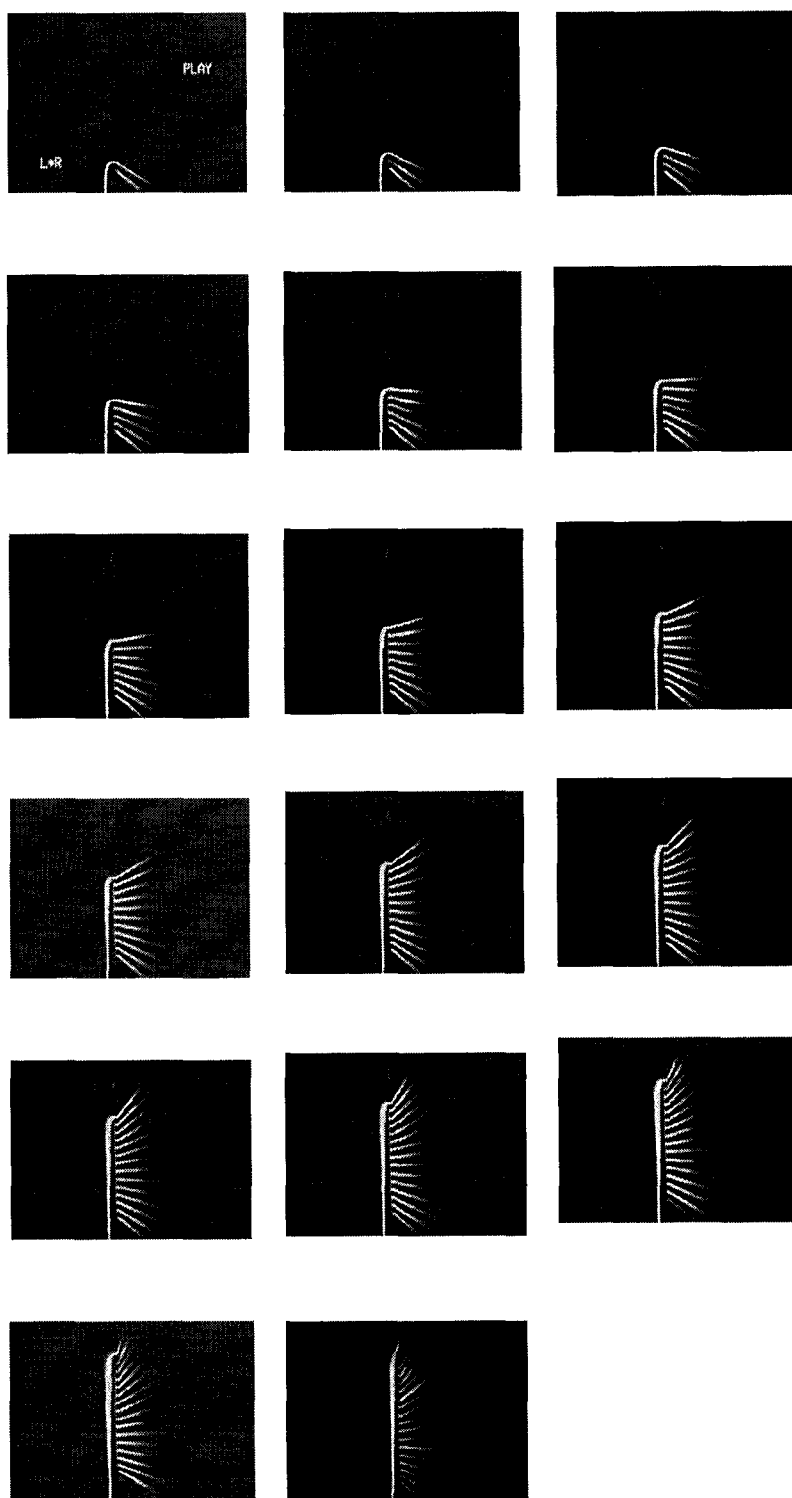
Figure 4.8 Images show the fluorescein stream was delivered into individual collection channels automatically controlled by the high voltage relay box. Sample voltage: 1.5 kV, sheath voltage: 1.8 kV. Collection channel was grounded individually. Buffer: 20 mM NaOH. The same device design and fluorescein solution as those in Figure 4.6 was used.

83
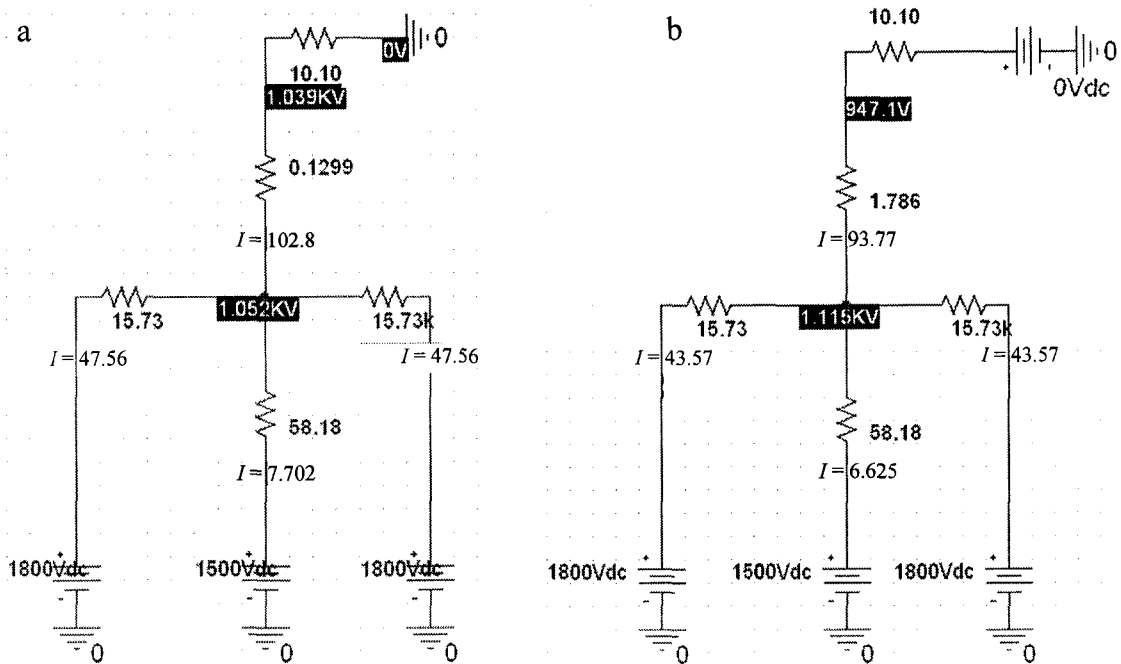
Figure 4.9 *Simulation scheme for 300 μm fractionation zone device with the 1ˢᵗ (Figure 4.9 a) and the 18ᵗʰ (Figure 4.9 b) channel at ground, respectively. The predicted sample stream widths are 37 μm and 74 μm, respectively. The units of resistances (R) and currents (I) are the same as those in Figure 2.8.*

observed sample stream widths with the 18ᵗʰ collection channel at ground may partially relate to the diffusion induced by the relay time.

Because the sample stream width is still smaller than the fractionation zone width as shown by Figures 4.6, 4.7 and 4.8, it is possible to employ a longer fractionation zone with more collection channels on both sides. When sample and sheath voltages are 1.5 kV and 1.8 kV, respectively, the sample stream width is predicted to be 138 μm when it reaches the end of a 7350 μm long and 310 μm wide fractionation zone, such a long fractionation zone easily allows for 100 collection channels.

84

4.4.3 Necessity of electrokinetically driven flow

This fractionation design can be effectively driven by electrokinetic forces, but fails to function properly when driven with hydrodynamic force. This phenomenon was accidentally discovered when attempting to flush the chip with a pump operating at 2 μL/min, with entry through the sample and the two sheath reservoirs. Substantial leakage into the two injection arms was expected, but it was a surprise that only the first few collection channels received outflow. No observable flow occurred into the 5th (counting along one side, so ~10th overall) and later collection channels. Pressure driven laminar flow has been reported to focus flow and pattern the internal surface of a microchannel. However, in our case, hydrodynamic focusing is not effective because the flow is split quickly, due to the collection channels.

A simulation was performed to verify the observation. It is possible to use Pspice software for this simulation, if we treat the pressure and flow resistance as an equivalent voltage and impedance, respectively. This method has been used to simulate hydrodynamic flow [2]. Pressure driven steady state flow in microfluidic channels is referred to as Hagen-Poiseuille flow [3-5]. The flow resistance is given by

$$R_{flow} = \frac{\Delta P}{Q}$$

where R_{flow}, ΔP and Q are flow resistance, pressure drop and volume flow rate, respectively. For rectangular channels, the equation can be described by

$$R_{flow} = \frac{\Delta P}{Q} = \frac{4\eta L}{w^2 d^2 F}$$

where η is the viscosity of the fluid; L, w and d are the channel length, width and depth; F is a geometric factor related to d and w[6]. Bao et al [7] studied the F term in detail

85

for the D-shape channel resulting from isotropic etching, and derived an empirical equation to calculate F as follows,

$$F = 0.3468\left(\frac{d}{w}\right) - 0.6230\left(\frac{d}{w}\right)^2 + 1.2466\left(\frac{d}{w}\right)^3 - 2.7916\left(\frac{d}{w}\right)^4 + 3.3696\left(\frac{d}{w}\right)^5$$

The calculated F factors according to this equation are shown in Table 4.1. The value of w is taken as the width at the top of the D-shape channel, and d is the maximum depth. Figure 4.10 demonstrates the calculated flow resistances and the simulation scheme where an arbitrary voltage was applied to the sample reservoir and sheath reservoirs. Obviously, the current flow, which is directly proportional to volume flow rate, decreases quickly as the liquid travels further down the fractionation zone. By the fifth pair of collection channels the flow rate is 3.2% of the value at the first collection channels.

4.5 Conclusion

This chapter demonstrates a fractionator and collector in space which can be operated at fixed time intervals for fractionation. The 36 collection channels increase the fractionator's throughput and further increase of the number of fractionation channels is feasible on the basis of our results. The sample stream can be delivered to the grounded channel with no contamination of the other channels. The electrokinetically driven flow and hydrodynamic flow in this device were compared. The advantage of electrokinetically driven flow over hydrodynamic flow was embodied in the ability of electrokinetically driven flow to direct flow equally into individual channels on our device with multiple outlets.

86

Figure 4.10 Schematic simulation of the hydrodynamic flow. All the flow resistances are displayed in the scheme as electrical impedances. The resistances are in $1000 \cdot \mu m^{-1}$. 1 mA of current (I) in this simulation scheme corresponds to $1 \ V \cdot \mu m / 1000$.

87

4.6 Reference

1. Taylor, J. Harrison, D.J. *Proceedings of MicroTAS*, **2002**, 344-346.

2. Stiles, T.; Fallon, R.; Vestad, T.; Oakey, J.; Marr, D.W.M.; Squier, J.; Jimenez, R. *Microfluid Nanofluid* **2005**, 1, 280-283

3. Ahn, J.J.; Oh, J.G.; Choi, B. *Microsystem Technologies* **2004**, 10, 622-627.

4. Zengerle, R.; Richter, M. *J. of Micromech. Microeng.* **1994**, 4, 192-204.

5. Aumeerally, M.; Sitte, R. *Simulation Modeling Practice and Theory* **2006**, 14, 82-94.

6. Mortensen, N.A; Okkels, F.; Bruus, H. *Physical Review E*, **2005**, 71, 057301.

7. Bao J.B.; Harrison D.J. *AIChE Journal* **2006**, 52, 75-78.

88

5.1 Introduction

As mentioned in previous chapters, the 36-channel fractionator will be merged into a protein analysis platform on microchip. The digestion of protein on chip should immediately follow the fractionation step. The fractionated protein can be collected into a reservoir and be digested in a homogeneous reaction, or adsorbed onto a solid support and then digested on site. Because the sample stream will have been diluted by the sheath streams, homogeneous digestion will be slow, and detection downstream will become a problem as well. Therefore, it is best to concentrate the protein before further analysis.

Different types of protein concentration methods are available, such as isoelectric focusing (IEF), isotachophoresis, field amplified sample stacking and solid phase extraction (SPE). The most practical concentration method for this fractionation design is some version of SPE. The bed could be made by coating the walls, packing conventional beads, or using monolithic polymer columns.

The particle packing method is feasible if only a single channel or small number of channels need to be packed. In our system, 36 channels need to be packed in specific regions. Taylor [1] showed that it is difficult to pack so many channels with equal flow resistance, which is required if the device is to operate properly. Instead of bead packing, photoinitiated polymerization [2-6] may be a good choice, because the polymer can form in a specific region with good edge resolution and reproducible properties. Moreover, the reaction can occur in different regions at the same time.

In this chapter, we describe the efforts to make monolithic polymer beds within the bed regions of the fractionator. The conditions for protein adsorption and elution from

89

the polymer beds were studied. Different monomers and porogens were investigated in order to obtain a polymer bed with sharp edges and low flow resistance, so that the polymer bed has little effect on the sheath flow effect, compared to a fractionator without polymer beds.

5.2 Experimental

Chemicals

Butyl methacrylate (BMA) was from Fluka (Seelze, Germany). Ethylene glycol dimethacrylate (EDMA), 2,2-Dimethoxy-2-phenyl-acetophenone (DPA), 4-(Dimethylamino)-benzophenone (DMAP) were from Aldrich (USA). Benzoin was obtained from General Intermediate of Canada (Edmonton, Alberta, Canada). Acrylamido-methyl-propane sulfonate (AMPS) was from Aldrich (Oakville, Ontario, Canada). Alumina Basic and 1-octanol were from Fisher Scientific (Ottawa, Ontario, Canada). Methanol, cyclohexanol, 1,4-butanediol, isooctane, hexane, toluene, FITC-Avidin and FITC-BSA were purchased from Sigma (Oakville, Ontario, Canada). UV transilluminator was obtained from Spectronics Corporation (Westbury, NY, USA).

Preparation of monolithic polymer bed

The inhibitor was removed from the monomer (butyl methacrylate), and crosslinker (ethylene glycol dimethacrylate) by passing through a basic alumina column which was made by loading the alumina powder in a syringe, with a filter (0.2 μm) underneath to prevent alumina powder from eluting. The monomer, crosslinker and solvents were degassed individually before mixing with initiator. The filtered mixture

90

was introduced into the chip by capillary force. Afterwards, the same amount of water was loaded into each reservoir before sealing with parafilm. The chip was then placed on top of a photo-mask and bonded with black tape after alignment. The dimensions of chips and masks will be described in the Results and Discussion section. The mask and chip were brought to the plane of the transilluminator for exposure. The UV light illuminated from underneath the mask. A cooling fan was located beside the transilluminator to reduce thermal polymerization. After exposure, the polymer bed was rinsed with methanol/water (50:50, v/v) to remove solvent and residual monomers, followed by rinsing with water. Pictures of the polymer beds were taken using different magnification objectives, instead of scanning electron microscopy (SEM). Because the channel can be regenerated after the polymerization reaction, and the chip fabrication is expensive, it is not economical to cut the microchannel to expose the polymer and take SEM pictures for each sample.

5.3 Results and discussion

5.3.1 Effects of reaction conditions on the polymer structure

To adsorb protein, we chose BMA as the functional monomer, because it is hydrophobic due to the methyl groups. Table 5.1 lists all the conditions investigated.

Table 5.1 The composition of the reaction mixture

Solution No.	EDMA(g)	BMA(g)	Initiator (mg)	Solvents (g)	Exposure time (min)
1	0.24	0.36	Benzoin (7.0)	Methanol (0.9)	8, interface not good
2	0.24	0.36	DPA (6.3)	Octanol (0.9)	8, interface not good
3	0.24	0.36	DPA (6.0)	Methanol (0.45) Glycerol (0.45)	8, only a little reaction

to be continued

91

4	0.13	0.18	DPA (3.5)	Methanol (0.225) Octanol (0.225)	14, only a little reaction
5	0.24	0.36	DPA (6.0)	1,4-Butanediol cyclohexanol	8, interface not good
6	0.12	0.18	DMAP (6.0)	Octanol (0.45)	13, slow reaction
7	0.24	0.36	DPA, (6.1)	Methanol (0.9)	reacted everywhere
8	0.12	0.18	Benzoin (6.0)	Isooctane (0.23) Toluene (0.23)	8, no reaction
9	0.12	0.18	DPA (5.3)	Octanol (0.3) Cyclohexanol (0.15)	8, milky product
10	0.12	0.18	DPA (5.5)	Octanol (0.6)	8, product diffused
11	0.12	0.18	DPA (5.5)	Octanol (0.75)	8, product diffused
12	0.12	0.18	DPA (5.5)	Octanol (0.9)	8, product diffused
13	0.12	0.18	Benzoin (2.7)	Octanol (0.45)	8, half of bed
14	0.1261	0.1842	Benzoin (3.7)	Octanol (0.4664)	8, good
15	0.1187	0.1803	Benzoin (3.3)	Octanol (0.4532) Methanol (0.1025)	8, almost no reaction
16	0.1239	0.1837	Benzoin (3.4)	Methanol (0.4533)	8, milky product, no flow
17	0.1264	0.1807	Benzoin (3.9)	Octanol (0.8931)	8, Sparse reaction
18	0.1190	0.1875	Benzoin (3.7)	Octanol (0.4657) AMPS (0.0471)*	5 min, nothing, 6min and 8min, good
19	0.1234	0.1674	Benzoin (3.9)	Octanol (0.3764) AMPS (0.1032)*	8, good, resistance bigger than #40
20	0.1234	0.1674	Benzoin (3.9)	Octanol (0.3764) AMPS (0.2032)	20, good
21	0.1382	0.1872	Benzoin (3.4)	Octanol (0.4506) Toluene (0.0549) AMPS (0.0482)*	8, little reaction

to be continued

92

22	0.1307	0.1626	Benzoin (3.9)	Octanol (0.4530) Toluene (0.0610) AMPS (0.1168)*	13,14,16,20min, good 10 min, no reaction
23	0	0.07	Benzoin (2.8)	AMPS in octanol 0.(14)**	No reaction
24	0	0	Benzoin (0.2)	AMPS (0.5)*	No reaction
25	0.1345	0.1794	Benzoin (3.3)	Octanol (0.4456) Toluene (0.0622) AMPS (0.0631)*** Methanol (0.0606)	No reaction
26	0.1366	0.1620	Benzoin (3.4)	Octanol (0.4602) Toluene (0.0600) AMPS (0.1620)*	started at 12 min, 14min and 16min, good
27	0.1118	0.1788	Benzoin (3.7)	Methanol (0.6164) Hexane (0.2470)	No reaction
28	0.1300	0.1870	DPA (4.3)	Methanol (0.6323) Hexane (0.2853)	No reaction
29	0.1199	0.1849	Benzoin (2.8)	Methanol (0.6094) Hexane (0.2678)	No reaction
30	0.1199	0.1849	Benzoin (7.0)	Methanol (0.6094) Hexane (0.2678)	No reaction
31	0.1248	0.1852	Benzoin (3.7)	Octanol (0.4550)	
32	0.1247	0.1860	DPA (3.7)	Octanol (0.4563)	

*AMPS 0.1g in 1.9g methanol; ** 0.2 g AMPS in 1.8g octanol and 0.22g water; ***0.2 g AMPS in 2.0 g methanol*

5.3.1.1 Porogenic solvent type, ratio and reaction time

As demonstrated in Table 5.1, a good interface was only created when octanol was the porogen. This may be related to the viscosities of porogenic solvents. The viscosity

93

of octanol was the highest among all the other solvents we have studied, resulting in less chance for the photoinitiated free radicals to diffuse. This may explain why the interface is sharply defined.

The porogen ratio in the mixture has an effect on the polymer structure [4, 5]. We attempted to increase the porogen ratio in order to obtain a large pore size, using solutions # 10, 11 and 12. The higher ratio of solvent resulted in more sparse structures, as shown in Figure 5.1. However, the sparse structure is fragile and collapses easily. Solution #14 was used to study the effect of the reaction time on the structure. A longer reaction time gives a denser structure, as demonstrated in Figure 5.2, however, the conversion of monomer will reach a plateau after a specific time. We did not study the structure as a function of reaction time any further, since it is not the focus of this chapter.
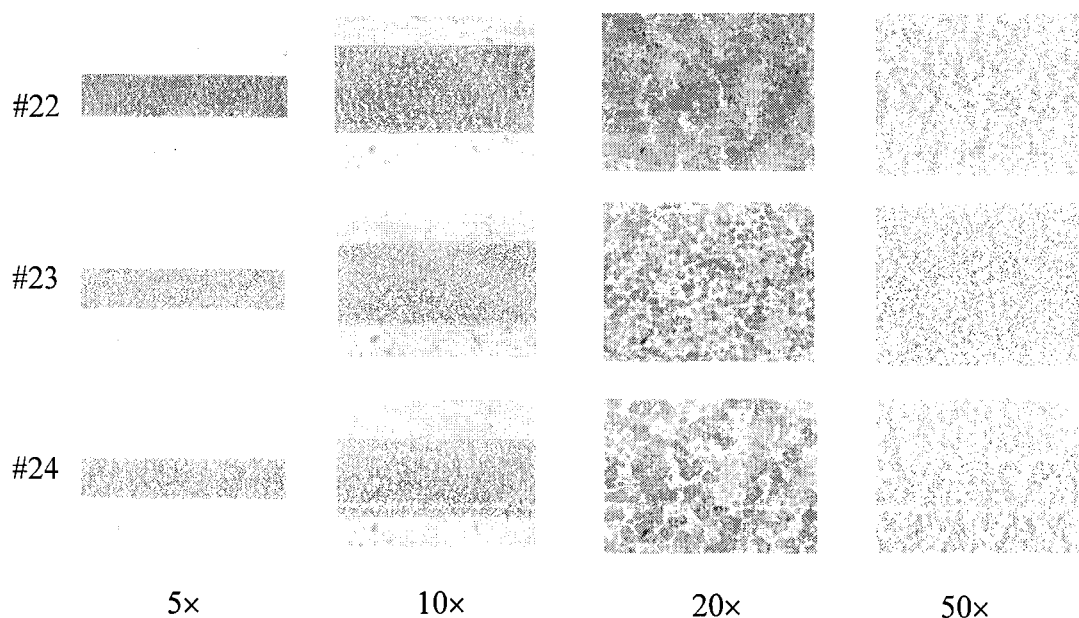
Figure 5.1 Images show the effect of porogen ratio on the polymer structure. The monomer to porogen ratios are 2:4, 2:5 and 2:6, respectively, corresponding to the entries of 10, 11 and 12 in Table 5.1 .

94

a   b
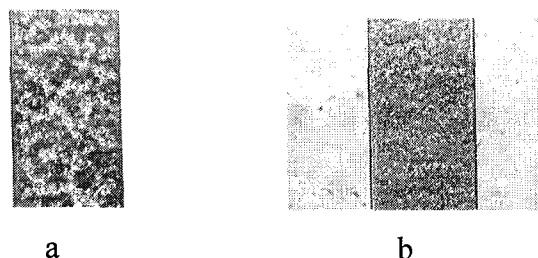
Figure 5.2 Images show the effect of reaction time on the polymer structure. Solution #14 in Table 5.1 was reacted for 5 min (a) and 8 min (b), respectively.

5.3.1.2 Mask designs for UV exposure

The window size had an impact on the reaction time and the polymer structure. In Figure 5.3, **A**, **B** and **C** illustrate three transparency masks with different exposure window sizes. These were used in all the polymerization reactions, unless otherwise stated. Figure 5.3 D shows the mask design of the chip. Each channel contains a wide region (shown by the enlarged view in Figure 5.3D) where a protein adsorption bed will be formed by photoinitiated polymerization reaction. Detailed dimensions of the chip were described in Chapter 4. On mask **A**, the UV exposure window size is the same as the final dimension of the fabricated reaction bed (140 μm wide and 1 mm long). On mask **B**, the window is enlarged from 140 μm to more than 1 cm wide while the length is kept unchanged. On mask **C**, the length is reduced to 0.5 mm while the width is the same as that on mask **B**. The single channel chip has exactly the same dimensions as one of the collection channels in the fractionator design.

With Mask **A**, the polymer prepared from solution #14 started to form on one side of the bed at 25 min, and a longer exposure time did not help the polymer fill up the entire bed. This might be explained by the poor collimation of the transilluminator. Because the light from it is not exactly vertical to its plane, when the light passes

95

through the exposure window, only part of the bed is exposed and the intensity is not as strong as when it illuminates perpendicularly. For Mask **B**, the polymer formed in the entire bed after 8 min for solution #14. However, with a 1 mm long window, the polymer always grew beyond the bed region. This increased the flow resistance of the narrower channels joined with the bed, or even worse, plugged them. This effect may arise from diffusion [7] of free radicals outside the window length. On Mask **C**, the exposure window is only 500 μm long instead of 1 mm. For this design the reaction was confined within the bed region as shown in Figure 5.4. Consequently, Mask **C** was used in all the following experiments.
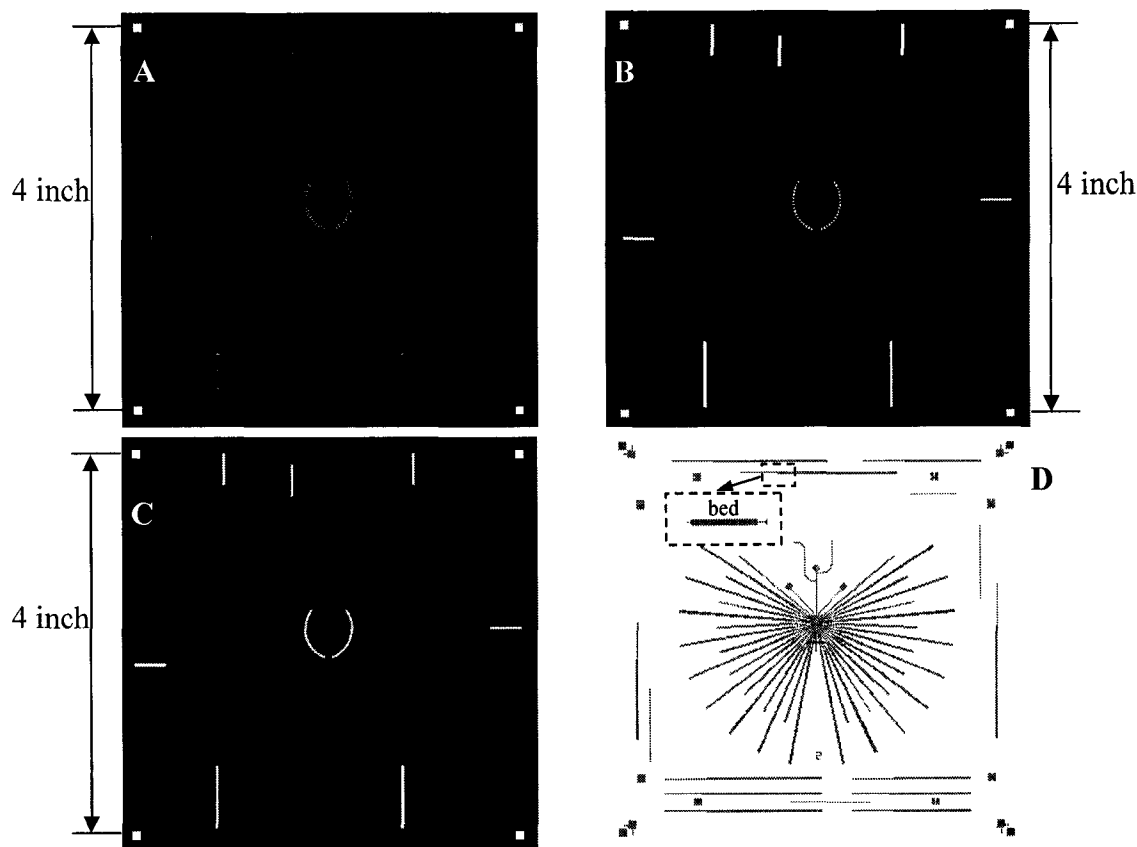
Figure 5.3 The mask designs for UV exposure (black) and the chip design shows the single channels around the fractionator. The dimensions of the fractionator and single channels were described in Table 4.1 and 4.2.
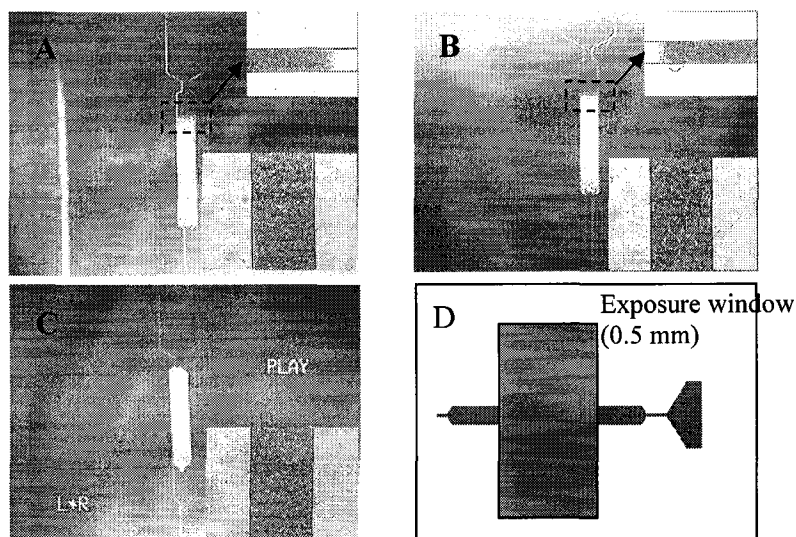
Figure 5.4 A, B and C *images show the reproducibility of the polymerization reaction which happened in the single channel device shown in Figure 5.3 D. Inserted images show the sharp edges and uniform polymer structure.Figure 5.4 D shows the exposure window was aligned in the middle of the bed. Solution #14 was reacted for 8 min.*
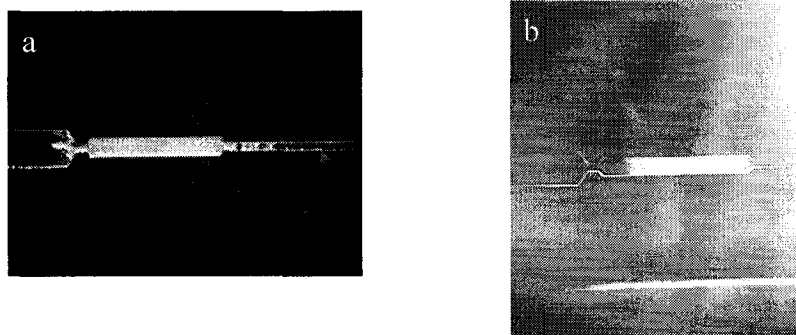
Figure 5.5 *Images show the effect of initiator on the interface (Figure 5.5 a) DPA (Figure 5.5 b) Benzoin Solution #31 and 32 were reacted for 8 min, respectively, in the same devices as those in Figure 5.4.*

97

5.3.1.3 Initiator type

Three initiators, DMAP, benzoin and DPA, were investigated. DMAP was found to initiate the reaction slowly, as demonstrated in Table 5.1. Under the same conditions (#31 and #32 in Table 5.1), the DPA initiated reaction extended far beyond the exposure region, as compared to a benzoin initiated reaction, as shown in Figure 5.5. This may be because the higher solubility of DPA in octanol leads to a higher concentration of photoinitiated free radicals.

5.3.1.4 Reproducibility of the polymerization reaction

We studied the reproducibility of the polymerization reaction using solution #14, since the polymer bed prepared from this solution has a better interface. The reaction in three individual single channels produced similar results, as shown by the inserted images in Figure 5.4. The pictures were taken after flushing with a methanol/water solution, followed by removal of the solvents. The polymer bed in Figure 5.4 C illustrates that the polymer can be moved by flushing because the channel wall is not modified [8-9] to immobilize the polymer. However, the polymer bed cannot move out of the bed region due to the restriction caused by the narrowing channels.

5.3.1.5 Amount of initiator

Solution #13 and #14 containing 0.9% and 1.2% initiator, respectively, were used to study the influence of the concentration of the initiator. The reaction lasted for 8 min. The polymer bed prepared from #13 (Figure 5.6) was only half filled and sparse, compared to the uniform and dense polymer structure prepared from solution #14 in

98

Figure 5.4. The amount of the initiator is 1-2 % (w/w) [10, 11] of the total amount of monomer plus crosslinker. A large amount of initiator will trigger the reaction so fast that cracks form, which leads to a non-uniform porous structure.

Figure 5.6 Image shows the sparse structure prepared from solution #13. Solution #13 was reacted for 8 min in the same device as that in Figure 5.4.

5.3.1.6 Interface movement induced by channel geometry

It was found that the channel geometry has a great effect on the interface. The single channel device shown in Figure 5.3 D and a Y-shape device shown in Figure 5.7 A were used in this study. As shown in Figure 5.4 A, B and C, although the mask was aligned in the middle of the bed (Figure 5.4 D) and the liquid in both reservoirs was at the same level, the polymer was not symmetrically located in the bed because the two interfaces moved in the bed region. The same thing happened in Y shaped channels, as shown in Figure 5.7, whether the access holes were sealed with tape, or covered with water before sealing with parafilm. This same behavior was not observed in a straight channel with a uniform width or the fractionatior with 36 channels. In the latter case, the channels seemed to balance each other so that no flow induced interface movement was observed.
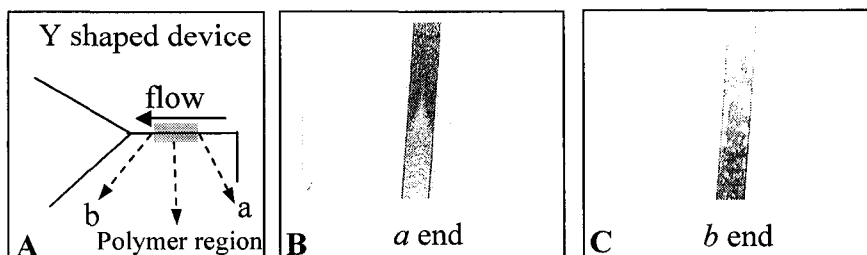
Figure 5.7 *Images show both the interfaces were disturbed by flow on a Y shaped device. Solution #14 was reacted for 8 min.*

5.3.2 Characteristic of the monolithic polymer

The morphology of polymers produced in large and small confined geometries may not be the same. Researchers have studied the dependence of the formation of methylsiloxane gel on capillary dimension [12]. When the capillary diameter decreased from 100 μm to 10 μm, the methylsiloxane did not form its typical porous gel structure. Our experiments show that some polymerization reactions do not happen in thin channels, whereas they do in large channels. Our own results support this, as discussed in Section 5.3.5.3. However, no detailed study on the effect of channel size on BMA polymerization reaction exists. For that reason, studies of bulk material are not fully instructive.

The pore size of BMA polymer formed from a large scale reaction in an unconfined space was measured using an AutoPore IV 9500 porosimeter (Micromeritics Instrument Corporation). Solution #14 was used to make the monolithic porous polymer in a sample vial. The polymer was removed, extracted with methanol and treated under vacuum overnight. Around 0.6 g of polymer was loaded into a measuring cell of a

100
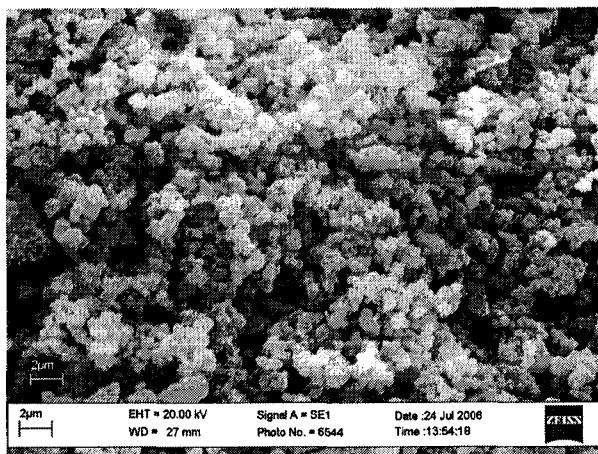
Figure 5.8 *SEM image of the polymer structure prepared from solution #14. Solution #14 was reacted for 8 min.*
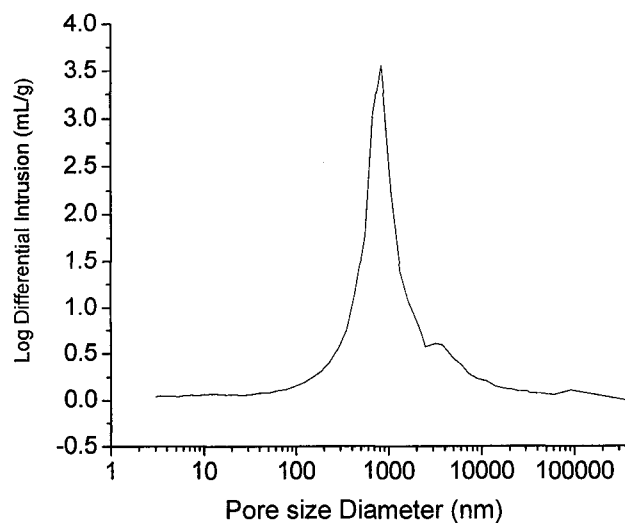
Figure 5.9 *Measurement of pore size of the polymer in Figure 5.8. The average pore size was 954 nm.*

101

porosimeter. Mercury was forced to intrude into the measuring cell at a lower pressure and into the pores of the polymer at higher pressure. The intrusion volume of mercury was measured as a function of pressure, from which the pore size was derived. Figure 5.8 and Figure 5.9 show the SEM image and the pore size, respectively. The average pore size is 940 nm and the porosity was calculated to be 46.4%. It is worthwhile mentioning that these data can only be used as a reference, because of the difference between large scale and small scale reactions. Obviously, obtaining 0.6 g of polymer from a chip with 20 ×140 μm channels is a demanding, possibly unfeasible task.

5.3.3 Behavior of the polymer bed on our device

A polymerization reaction using solution #14 was performed for 8 min in a single channel device (Figure 5.10), and the behavior of the polymer was investigated. Several aspects will be discussed in this section. The solution was driven by EOF, with a PMT detector placed immediately before or after the polymer bed, depending on specific experimental requirements.
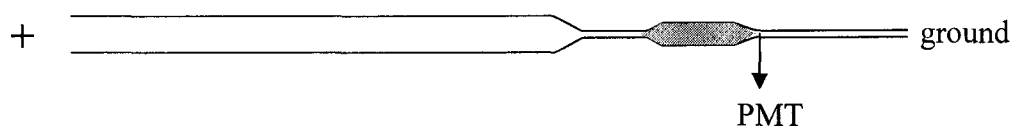
Figure 5.10 *Schematic experimental setup for the single channel device. The dimensions are described in Figure 4.2.*

5.3.3.1 Eluent composition

FITC-Avidin was used as a model protein. The eluent was prepared by changing the volume of acetonitrile (ACN) while maintaining the concentration of ammonium

102

bicarbonate (AB) at 20 mM, regardless of % ACN. The procedures are summarized in

Table 5.2.

Table 5.2 Procedures for studying eluent composition

Step	Anode reservoir	Cathode reservoir	Duration	voltage	
1	Avidin in 20 mM AB	20 mM AB	1.5 min	1.0 kV	To adsorb avidin
2	20 mM AB	20 mM AB	5.0 min	1.0 kV	To remove nonspecific adsorption
3	ACN(20-60%) + 20mM AB	ACN(20-60%) + 20mM AB		1.0 kV	To elute avidin
4	ACN(80%) + 20mM AB	ACN(80%) + 20mM AB		1.0 kV	To further elute avidin

After elution with a lower ratio of acetonitrile, 80% (v/v) ACN was used to elute

the remaining retained protein. Beds treated with 60% ACN did not release more

protein at 80% acetonitrile, but all lower ACN concentrations failed to completely elute

protein, as shown in Figure 5.11. An 80% ACN eluent could still elute some protein off

beds which were previously eluted by a lower ratio of ACN, while no more protein

came off beds eluted with 60% ACN. The current dropped drastically when introducing

the eluent containing 80% ACN into the channel. This is consistent with the result

reported by other researchers [13]. This is attributed to the decrease of conductivity and

dielectric constant by addition of ACN. Exposure of the channel surface to 80% ACN

made the EOF decrease quickly. Therefore, eluent containing 60% ACN is appropriate

for our system.

103
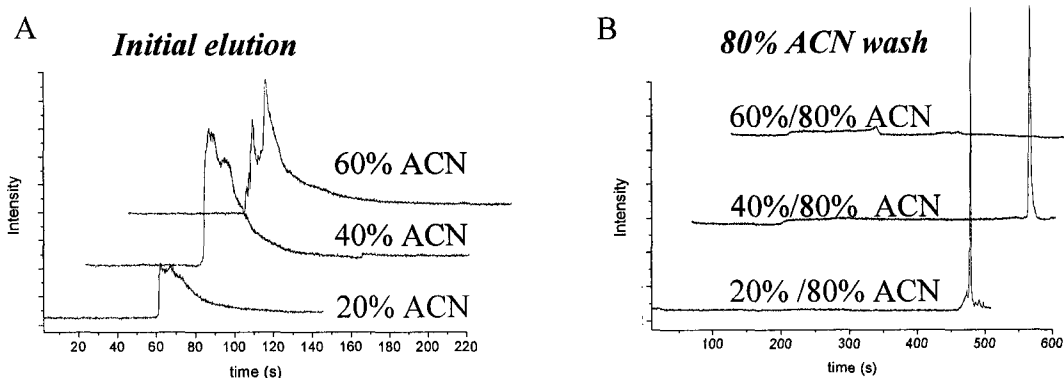
Figure 5.11 *(A) Initial elution electropherograms with different acetonitrile (ACN) ratios; (B) Further elution with 80% acetonitrile following the elution with lower ratios of ACN. The polymer beds were formed in the channel described in Figure 5.11 from the reaction of solution #14 for 8 min. Avidin solution was made by 6×10^7 times of dilution of the stock solution with 20 mM ammonium bicarbonate.*

5.3.3.2 Effect of adsorption voltage

The voltage applied during the adsorption process is important, because it will affect the flow rate and thus the amount of adsorption [2]. The procedures are listed in Table 5.3. Three adsorption voltages were studied and the elution was carried out at the same voltage. Figure 5.12 illustrates that lower adsorption voltage, thus lower flow rate, is beneficial to the adsorption. The eluted peak areas for elution voltages of 3.0 kV, 2.0 kV and 1.0 kV were estimated to be 2.04, 3.21 and 4.57 respectively.

Table 5.3 *Procedures for studying the effect of adsorption voltage*

Step	Anode reservoir	Cathode reservoir	Voltage (kV)	Duration
1	Avidin in 20 mM AB	20mM AB	1.0, 2.0, 3.0	1.5min
2	20 mM AB	20 mM AB	1.0, 2.0, 3.0	5.0 min
3	ACN(80%) + 20mM AB	ACN(80%) + 20mM AB	1.0	
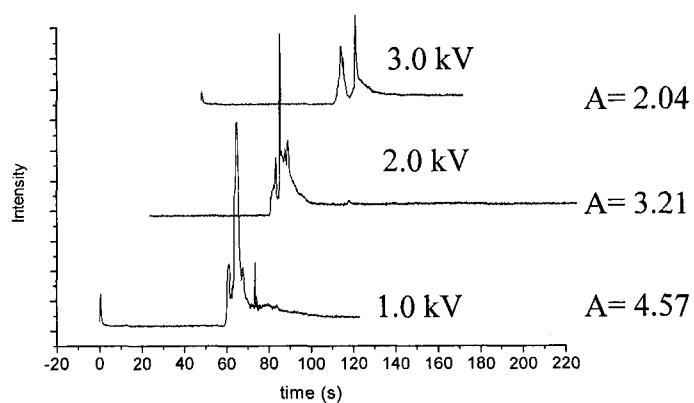
Figure 5.12 *Electropherograms for elution of proteins adsorbed at different adsorption voltages. The eluted peak areas are shown in the graph. Solution #14 was reacted for 8 min in the single devices as shown in Figure 5.4. Avidin solution was made by 6×10^7 times of dilution of the stock solution with 20 mM ammonium bicarbonate.*
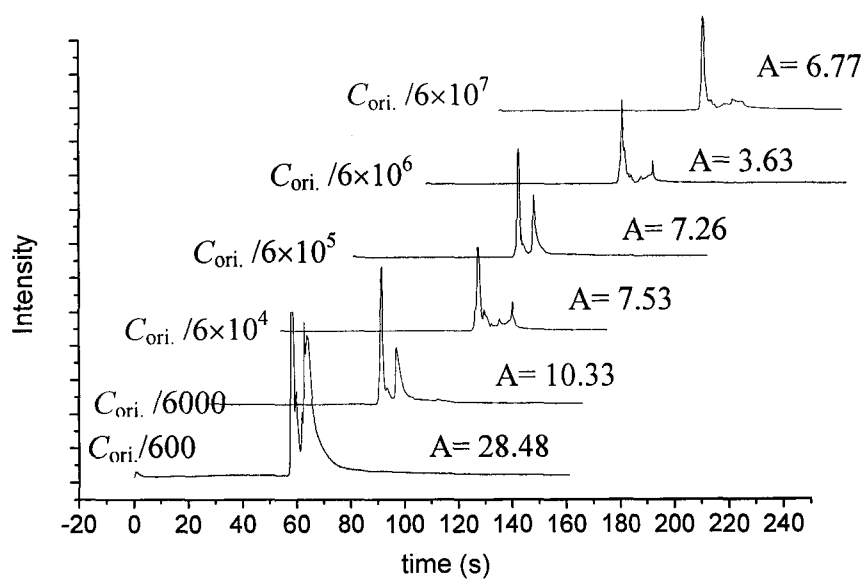
Figure 5.13 *The electropherograms for elution of proteins at various starting concentrations. c_{ori}: concentration of the original avidin stock solution. The numbers give the dilution factors from stock solution. The reaction conditions were the same as those in Figure 5.12.*

105

5.3.3.3 Effect of concentration on adsorption

FITC-Avidin solution (the concentration of stock commercial solution is unknown) was diluted different amounts with 20 mM AB. The dilution factors are given in Figure 5.13. Both the adsorption and elution were performed at 1.0 kV. In Figure 5.13, as the concentration (labeled in Figure 5.13) decreases, the amount of adsorbed avidin decreases, except for the one diluted by 60 million times. The reason is unknown. The eluted peak areas are labeled in Figure 5.13.

5.3.3.4 Estimate of concentration factor

The concentration effect is obvious when comparing Figure 5.13 with Table 5.4. Table 5.4 shows that the signal was essentially the same for all concentrations tested, when the PMT was located immediately before the polymer bed. Thus the detector could not measure the avidin at low concentrations, without preconcentration. The signal fluctuated around the baseline within a small range of standard deviation. A data trace for the highest concentration of avidin of all the concentrations tested is shown in Figure 5.14.

Table 5.4 Signals of protein solutions detected by PMT located before the polymer bed

Conc.	$c_{ori.}/3 \times 10^8$	$c_{ori.}/6 \times 10^7$	$c_{ori.}/6 \times 10^6$	$c_{ori.}/6 \times 10^5$	$c_{ori.}/6 \times 10^4$	$c_{ori.}/6 \times 10^3$	$c_{ori.}/6 \times 10^2$
signal	0.110	0.110	0.110	0.111	0.109	0.109	0.117
Std. Dev.	0.001	0.001	0.001	0.001	0.001	0.001	0.002

$c_{ori.}$: *concentration of the original FITC-Avidin stock solution*

106
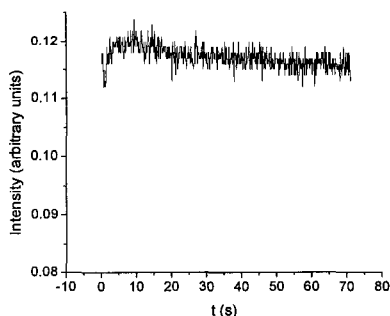
Figure 5.14 Data trace for the avidin solution measured before the polymer bed. No observable signal was detected by the detector. The avidin solution was made by diluting the stock solution by a factor of 600. Sample was driven past the detector located before the polymer bed by applying 1.0 kV.

The concentration factor can be calculated by dividing the volume of the protein solution flowing through the polymer bed in the adsorption process by the volume of acetonitrile containing buffer used in the elution process [2, 14]. The flow rates for the adsorption and elution processes were assumed to be close because they were driven by the same electric field. Hence, the concentration factor is determined by the adsorption time and the elution time. The concentration effect for BSA and avidin were evaluated. The adsorption and elution experiments were performed when 1.0 kV was applied between the anode and cathode, because a lower adsorption voltage is beneficial to the adsorption. In Figure 5.15, the electropherogram of eluted protein was fit to a Gaussian regression in order to obtain the half peak width (the peak width at half peak height) as the elution time. The concentration factors for BSA (3.3×10^{-3} mg/mL) and avidin (diluted by 6×10^7 times) were estimated to be 30 and 25, respectively.

107
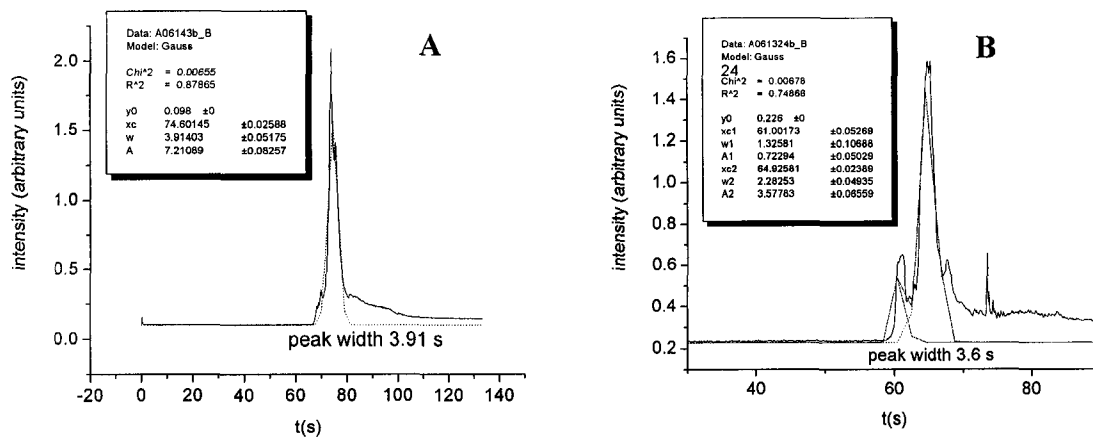
Figure 5.15 *Calculation of concentration factor*
(A) BSA was adsorbed at 1.0 kV for 2 mins, and eluted with 60% acetonitrile and 20 mM AB at 1.0 kV; (B) Avidin was adsorbed at 1.0 kV for 1.5 mins and and eluted with 80% acetonitrile and 20 mM AB at 1.0 kV. The reaction conditions were the same as those in Figure 5.12.

5.3.3.5 Flow rate change induced by polymer bed

The change in the flow rate directly influences the sample travel time in the fractionation zone, and thus the diffusion distance, which is the limiting factor in determining the sample dispersion and leakage. The effects of the polymer bed on electrical resistance and flow resistance lead to a flow rate change. The electrical resistances for the unpacked and packed single channel device were measured by filling the channel and reservoirs with a 4 M KCl solution and monitoring the current as a function of voltage. The high concentration of KCl prevents contribution by the electrical double layer. For a glass or quartz channel, the current contains two parts, the current due to transport of charge close to the double layer by EOF and the conduction current [15]. The first of these becomes negligible when the electrolyte is highly concentrated.

108

Figure 5.16 indicates that electric resistance does not change much after the monolithic packing. The small increase in the resistance for a packed channel may be attributed to the occupation of bed volume by the polymer. The estimated 46.4% porosity of the polymer means that the electrical resistance ratio of the packed over the unpacked one is expected to be 1.04, based on a pSpice simulation of the effect of volume reduction. This ratio was measured to be 1.05, based on the data in Figure 5.16. However, measurements of migration rates demonstrate the flow rate has been altered significantly as shown in Table 5.5. The migration time of the neutral marker, BODIPY, in the packed and unpacked channel was measured. The experimental setup is the same as in Figure 5.11, except the PMT detector was placed just before the polymer bed. The data in Table 5.5 show big differences in the migration time for the two devices. This can be understood by the flow conservation theory. Horváth et al developed a theory to describe the flow velocity in a CEC system [16, 17]. In our case, the EOF in the packed region is only provided by the negative charge on the channel wall, because the polymer has no charge. Moreover, some regions of the channel wall, being in close contact with the polymer, cannot be fully charged. All of these factors result in a smaller EOF and thus slower flow through the bed region. According to Horváth's model, which consists of a packed segment upstream and open segment downstream, the volume flow rate in the unpacked segment will slow down in order to abide by the mass conservation law.

109

$I_A = -40.79133 + 2.96611 V_A$

$I_B = -38.96333 + 2.82343 V_B$

A (unpacked)

B (packed)

current (μA): 350, 300, 250, 200, 150, 100, 50, 0, -50

voltage (V): 0, 20, 40, 60, 80, 100, 120, 140
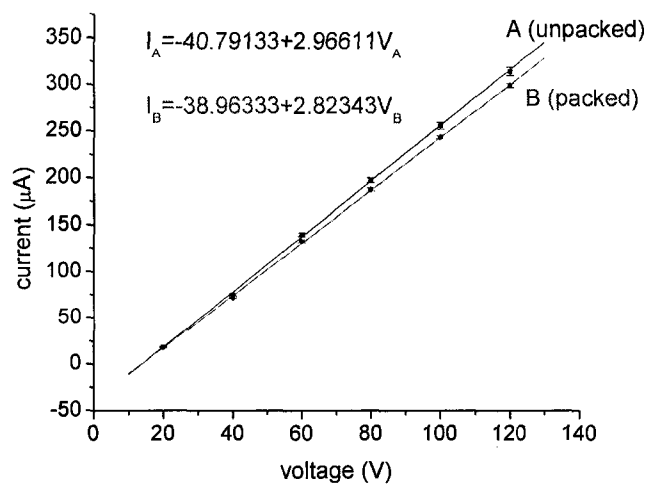
Figure 5.16 *Current as a function of voltage for unpacked and packed channel. The reaction conditions were the same as those in Figure 5.12. The channel was filled with 4 M KCl solution.*

Table 5.5 *Measurement of migration time for packed and unpacked channel*

Voltage (kV)	Migration time (unpacked) (s)	Migration time (packed) (s)
0.5	52.3	351.4
0.6	41.6	264.4
0.7	34.9	230.4
0.8	28.3	193.7
0.9	26.9	181.2
1.0	24.3	161.7
1.1	23.5	146.6
1.2	20.3	129.6
1.3		117.0
1.4		112.5
1.5		99.0

5.3.4 Polymerization in the multiplexed fractionator

The polymer beds were prepared in 36 bed regions using solution #14. First, the 10th reservoir on one side was filled with 20 μL of a monomer and porogen mixture. The mixture was then delivered into the other channels by capillary force. Once the 8th and 12th channels on the same side as the initial 10th reservoir were filled, the mixture

110

was added to the reservoirs of those two channels as well, to enhance the flow rate to other channels. The chip was left in the dark for around 40 mins, until all the other channels were filled. Afterwards, all the reservoirs were loaded with 20 µL of water and sealed with parafilm. Care was taken to align the chip with the mask before exposing it for 8 min under the UV lamp. To rinse the chip, a vacuum line was attached to three outlets. One was connected to the sample reservoir, while the other two were connected to two collection reservoirs for 10 min before moving to the next two reservoirs. The chip was rinsed with methanol/water (50%:50%, v/v) for 3 h, followed by water for another 3 h, then finally conditioned with 10 mM NaOH, for 3 h. The polymer bed cannot withstand 0.1 M NaOH due to the formation of bubbles.
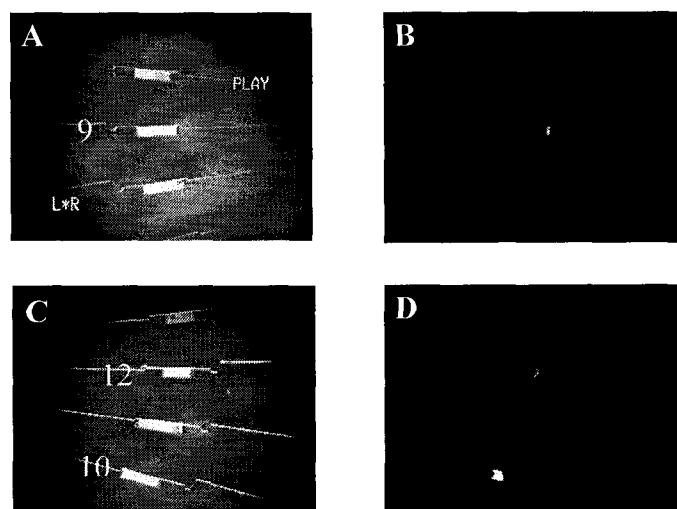
Figure 5.17 Images of the polymer beds before and after protein adsorption. The sample reservoir and sheath reservoirs were held at 1.5 kV and 1.8 kV, respectively. Figure 5.17 A shows the collection channels from 8th to 10th with packed polymer beds on the left side. Figure 5.17 B shows the fluorescence image of avidin adsorbed onto the polymer bed in the 9th channel. Figure 5.17 C shows the collection channels from 10th to 13th with packed polymer beds on the right side. Figure 5.17 D shows the fluorescence image of avidin adsorbed onto the polymer beds in the 10th and 12th channel. The polymer beds in unlabeled collection channels did not fluoresce because avidin was not adsorbed onto those beds.

111

5.3.4.1 Protein concentration on the multiplex fractionator

FITC-Avidin (diluted with 20 mM ammonium bicarbonate by a factor of 300 from the stock solution) was used as a model protein. The sample reservoir and sheath reservoirs were held at 1.5 kV and 1.8 kV, respectively. The 2nd, 9th, and 15th channels on the left side and 5th, 10th, 12th channels on the right side were grounded sequentially for 4 min each. Images in Figure 5.17 show that the protein only adsorbed onto the front end of the column. This can be attributed to the extremely low flow rate in the packed segment, which is beneficial for protein adsorption, as studied in 5.3.3.2.

5.3.4.2 Disturbance of flow direction by the polymer bed

BSA (1 mg/mL in water) was employed as the model protein. The sample and sheath reservoirs were held at 0.8 kV and 1.22 kV, respectively. Figure 5.18 shows the distortion of flow direction with polymer beds in the chip. On this device, the 16th channel on the left side happened to have no polymer formed. The nicely focused sample stream in Figure 5.18A verified the efficiency of the voltage combination employed. However, as demonstrated in Figure 5.18B, besides flowing into the grounded channel, the sample stream also flowed downstream and contaminated the inlets of other channels. This can be explained from the discussion in Section 5.3.3.5. Because the flow rate in the open segment was much higher than that in the packed segment, the volume flow rate of the sample stream delivered from the open fractionation zone was not compatible with the flow rate through the packed segment. As a result, a large amount of sample accumulated in the fractionation zone based on the mass conservation law. This phenomenon was even worse when the 4th channel on

112

the left side was grounded. Figure 5.18C shows no observable flow into this channel. However, the sample accumulated in the fractionation zone barely reached any of the polymer beds in the floating channels because no additional driving force existed. That explains why Figure 5.17 shows no contamination to the polymer beds of the floating channels, despite the volume flow rate mismatch.
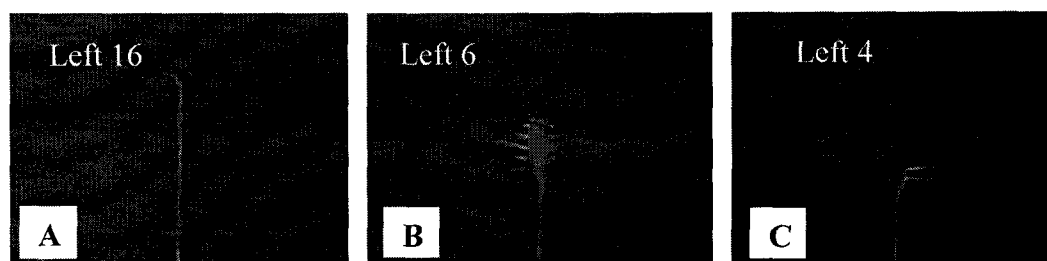
Figure 5.18 Images show the distortion of the flow direction by the polymer beds. The sample and sheath reservoirs were held at 0.8 kV and 1.22 kV, respectively.

5.3.5 Improvement

The problem discussed above might be solved in several ways; increasing the EOF by making a charged polymer bed, or reducing the flow resistance by shortening the polymer bed, making a polymer bed with larger pores, or enlarging the cross section of the bed region.

5.3.5.1 EOF enhancement

AMPS was introduced to the reaction mixture because it can be negatively charged. Solution #18, 22 and 26 with increasing amount of AMPS were used to prepare the polymer bed after reaction times of 6 min, 14 min and 18 min, respectively. The migration time was measured to be 122 s, 86 s and 67 s. In contrast, the migration time

113

in a channel packed with polymer without AMPS was 161.7 s, as shown in Table 5.5.

Solution #26 was selected to make the polymer beds on the multiplex fractionator. The images shown in Figure 5.19 indicate that the distortion of flow has been alleviated to some extent when compared to Figure 5.18 C; however, as the sample stream flowed into the channels at ground, it also leaked into the channels downstream due to the disturbance of flow by the polymer beds.
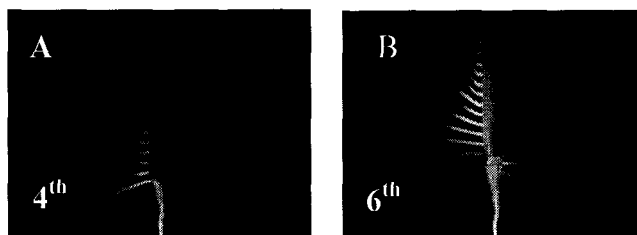
Figure 5.19 *Images show sheath images in the multiplexed fractionator with charged polymer beds formed from solution #26. Images show EOF was enhanced a little when compared to Figure 5.18 B and C because sample stream could be delivered into the collection channel at ground. The sample and sheath reservoirs were given 1.4k and 1.8kV respectively. Solution #26 was reacted in the multiplexed fractionator for 16 mins. Figure 5.19 A shows leakage into the channels downstream even though sample had not yet been delivered to any downstream channels. Figure 5.19 B shows obvious flow along the fractionation zone and leakage into the channels downstream. Sample is 200 µM fluorescein in 20 mM ammonium bicarbonate.*

5.3.5.2 Shorter bed

The edge resolution of the polymer bed is defined by [7],

$$b_{min} = \frac{3}{2}\sqrt{\lambda(s + z/2)}$$

where b_{min} is the resolution limit, λ is the illuminating wavelength, s and z are the distance between mask and polymer surface and polymer thickness, respectively. In our case, λ is 312 nm, s is 457 µm which is the thickness of the bottom glass (O211) and z is 20 µm. b_{min} was calculated to be 18 µm. Based on this, a bed length of ~36 µm could be made. However, we find the polymer bed produced is never shorter than 200 µm,

114

even though a very narrow window was used with a cooling fan to reduce thermal polymerization. Throckmorton *et al* also reported the same phenomenon [7]. As a result, the use of shorter beds to reduce flow resistance was not explored.

5.3.5.3 Making larger pores

It was reported that when methanol was used as the porogen, the pore size could be as large as 19 μm, whereas when methanol and hexane were used together, the pore size achieved was 9 μm [3]. Considering the channel is 20 μm deep, it is impossible to form pores of 19 μm. We tried various conditions using methanol and hexane as porogens. However, no particles formed in the bed region of our device, even when the light from the transilluminator exposed the chip through a 1 mm window. In contrast, the reaction happened easily when octanol was the porogen. We speculate that the failure of formation of a polymer bed on our device when methanol and hexane were the porogens can be attributed to three reasons. First, the exposure window was not long enough. When the exposure window size was increased to 2 mm, the reaction easily occurred on our device. Second, the UV light from the UV transilluminator was not intense enough and not well collimated. The reaction occurred nicely in 5 min with a 0.5 mm exposure window when exposed to well collimated UV light from a mask aligner. Finally, the width and depth of our device are too small for the reaction to happen. To investigate these factors, a channel with different dimensions (800 μm wide and 150 μm deep) than our device was used. The polymerization reactions for solution #27, 28, 29 and 30 were found to occur easily in 5 min even when the exposure window was as narrow as 200 μm. However, the interface of the polymer bed was not clearly

115

defined. We find that the polymer bed formed in the large channel (800 μm wide and 150 μm deep) using solution #27, 28, 29 and 30, after 5 min of exposure to the UV transilluminator, had low flow resistance, and the flow resistance increased with reaction time because the polymer structure became denser.

5.3.5.4 Making larger bed

A larger bed brings the advantage of short reaction time, which gives a sparse structure compared to a longer reaction time, so it is possible to lower flow resistance with a larger cross section. In order to enlarge the bed volume, we fabricated the bed in the cover plate. Two cover plates with beds of different depths were fabricated and bonded to two substrates.

Device 1: All the access holes were drilled on a cover plate with 43 μm deep beds. Solution #27 was used to study the polymerization reaction on the new device. The reaction rate was found to depend on the direction of the illuminating UV light. Mask **C** was placed underneath the chip. The reaction still could not be initiated when the UV light was exposed from the substrate side, as discussed in 5.3.5.3. However, when the chip was turned over so that the UV light illuminated from the cover plate side that contains the bed regions, the reaction happened easily. When this polymer was transferred onto the multiplexed fractionator, the flow resistance coming from the polymer bed still affected the flow direction. Similar results to those shown in Figure 5.18 were observed.

Device 2: Since the exposure from the deeper bed side can shorten the reaction time, on the second cover plate, the bed was enlarged to 115 μm deep. All the access holes were

116

drilled onto the substrate instead of onto the cover plate. The cover plate was actually placed underneath, which allowed the light to illuminate from the cover plate side. Solution #26 was reacted for 6.5 min and the migration time was measured to be 37 s, whereas the migration time was 67 s for the shallower bed (20 μm) described in 5.3.5.1, which means the flow resistance was reduced in **Device 2**. The bed capacity in **Device 2** was 0.0657 mmoles/L when trypsin inhibitor was used as the model protein.
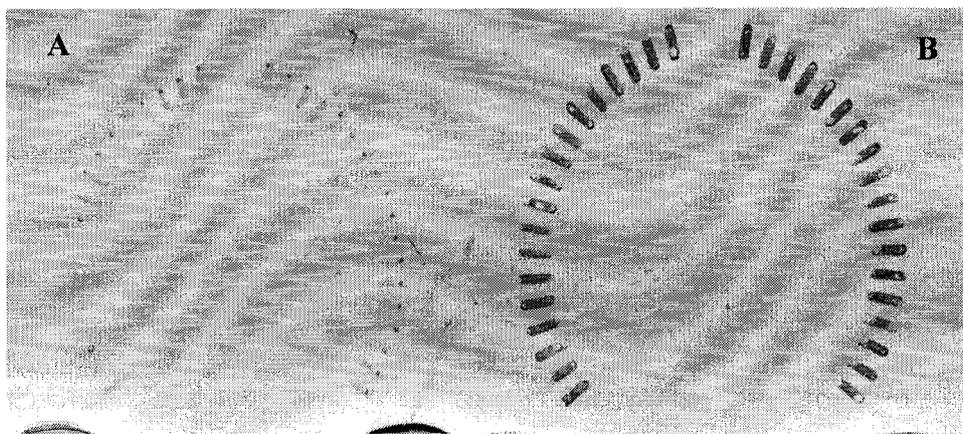
Figure 5.20 Images of the polymer beds formed from solution #26. Image in Figure 5.19 A was taken after solution #26 was reacted for 5 min. Then, the chip was flushed with methanol and water. The polymer beds became observable as shown in Figure 5.20 B. The black spots in image A are bubbles induced by the dead volume of the bed due to the size difference of the original bed in one glass plate and the deeper bed in the other plate.

5.3.5.5 The sheath effect on the fractionator with deeper beds (113 μm deep)

Solution #26 was used to prepare the polymer beds after reacting for 5 min. As shown in Figure 5.20, the polymer beds were blurred after the reaction and became clear after rinsing with methanol and water. Figure 5.21 shows a tightly pinched fluorescein stream, when the sample and sheath reservoirs were held at 1.5 kV and 1.95 kV, respectively. Figure 5.22 shows the automatic switching process, from the 14th to the 18th channel. These experiments indicated that the flow disturbance by the formation

117
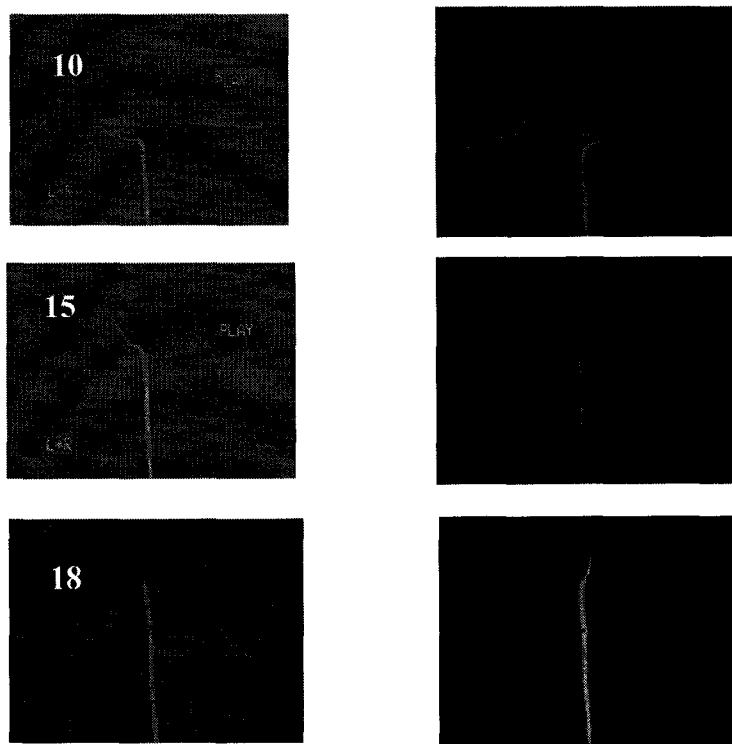
Figure 5.21 Images of the focused fluorescein streams on the fractionator with polymers. The sample and sheath reservoirs were held at 1.5 kV and 1.95 kV, repectively. The fractionator with polymer beds as shown in Figure 5.20 was used.
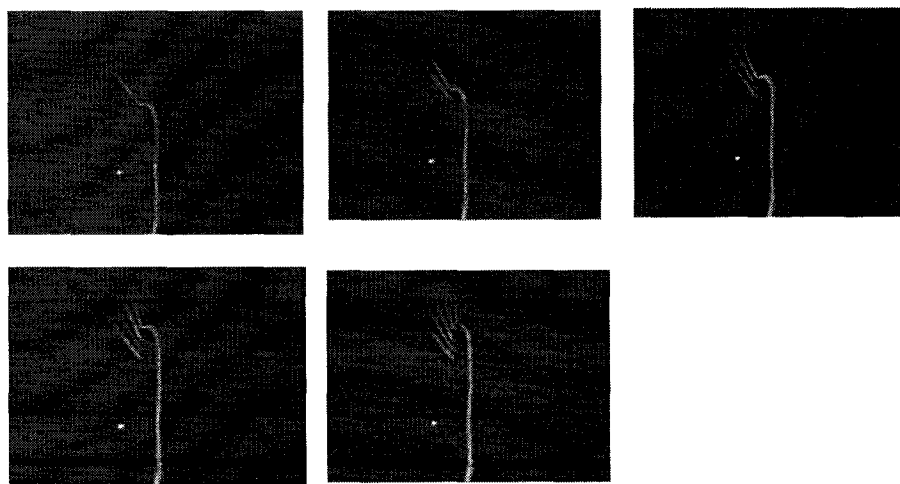
Figure 5.22 Images show the automatic switching of the BSA stream from 14th channel to 18th channel. The sample and sheath reservoirs were held at 1.5 kV and 1.95 kV, repectively. The same device as that in Figure 5.21 was used.

118

of polymer beds in shallower bed regions (20 μm) were solved by enlarging the bed

regions to 115 μm and by shortening the reaction time to 5 min.
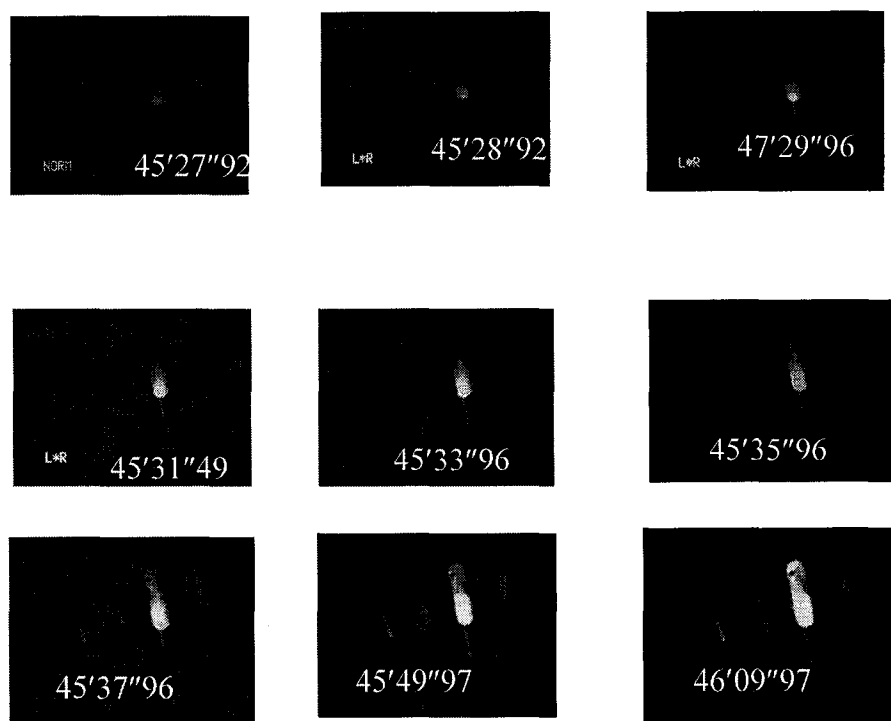
Figure 5.23 Dynamic protein adsorption process onto the 5th bed on the left side. BSA (1 mg/mL) was driven to the polymer bed and adsorbed. Other conditions were the same to those in Figure 5.21.

5.3.5.6 Protein adsorption on the multiplex fractionator

Since the sheath flow effect could be made to function normally on the fractionator with polymer beds, we then studied a dynamic protein adsorption process onto a specific polymer bed under protection from sheath streams, which is the final aim of this fractionator. The protein stream was supposed to be adsorbed onto the specific bed without leakage into other beds. In order to observe the leakage that may exist, a highly concentrated BSA solution (1mg/mL) was used. Images in Figure 5.23 show the adsorption process of BSA onto the 5th bed on the left side. The lack of an observable

119

fluorescence signal for the channel downstream of the bed means that no protein leaked through the space before the front of the protein band reached the end of the polymer bed. The bed glared brightly as the protein was adsorbed onto it, lightening up the two beds on either side. The laser spot covered the entire bed region of the channel of interest and the upstream channel segments of the two channels beside it. The channels upstream of the two beds did not fluoresce, excluding the possibility of adsorbed protein from leakage into the other beds. A recipe for forming larger pores was not investigated further, because larger pores reduce the surface to volume ratio and thus the amount of adsorption.

5.3.5.7 Study of voltage combination

Because this fractionator will eventually be coupled with protein separation, in order to be flexible with applied voltages in the separation process, it is necessary to find all the possible voltage combinations which are able to produce neat sheath effects. We find that the sheath flow effect was efficient when the sample voltage varied from 1.1 to 1.5 kV while keeping the sheath voltage at 1.8 kV. However, bubbles usually occur in these devices after running longer than 10 min in this voltage range. Sometimes, the separation in the sample channel needs to last longer. Reducing the voltages could prevent the bubbles. However, the velocity decreased at the same time and thus the diffusion of the sample stream became more severe. Table 5.6 lists the allowable voltage combinations tested experimentally without severe diffusion problems.

Table 5.6 The allowable voltage combination for creating pinching effect

sample	1.1	1.1	0.8	0.7	0.8	0.9	0.9
sheath	1.5	1.4	0.92	1.0	1.0	1.0	1.1

5.4 Conclusions

Polymer beds were coupled with the fractionator in order to adsorb protein for further analysis. At first, the polymer beds were found to affect the flow direction severely and thus the sheath effect was not working on the fractionator with polymer beds. The recipes for making monolithic polymer and the bed dimensions were improved several times. Finally, we find that solution #26 is a good choice to form polymer beds on the multiplexed fractionator with 115 μm deep beds. The solution was reacted for 5 min with the illumination of UV light (312 nm) through the photomask (0.5 mm window size) from the side of the glass plate with the 115 μm deep beds. The final conditions allow the sheath flow effect and protein adsorption on this fractionator with polymer beds to be performed well. This fractionator will be coupled to protein separation stages in the future.

5.5 Reference

1. Taylor, J.; Harrison, D.J. *Procceedings of MiroTAS 2002*, 344-346.
2. Yu, C.; Davey, M.H.; Svec, F.; Fréchet, J.M.J. *Anal. Chem.* **2001**, 73, 5088-5096.
3. Yu, C.; Xu, M.C.; Svec, F.; Fréchet, J.M.J. *J. Polym. Sci. Part A: Polym. Chem.* **2002**, 40, 755-769.
4. Yu, C.; Svec, F.; Fréchet, J.M.J. *Electrophoresis*, **2000**, 21, 120-127.

121

5. Chuda, K.; Jasik, J.; Carlier, J.; Tabourier, P.; Druon, C.; Coqueret, X. *Radiation Physics and Chemistry* **2006**, 75, 26-33.

6. Lin, Z.; Xie, Z.H.; Lu, H.X.; Lin, X.C.; Wu, X.P.; Chen, G.N. *Anal. Chem.* **2006**, 78, 5322-5328.

7. Throckmorton, D.J.; Shepodd, T.J.; Singh, A.K. *Anal. Chem.* **2002**, 74, 784-789.

8. Rohr, T.; Hilder, E.F.; Donovan, J.J.; Svec, F.; Fréchet, J. M. J. *Macromolecules* **2003**, 36, 1677-1684.

9. Peterson, D.S.; Rohr, T.; Svec, F.; Fréchet, J.M.J. *Anal. Chem.* **2003**, 75, 5328-5335.

10. Peters, E.C.; Petro, M.; Svec, F.; Fréchet, J.M.J. *Anal. Chem.* **1997**, 69, 3646-3649.

11. Viklund, C.; Pontén, E.; Glad, B.; Irgum, K. *Chem. Mater.* **1997**, 9, 463-471.

12. Kanamori, K.; Yonezawa, H.; Nakanish, K.; Hirao, K.; Jinnai, H. *J. Sep. Sci.* **2004**, 27, 874-886

13. van den Bosch, S.E.; Heemstra, S.; Kraak, J.C.; Poppe, H. *J. Chromatogr. A* **1996**, 755, 165-177

14. Oleschuk, R.D.; Shultz-Lockyear, L.L.; Ning, Y.B.; Harrison, D.J. *Anal. Chem.* **2000**, 72, 585-590.

15. Rice, C.L.; Whitehead, R. *J. Phys. Chem.* **1965**, 69, 4017-4024.

16. Rathore, A.S.; Horváth, Cs. *Anal. Chem.* **1998**, 70, 3069-3077.

17. Rathore, A.S. *Electrophoresis* **2002**, 23, 3827-3846.

6.1 Introduction

In this chapter, we evaluate methods to perform protein separations coupled with the sheath flow effect. The CZE mode demonstrated earlier is a good choice from the perspective of being compatible with the fractionator, as demonstrated in Chapter 3. However, CZE is not as powerful as other protein separation methods. Isoelectric focusing (IEF) is an excellent protein separation and concentration tool [1] that has been extensively used. IEF on a microchip was first presented by Hofmann *et al* [2] on a glass chip, followed by a demonstration on quartz by Mao [3] and on PDMS chip by Cui [4]. IEF is categorized into two-step and one-step IEF. In two-step IEF, the protein is focused into individual zones according to their pI values, followed by mobilization out of the capillary or channel by gravity [5], chemical mobilization [6] or hydrodynamic force [7]. Focusing and mobilization are carried out at the same time [8,9] in one-step IEF.

In our design, if two-step IEF in the sample channel is performed first, the already focused protein zones would be deformed in the mobilization and fractionation step because of changes in the electric field and zeta potentials along the channels. Hence, we chose to perform one-step focusing, mobilization and focusing at the same time. The challenges with this method are: (a) One-step IEF is not as stable as two-step IEF because of the disturbance of focusing by the mobilization force, normally EOF, in the sample channel. EOF is not uniform across the entire channel because of the pH gradient and the adsorption of ampholyte onto the channel surface.

In our case, coating all the channel surfaces to reduce EOF is not feasible, because strong EOF is necessary to drive the sample stream across the fractionation zone at high

speed, in order to restrict diffusion. Selectively coating the sample channel is not recommended either, due to the pressure differential associated with having multiple different zeta potentials along the channel of a device. Further, the voltage combination that creates good sheath flow effect may be inappropriate for IEF. In this chapter, we explore the feasibility of coupling the one-step IEF and fractionation processes together.

6.2 Experimental

Reagents

Bio-lyte (pH 3-10) was obtained from Bio-RAD. Enhanced cyan fluorescent protein (ECFP) and monomeric red fluorescent protein (mRFP) was kindly donated by Zihao Cheng and Huiwang Ai from Dr. Campell's group in Department of Chemistry, University of Alberta. BSA from Sigma (Oakville, Ontario, Canada) was labeled using an Alexa Fluor 488 Microscale Protein Labeling kit from Invitrogen (Burlington, Ontario, Canada). The final concentration was 45 μM. Alexa Fluor 488 labeled trypsin inhibitor and FITC-insulin were from Invitrogen. The concentrations of the stock solutions of trypsin inhibitor and insulin were 1mg/mL in water. FITC-IgG was from Sigma. The isoelectric points (pI) of proteins are listed in Table 6.1.

Table 6.1 Isoelectric points of proteins

Protein	ECFP	BSA	Insulin	Trypsin inhibitor	IgG
pI	5.95^a	4.8^b	5.5^c	4.6^d	7.4^e

a: This value was calculated based on the gene sequence of ECFP.
b: http://faculty.washington.edu/yagerp/microfluidicstutorial/transverseief/transverseief.htm
c: Eriksson, H. *Biotechnology Techniques* **1998**, 12, 329-334.
d: http://www.sigmaaldrich.com
e: Fujita, H.; Narita, T.; Ito, S. *Diabetes Care* **1999**, 22, 823-826.

Microchip operation

The experiments were operated on the fractionators described in previous chapters and one more which will be introduced in this chapter. The chips were conditioned with 0.1 M NaOH, followed by rinsing with water and catholyte in sequence. All the channels and reservoirs except the sample and buffer reservoir were filled with catholyte. Anolyte was loaded into the buffer reservoir. After sample injection, positive voltage was applied between the buffer reservoir and one of the collection reservoirs, to drive focused sample zone past the detector located at the converging point of the sample and sheath channels, which is called the sheath point. The two sheath reservoirs received voltages higher than that on the buffer reservoir. After separation and fractionation were performed, the device was regenerated. Anolyte was then removed from the buffer reservoir and it was filled with catholyte. The same voltage combination as that used in the focusing process was then employed to mobilize catholyte, destroying the pH gradient formed in the focusing process and regenerating the channel surface.

6.3 Results and Discussion

6.3.1 Effect of the length of IEF channels

To study the effect of IEF channel length, the second generation of Chapter 2 (Figure 2.10 and Table 2.4) Design **B** and a third generation design shown in Figure 6.1 b and Table 6.1 were used to perform IEF. A PMT was located at the sheath point. Figure 6.2 demonstrates the IEF results on the second and third generation devices. For the second generation, which has a long separation channel, in most cases no peak was

125
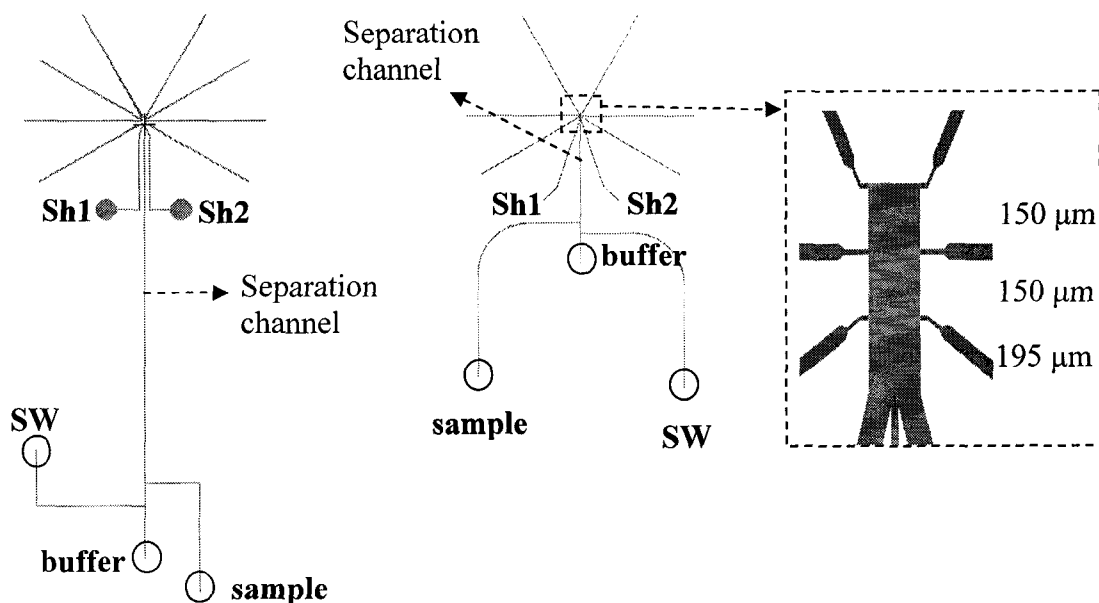
(a) Design B from Chapter 2, 2ⁿᵈ generation

**(b) Design B, 3ʳᵈ generation)**

Figure 6.1 The layouts of fractionators with long and short separation channels. Figure 6.1 a shows the Design B from Chapter 2 which has a 4 cm long separation channel. The injection plug is 2 mm long and the distance from buffer reservoir to the injection plug is 5 mm. Figure 6.1 b shows the design in the third generation which has a 1.6 cm long separation channel. The injection plug is 2 mm long and the distance from buffer reservoir to the injection plug is 4 mm.

Table 6.2 The detailed dimension of Design B in the 3ʳᵈ generation

Fractionation zone	Sheath channel	Collection channel		Separation channel
		Segment A*	Segment B*	$w = 50$ µm $l = 16$ mm
$w = 166$ µm $l = 500$ µm	$w = 78$ µm $l = 10$ mm	$w = 10$ µm $l = 100$ µm	$w = 36$ µm $l = 10$ mm	
$R = 0.224$	$R = 23.30$	$R = 7.539$		$R = 55.32$

* Collection channel contains two segments, A and B, with different dimensions.

obtained, as shown by the electropherogram in Figure 6.2 a. In contrast, for the third generation, which has a short separation channel, the peak shown in Figure 6.2 b always appeared.
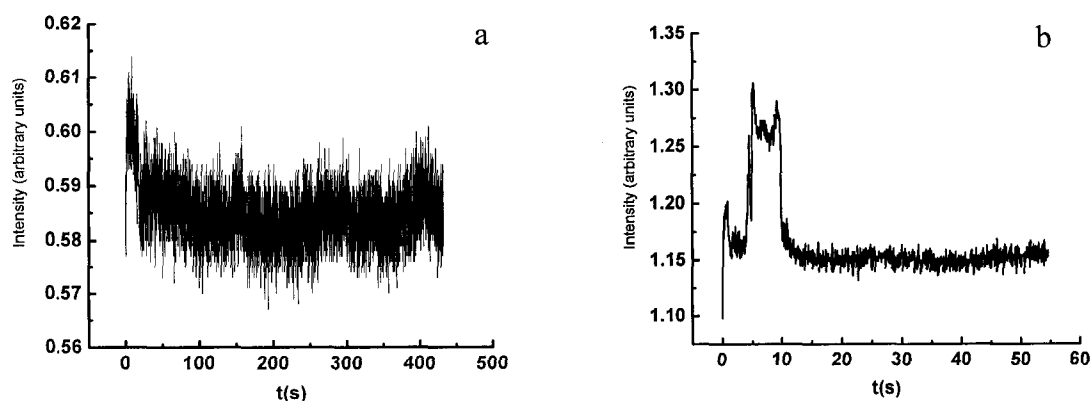
Figure 6.2 *The electropherograms obtained during the focusing process for the fractionators with long (a) and short (b) separation channels shown in Figure 6.1. Anolyte: 10 mM H_3PO_4; Catholyte: 10 mM NaOH; Sample: IgG 0.01 mg/mL in water with 2% ampholyte; Injection: -2.5 kV for 60 s. Focusing: (a) Sh1 and Sh2 were at 2.0 kV, the buffer reservoir was at 0 kV and the collection channel was at -3.0 kV; (b) Sh1 and Sh2 were at 1.0 kV, the buffer reservoir was at 0 kV and the collection channel was at -2.0 kV.*

The lack of peaks in the long channel versus short channel device is surprising. In both designs, once the buffer reservoir was filled with catholyte for device regeneration, a large protein peak was observed, as shown in Figure 6.3. This suggests that protein precipitation occurred during the IEF step. This may be partially explained by the different electric fields in separation channels induced by different separation channel lengths. The electric fields were calculated to be 143 V/cm and 461 V/cm for the long and short separation channels, respectively. Therefore, the sample plug will take 54 s and 5s respectively to reach the sheath point. In the longer separation channel, there is

127

time for almost full precipitation, and in shorter separation channel, fraction is not fully focused and so remains in solution and is seen at the detector. The fluctuated migration times of these eluted peaks can be understood from the non-uniform EOF resulted from protein adsorption.
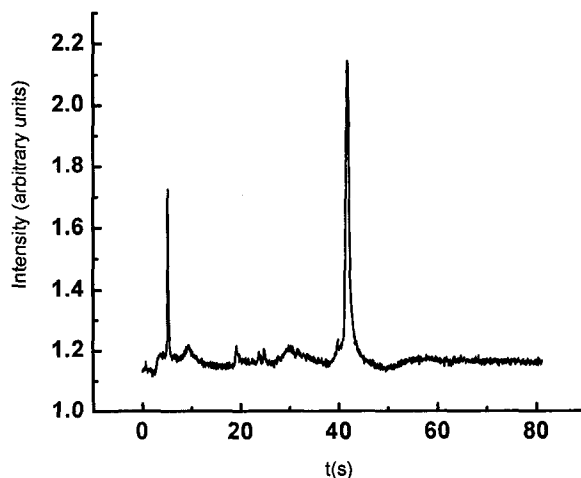

Figure 6.3 *Electropherogram following the IEF process shown in Figure 6.2b. The voltages applied were the same to those of the focusing process in Figure 6.2b. The anolyte in buffer reservoir was replaced with catholyte. The protein left in the channel due to lost of charge was charged again and driven past the detector. So, the channel surface was regenerated.*

6.3.2 Solutions to protein precipitation and adsorption

Protein precipitation in IEF is a notorious problem. Adding urea to the sample solution [10] can mitigate this problem, because urea denatures proteins and may reduce precipitation. Protein adsorption onto bare glass surface is another problem in IEF. The protein adsorption can be reduced by dynamic coating with HPMC or MC [11] because the addition of HPMC or MC can reduce surface charges and adsorption sites. In these chips, HPMC, glycerol and urea were found to improve the situation to some extent. HPMC was added to the catholyte and sample for all the following experiments.

128
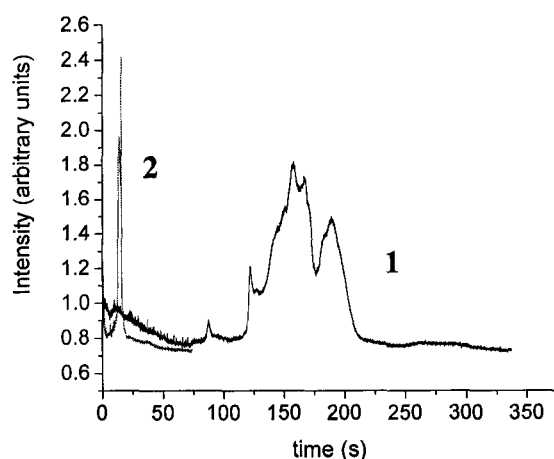
Figure 6.4 Electropherograms of IEF processes at different focusing voltages for a single protein. Anolyte: 100 mM formic acid; Catholyte: 20 mM NaOH containing 0.06% HPMC; Sample: 25 μL of IgG (1.25 μg/mL) in 20 mM ammonium bicarbonate containing 2% ampholyte mixed with 75 μL of glycerol; Injection: -1.5 kV for 5 s; Buffer reservoir was at ground; Sh1 and Sh2 were floating; Collection reservoir was at -1.0 kV for trace 1 and -2.5 kV for trace 2, respectively.
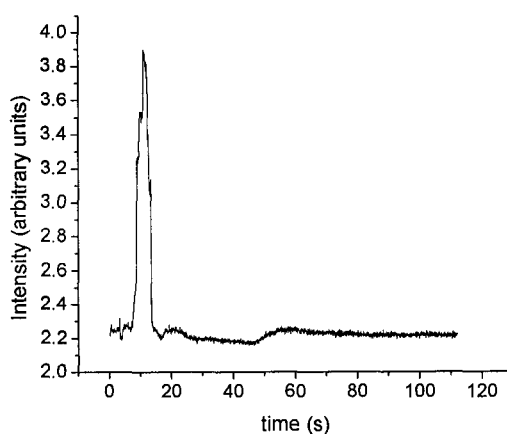
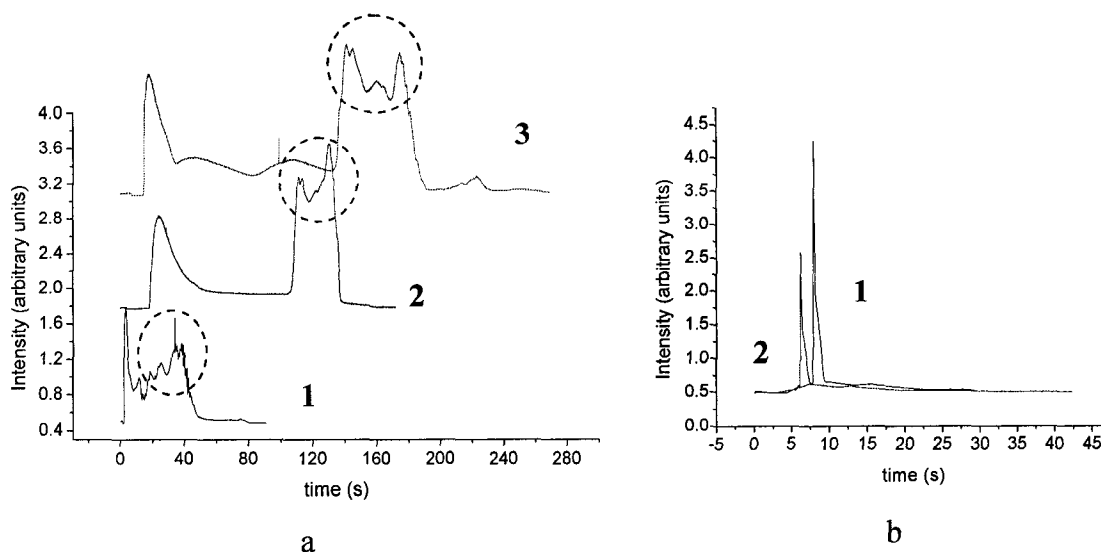**Figure 6.5** Electropherogram of IEF process of a mixture. Anolyte and catholyte are the same to those in Figure 6.4. Sample: 25 μL of mixture of IgG (1.25 μg/mL) and BSA (20 μg/mL) in 20 mM ammonium bicarbonate containing 2% ampholyte mixed with 75 μL of glycerol ; Injection: -1.0 kV for 20 s; Buffer reservoir was at ground; Sh1 and Sh2 were floating; Collection reservoir was at -2.5 kV.

129

6.3.2.1 Effect of glycerol

The third generation device shown in Figure 2.1 b was used. When a high concentration of glycerol was mixed with an IgG sample, almost all the protein could be driven by a lower voltage (1.0 kV) past the detector during the focusing process, as shown by trace 1 in Figure 6.4. No glycerol was added to the buffer. However, multiple broad peaks showed up for a single protein sample. Trace 2 in Figure 6.4 demonstrates the narrower peak at higher focusing voltage (2.5 kV). The IEF results of a mixture of IgG and BSA are shown in Figure 6.5. The appearance of only one large peak illustrates no separation for the two proteins. Therefore, we conclude that a high concentration of glycerol should be avoided.

6.3.2.2 Effect of urea

In another attempt to improve IEF separation, 4M urea was introduced only into the sample matrix. Trace 1 and 2 in Figure 6.6 a show IEF processes at high and low voltages, respectively. A lower focusing voltage and thus weaker EOF allowed longer times for protein molecules to be focused. As a result, less amount of protein was left behind in the separation channel as shown by trace 2 in Figure 6.6 b. The broad focused peaks shown by trace 3 in Figure 6.6 a illustrated that 100 mM formic acid is not as good an anolyte as 10 mM H_3PO_4. This can be explained by the sharper pH gradient created by 10 mM H_3PO_4 due to its stronger acidity. Figure 6.7 shows that a higher concentration of HPMC (trace 2) leads to longer migration time and slightly better resolution. However, 0.22% HPMC was found to reduce EOF considerably after a few runs.
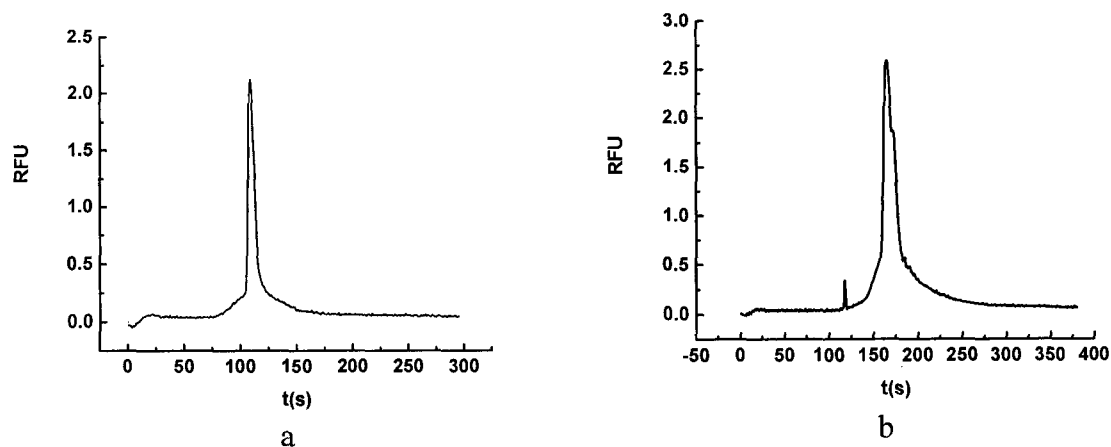
Figure 6.6 (a) Electropherograms of IEF processes. The circled peaks were from the mobilization of focused protein. **Trace 1 and 2**: Anolyte: 10 mM H_3PO_4; Catholyte: 20 mM NaOH containing 0.06% HPMC; Sample: insulin (0.5 μg/mL) in the mixture of 4M urea, 0.1% HPMC and 3% ampholyte; Buffer reservoir was at ground; Collection reservoir was at -2.5 kV for **trace 1** and -0.5 kV for **trace 2**. **Trace 3**: The conditions were the same as those of **trace 2** except 100 mM formic acid was used as anolyte. (b) Electropherograms of protein eluted during the surface regenerating processes following the IEF processes shown by **trace 1** and 2, respectively.
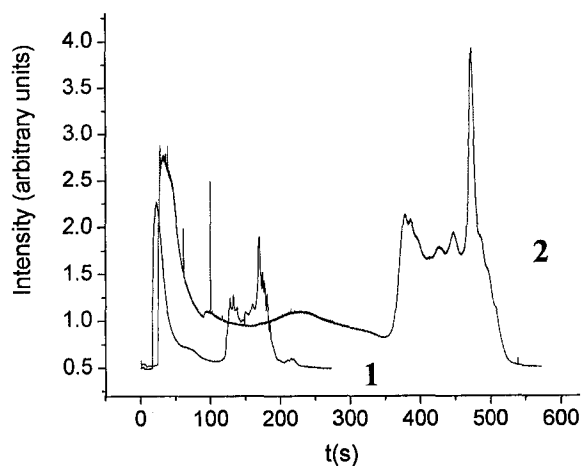
**Figure 6.7** Electropherograms of IEF processes. Anolyte: 10 mM H_3PO_4; Catholyte: 20 mM NaOH containing 0.06% HPMC and 0.22% HPMC for **trace** 1 and 2, respectively; Sample: mixture of insulin (0.25 μg/mL) and BSA(0.0225 uM) in the mixture of 4M urea, 0.1% HPMC and 3% ampholyte; Injection: -1.0 kV for 4 s; Buffer reservoir was at ground; Collection reservoir was at -0.5 kV; Sh1 and Sh2 were floating.

131

Although a large portion of the protein molecules were focused and mobilized past the detector, there was always a large peak at the very beginning. This peak cannot be completely attributed to the strong EOF, because further reducing EOF by adding more HPMC to the buffer did not remove it. To identify the origin of this peak, similar experiments were performed in a capillary. The results in Figure 6.8 showed no peaks at the beginning of the focusing process. For a capillary, the sample plug at the buffer reservoir end directly contacts the anolyte. In comparison, on a microchip with the double T junction design, the catholyte was actually sandwiched between the sample plug and the anolyte in the anodic reservoir, as shown in Figure 6.9 a. Therefore, during the first stage of focusing, ampholyte in the sample matrix could not form a pH gradient, because there was no pH difference across the sample plug. We conclude that a CZE mode, or perhaps a sample stacking effect, resulted in the first peak. As H^+ from the anolyte entered into the channel, the sandwiched catholyte was first neutralized, then became acidic, and the ampholyte began to form a pH gradient. However, the pH gradient was not well defined, so that insulin and BSA could not be separated. In order to get rid of the catholyte sandwich, we moved the access holes to new positions, shown in Figure 6.9 b, about 200 µm away from the injection plug, compared to 3 mm in Figure 6.9 a. Figure 6.10 shows the IEF results for BSA and a mixture of BSA and insulin. Almost no initial peak was observed, and the two proteins were baseline resolved.

132

Figure 6.8 Electropherograms of IEF processes on capillary. Anolyte: 10 mM H_3PO_4; Catholyte: 20 mM NaOH containing 0.06% HPMC; Sample: Figure 6.8 a, Insulin (50 ng/mL) in a mixture of 4M urea, 0.1% HPMC and 3% ampholyte, Figure 6.8 b insulin (19 ng/mL) and BSA (0.13 μM) in a mixture of 4M urea, 0.1% HPMC and 3% ampholyte; Injection: 8 kV for 3 s; Focusing: 500 V/cm.
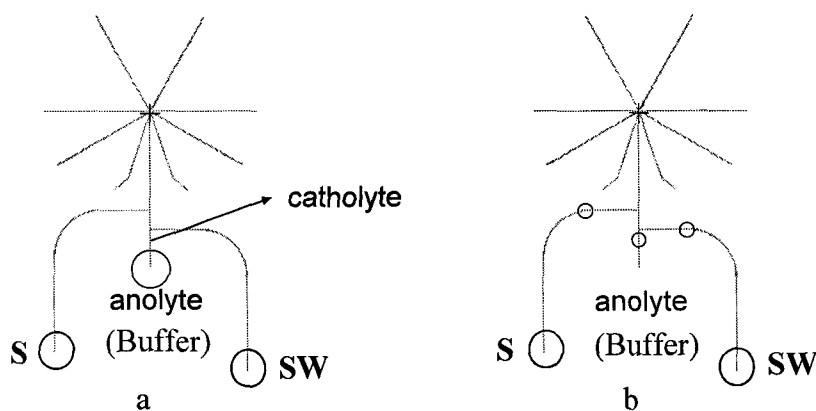
Figure 6.9 Chip design layouts. (a) The normal way of drilling access holes and filling the device trapped catholyte between sample plug and anolyte; (b) The access holes for buffer introduction and injection were moved to make the buffer reservoir as close as possible to the sample plug and shorten the injection loop in order to replace the catholyte entirely with sample in short time.

133
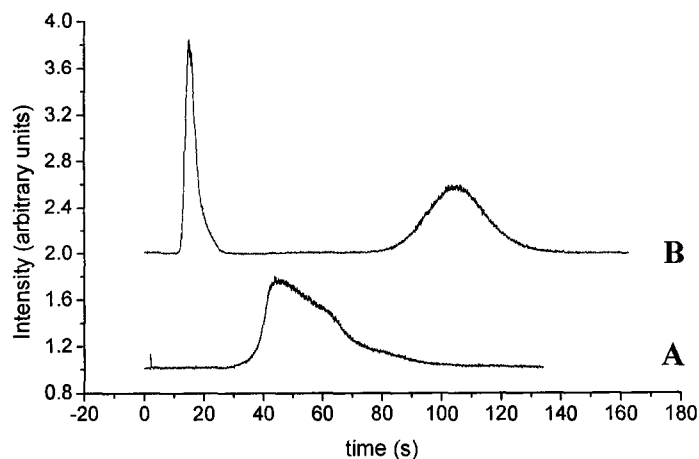
Figure 6.10 Electropherograms of IEF processes following device modifications discussed in Figure 6.9 b. Anolyte: 100 mM H_3PO_4; Catholyte: 20 mM NaOH containing 0.06% HPMC and 0.06% HPMC; Sample: **trace A** BSA (0.09μM) in the mixture of 4M urea, 0.1% HPMC and 3% ampholyte, **trace B** mixture of insulin (1 ng/mL) and BSA(0.045 μM) in the mixture of 4M urea, 0.1% HPMC and 3% ampholyte; Injection: -0.5 kV for 4 s; Buffer reservoirwas at ground; Collection reservoir was at -0.8 kV for trace **A** and -1.0 for trace **B**, respectively; Sheath reservoirs were floating.
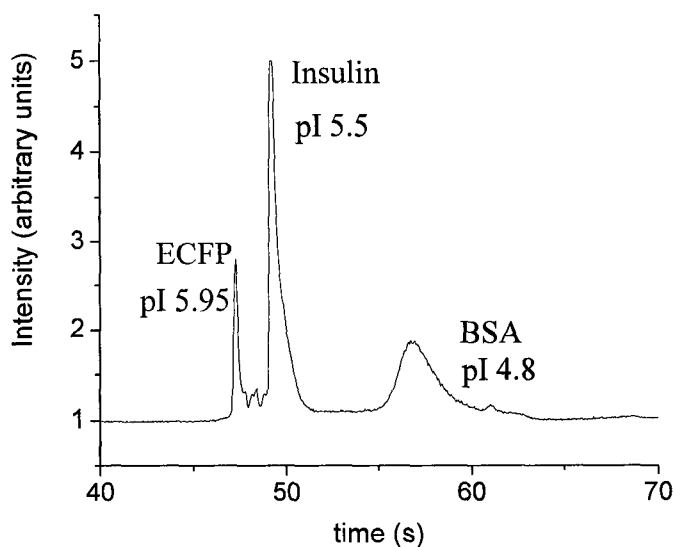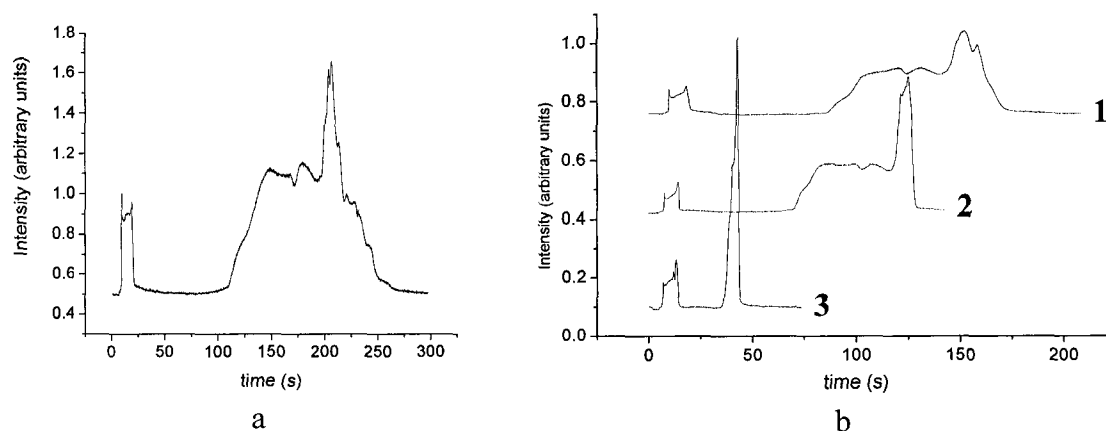

Figure 6.11 Electropherogram of IEF process following device modifications discussed in Figure 6.9 b. The conditions were the same to those of Figure 6.10 except the collection reservoir was held at -0.9 kV. Sample: insulin (670 ng/mL), BSA(0.03 μM) and ECFP (0.033 μM) in the mixture of 4M urea, 0.1% HPMC and 3% ampholyte.

134

Figure 6.11 demonstrates the separation of ECFP, insulin and BSA according to their pI values. As shown in Figure 6.10, the migration time is not directly related to the focusing voltage, because in Figure 6.10 B higher applied focusing voltage (1.0 kV) than that in Figure 6.10 A (0.8 kV) resulted in longer migration time for BSA. It is likely that unstable EOF originating from the pH gradient and irreproducible channel surface activity, caused variation in the migration time. For two runs in sequence, there was no predictable trend of the variation in the migration time. However, EOF became smaller after the device was used for more than four hours. Although after each run of focusing, the chip was flushed with catholyte under the driven of EOF for 10 min, the channel surface may not be fully regenerated.

6.3.3 IEF on the multiplexed chip

IEF experiments were next performed on the 36-channel multiplexed chip, the detailed dimensions of which are given in Figure 4.1 and Table 4.1. However, the protein samples and good separating conditions in Figure 6.11 were not working in the multiplexed device. We then tested other protein samples and separating conditions. Alexa Fluor 488 labeled trypsin inhibitor and fluorescent protein mRFP were used as model proteins. Figure 6.12 a and trace 1 in Figure 6.12 b show that no sharply focused peaks of mRFP or trypsin inhibitor could be obtained at low focusing voltage (0.35 kV was applied). However, trace 1 and 2 in Figure 6.12 b show that higher focusing voltage (0.5 kV) gave shorter migration time and narrower peaks. Traces 2 and 3 demonstrate that trypsin inhibitor was focused more tightly and mobilized in a shorter time, as the concentration of phosphoric acid increased. The wider and slightly higher peaks in

135

Figure 6.13, compared to trace **3** in Figure 6.12 b, show that more protein molecules were focused when the two sheath reservoirs received a positive voltage. This can be attributed to the longer focusing time induced by lower electric field when using the voltage combination in Figure 6.13. No improvement in the resolution was found at higher voltage combinations. Moreover, bubbles formed when the sheath voltage was above 0.8 kV. The results of sheath flow effects discussed in previous chapters showed the formation of bubbles when the sheath voltage was higher than 1.5 kV. However, bubbles appear even at lower voltages in the IEF process, presumably because of heat accumulation due to longer run times.

a

b

Figure 6.12 Electropherograms of IEF processes. Anolyte, catholyte and sample buffer are the same to those in Figure 6.10 except anolyte of *trace 3* in Figure 6.12 b was 200 mM H_3PO_4; Sample: mRFP (2×10^{-13} M) for Figure 6.12 a, trypsin inhibitor (10 ng/mL) for Figure 6.12 b; Injection: 1.0 kV for 100 s; Buffer reservoir: 0.35 kV for Figure 6.12 and *trace 1* in Figure 6.12 b, 0.5 kV for *trace 2* and 3 in Figure 6.12 b; Collection reservoir were at ground for all traces; Sheath reservoirs were floating .

136
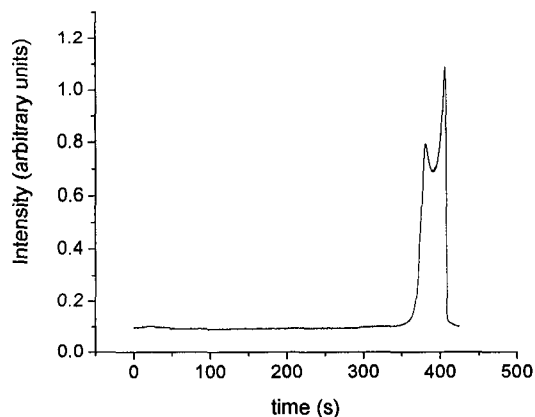
Figure 6.13 Electropherogram of IEF process. The conditions are the same to those of *trace 3* in Figure 6.12 b except the sheath reservoirs received 0.47 kV.

Since the IEF resolution on our device always suffers from EOF, it was informative to investigate the IEF profile along the separation channel. A detector was placed at four different positions in sequence as shown in Figure 6.14 a. Figure 6.14 b shows the IEF electropherograms of a protein mixture collected at each position. No observable focused peaks were collected at position 1 and 2, illustrating that the sample zone simply swept past the detector before being focused. Focused peaks appeared in the electropherograms collected at positions 3 and 4. The peaks at position 4 are wider and have begun to resolve. The profile study verified the influence of EOF on IEF separation and indicates that a longer separation channel might be beneficial for IEF separation.

137

a

b
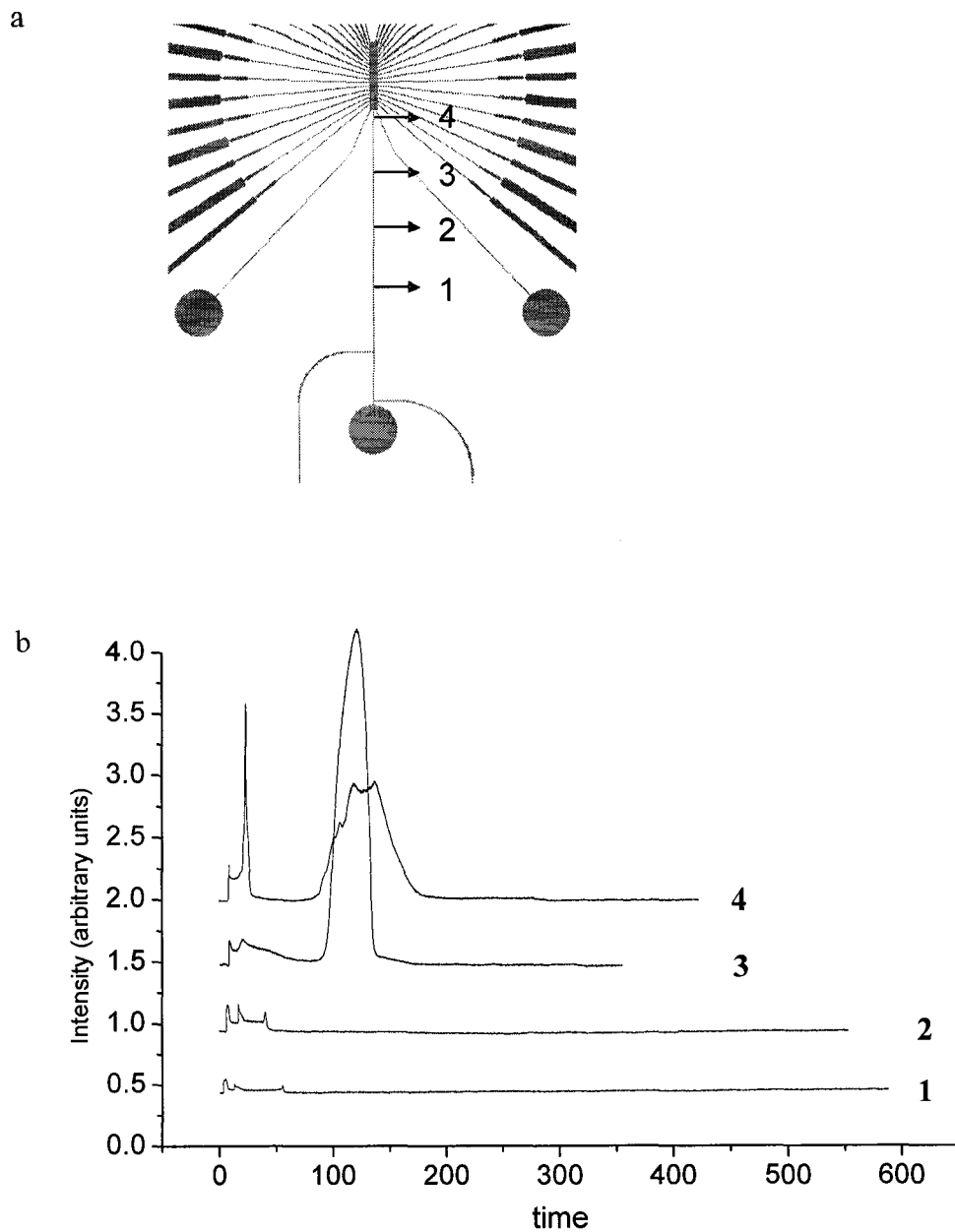
Figure 6.14 The electropherograms monitored at each detection point shown in the chip layout. Anolyte: 100 mM H_3PO_4; Catholyte: 20 mM NaOH containing 0.06% HPMC and 0.06% HPMC; Sample: mixture of trypsin inhibitor (33 ng/mL), carbonic anhydrase (0.066 μM) and mTrfp (O/9×10⁸) in the mixture of 4M urea, 0.1% HPMC and 3% ampholyte; Injection: 0.9 kV for 20 s; Anodic reservoir: 0.35 kV; Collection reservoir: grounded.

138

6.4 Conclusion

This chapter demonstrated one-step IEF for different fractionator designs. The focusing was found to relate to sample buffer and running buffer composition, the distance between anodic reservoir and injection plug and the length of the sample channel. For two-step IEF, the resolution is not affected by the channel length as shown by the following equation,

$$\Delta pI = 3\sqrt{\frac{D}{E - d(pH)}\frac{d\mu}{d(pH)}\frac{d(pH)}{dx}}$$

where ΔpI is the resolving power, D is diffusion coefficient of the analyte, E is the electric field and $d\mu/dpH$ is the electrophoretic mobility change with pH. However, our experiments show that, for one-step IEF, especially in the case where EOF is not reduced at all, the resolution changes with sample channel length and focusing voltage. A delicate balance needs to be satisfied in order to obtain baseline-resolved peaks. High focusing voltage can increase resolution, yet lead to formation of bubbles and strong EOF, which is detrimental to the stability of pH gradient. In order to reach higher focusing voltage, the voltages applied to the sample and sheath reservoirs should be increased accordingly. The large current flow from the sheath channels and the heat accumulated from the IEF process together make bubbles form at voltages above. Good resolution might be obtained in a longer separation channel (over 1 cm) at lower voltage combinations. However, the lower velocity associated with lower voltages makes diffusion in the fractionation zone worse. While not explicitly evaluated here, the variation in EOF along the channel also results in reduced resolution due to pressure effects induced by differential pump rates along the channel walls. Therefore, IEF may

139

not be an optimal separation method to couple with this electrokinetically controlled fractionator. Separation of protein according to molecular weight in SDS gel might be a potential method for our fractionator. However, removal of SDS before subsequent denaturing and electro-spray would be necessary.

6.5 Reference

1. Chen, J.Z.; Balgley, B.M.; DeVoe, D.L.; Lee, C.S. *Anal. Chem.* **2003**, 75, 3145-3152.

2. Hofmann, O.; Che, D.P.; Cruickshank, K.A.; Müller, U.R. *Anal. Chem.* **1999**, 71, 678-686.

3. Mao, Q.L.; Pawliszyn, J. *Analyst*, **1999**, 124, 637-641.

4. Cui, H.C.; Horiuchi, K.; Dutta, P.; Ivory, C.F. *Anal. Chem.* **2005**, 77, 1303-1309.

5. Tang, Q.; Harrata, A.K.; Lee, C.S. *Anal. Chem.* **1996**, 68, 2482-2487.

6. Kilar, F.; Hjerten, S. *Electrophoresis*, **1989**, 10, 23-29.

7. Chen, S. M.; Wiktorowicz, J.E. *Anal. Biochem.* **1992**, 206, 84-90.

8. Hiraoka, A.; Tominaga, I.; Hori, K. *J. Chromatogr. A*, **2002**, 961, 147-153.

9. Moorhouse, K.G.; Eusebio, C.A.; Hunt, G.; Chen, A.B. *J. Chromatogr. A*, **1995**, 717, 61-69.

10. Mazzeo, J.R.; Krull, I.S. *Anal. Chem.* **1991**, 63, 2852-2857

11. Gao, L.; Liu S.R. *Anal. Chem.* **2004**, 76, 7179-7186.

Chapter 7 Future work and some thoughts

7.1 Summary of the thesis work

In this thesis work, several generations of fractionators were designed based on electrokinetically driven flow. Two modes of fraction collection, peak selection and fixed time intervals, were explored. Monolithic polymer beds were assembled onto a multiplexed fractionator. The polymerization reaction conditions and chip dimensions were optimized so that the polymer beds have no influence on the sheath flow effect in the fractionation zone.

7.2 Separation in sample channel

Chapter 6 discussed the influence of the separation channel length on IEF separation. The study of the IEF profile demonstrated better separation at positions further away from the injection plug. Therefore, a longer separation channel might be beneficial for one-step IEF separation. In future, separation channels of different lengths need to be tested, while the dimensions of other channels should be adjusted accordingly in order to perform an efficient pinching effect. To simplify the design, only the separation channel and the furthest collection channel could be kept on the device. Once a suitable separation channel length is found, the separation channel will be integrated with all fractionation channels.

Other separation methods can be considered as well. Capillary gel electrophoresis on microchip [1] has been reported to give good separation of proteins. This method might be coupled with the fractionator. By applying vacuum to the first fractionation reservoir, the sieving matrix can be introduced from the separation reservoir, past the

141

injection plug until it arrives just at the sheath point. In order to avoid leakage of the sieving matrix into the injection arms, the two reservoirs at the end of injection arms must be sealed. Because protein molecules are usually negatively charged in normal buffers and electrophoretic force is the main driving force in CGE, the sheath point must be held at a higher potential than the separation reservoir. CGE has an advantage over IEF on this fractionator because the channel surface will not be changed significantly and thus the reproducibility should be improved. However, CGE can not produce a concentrated peak, in contrast to IEF. Since protein separation through one dimension is usually not efficient, a 2-D separation coupled with the fractionator needs to be explored in the future.

7.3 Improvement of polymer beds or channel dimensions

In Chapter 5, the introduction of polymer beds did not affect the sheath flow effect finally, after continuous efforts to optimize the polymerization reaction conditions. However, the reaction time needed to be optimized in order to form a polymer structure with a low flow resistance. We find that even slight changes in the reaction mixtures lead to great change in the optimal reaction time. To avoid this issue, it is worth the effort to keep looking for a recipe for polymerization which can create larger pores and thus smaller flow resistance on our fractionator. If large pores can not be realized on this device, modification of the unpacked portions of the collection channels in order to decrease EOF might be worth further investigation. When EOF from the modified collection channel matches that of the packed portion, there will be less accumulation of pressure before and after the polymer bed. However, EOF in the fractionation zone

142

should not be decreased. Otherwise, the widening of the sample stream due to diffusion will become a significant issue. This kind of selective modification on a complex design is not easy to realize.

7.4 Protein digestion on polymer bed

The fractionator integrated with polymer beds is basically ready for the next trypsin digestion step. Trypsin solution needs to flow through the polymer beds. As discussed in Chapter 4, when solution is driven into the entire device by a pressure pump, significant flow occurred only in the first couple of fractionation channels and longer and longer time was taken to reach the other channels. Therefore, the trypsin solution can be introduced by electrokinetic force instead of pressure-driven force. After digestion, the peptide digestion mixture might be adsorbed onto the polymer beds as well. However, we have not investigated the adsorption capacities of the polymer beds for peptides. Theoretically, all peptides should be adsorbed for protein identification. Therefore, the recipes for polymerization reactions should be studied thoroughly in order to figure out which polymer beds can fully adsorb peptides.

7.5 Protein identification

The step after digestion and adsorption of peptides is elution of the adsorbed peptides from the polymer beds to be detected by the MS. Electrokinetically driven flow is the only way to elute the peptides on our device. However, because the organic additives in the eluent will change the surface charges, the flow rate of EOF might not be stable for elution of different beds. The other big unresolved issue is the interface

143

with the MS for this fractionator. Without an interface to the MS, much more work will be involved to collect the digestion mixture and introduce it into the MS. One way of integrating an ESI tip is to use a single tip. More channels will be added downstream of this fractionator and finally they will join at one point where a capillary ESI tip can be connected. Another way is to use a separate tip for each channel. The entire device will be placed on a rotating disk and thus the tips will spray one by one into the MS. If multiple tips have to be used, a capillary tip is not recommended because of the complexity of connecting multiple tips. A polymeric tip [2] might be a good solution, because many tips can be made in the same batch.

Reference

1. Shadpour, H.; Soper, S.A. *Anal. Chem.* **2006**, 78, 3519-3527.
2. Koerner, T.; Turck, K.; Brown, L.; Oleschuk, R.D. *Anal. Chem.* **2004**, 76, 6456-6460.